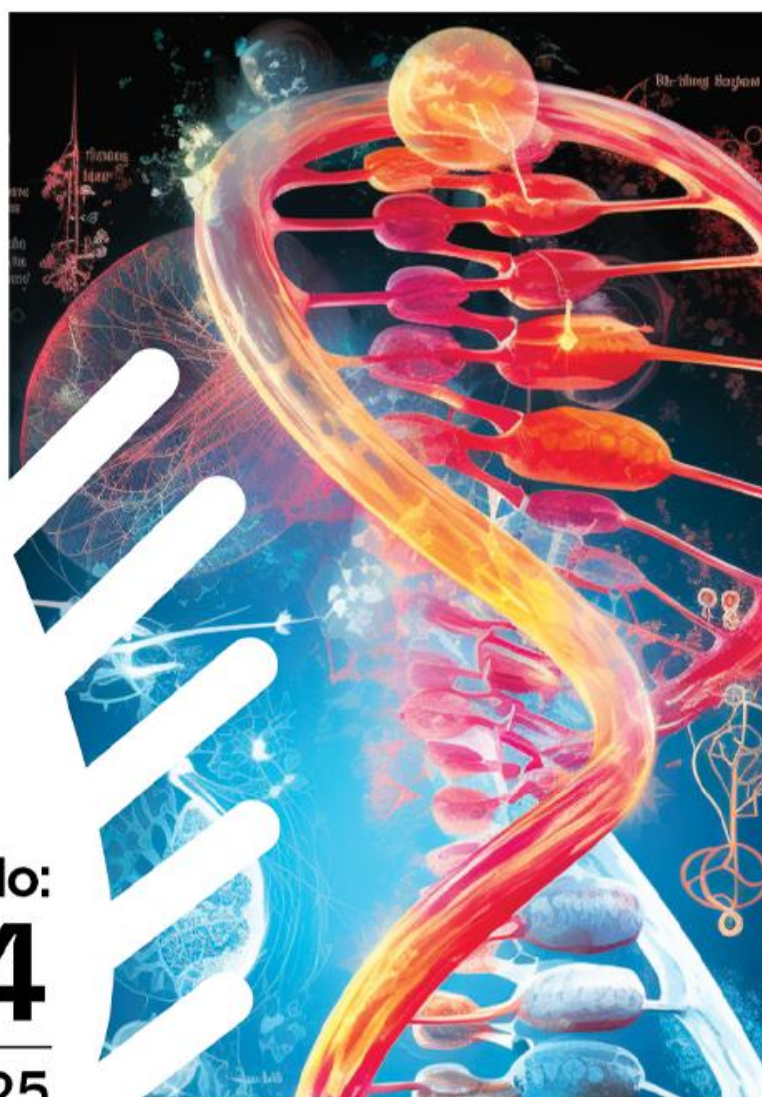


The European
Chemistry and
Biotechnology
Journal



No:
04
2025

The European Chemistry and Biotechnology Journal

Issue 4 • July 2025

Editor-in-chief

Tunc Catal, Uskudar University, Türkiye
E-mail: tunc.catal@uskudar.edu.tr (<https://orcid.org/0000-0003-2990-8680>)

Editorial board

Abhilasha Singh Mathuriya, Ministry of Environment, Forest and Climate Change, India
E-mail: imabhilasha@gmail.com
(<https://orcid.org/0000-0002-6601-8241>)

Ahad Mokhtarzadeh, Tabriz University of Medical Sciences, Iran
E-mail: ahad.mokhtarzadeh@gmail.com
(<https://orcid.org/0000-0002-4515-8675>)

Baris Binay, Gebze Technical University, Türkiye
E-mail: binay@gtu.edu.tr
(<https://orcid.org/0000-0002-6190-6549>)

Bharat Patel, Queensland University of Technology, Australia
E-mail: bharat.patel@qut.edu.au
(<https://orcid.org/0000-0002-5332-1858>)

Burcu Gunduz Ergun
Yildiz Technical University
E-mail: burcugunduz3@gmail.com
(<https://orcid.org/0000-0002-9344-1336>)

Chontisa Sukkasem, Thaksin University, Thailand
E-mail: chontisa.s@gmail.com
(<https://orcid.org/0000-0001-8043-4981>)

Deniz Yildirim, Cukurova University, Türkiye
E-mail: dyildirim@cu.edu.tr
(<https://orcid.org/0000-0002-5041-8160>)

Irina Nakashidze, Batumi Shota Rustaveli State University, Georgia
E-mail: irinanakashidze@yahoo.com
(<https://orcid.org/0000-0001-8934-6312>)

Jean-Marie Fontmorin, Chemical Engineering Research Center of Toulouse, France
E-mail: jeanmarie.fontmorin@toulouse-inp.fr
(<https://orcid.org/0000-0002-0832-7185>)

Lakhveer Singh, Sardar Patel University, Mandi, H.P., India
E-mail: lakhveer@spumandi.ac.in
(<https://orcid.org/0000-0002-4926-9778>)

Luguang Wang, Utah State University, USA
E-mail: luguang.wang@usu.edu
(<https://orcid.org/0000-0002-4566-6143>)

Milena Brouwer-Milovanovic
Swedish Environmental Research Institute IVL, Sweden
E-mail: milena.milovanovic@ivl.se
(<https://orcid.org/0009-0001-2019-3706>)

Muhsin Konuk, Uskudar University, Türkiye
E-mail: muhsin.konuk@uskudar.edu.tr
(<https://orcid.org/0000-0002-6651-718X>)

Oliver Feeney, The Eberhard Karls University of Tübingen, Germany
E-mail: oliver.feeney@uni-tuebingen.de
(<https://orcid.org/0000-0003-3585-448X>)

Rabah Boukherroub, CNRS & University Lille, France
E-mail: rabah.boukherroub@univ-lille.fr
(<https://orcid.org/0000-0002-9795-9888>)

Rahinah Ibrahim, Universiti Putra Malaysia, Malaysia
E-mail: rahinah.ibrahim@gmail.com
(<https://orcid.org/0000-0001-6741-6439>)

Raikhan Beisenova, LN Gumilyov Eurasian National University, Kazakhstan
E-mail: raihan_b_r@mail.ru
(<https://orcid.org/0000-0003-0913-9503>)

Ramazan Solmaz, Bingol University, Türkiye
E-mail: rsolmaz@bingol.edu.tr
(<https://orcid.org/0000-0002-9295-1203>)

Sirin Korulu Koc, Tallinn University, Estonia
E-mail: sirinkorulu@gmail.com
(<https://orcid.org/0000-0001-6762-0659>)

Suhendan Ekmekcioglu, MD Anderson Cancer Center, USA
E-mail: sekmekcioglu@mdanderson.org
(<https://orcid.org/0000-0003-4079-6632>)

Tommaso Beccari, Università degli Studi di Perugia, Italy
E-mail: tommaso.beccari@unipg.it
(<https://orcid.org/0000-0001-9637-6579>)

Xu-Dong Zhou
Hunan University of Chinese Medicine, Hunan province, China
E-mail: xudongzhou999@163.com
(<https://orcid.org/0000-0001-7445-5428>)

Yolina Hubenova, Institute of Electrochemistry and Energy Systems, Bulgaria
E-mail: jolinahubenova@yahoo.com
(<https://orcid.org/0000-0003-1783-758X>)

Language editor

Cigdem Sezer Zhmurov, Uskudar University, Türkiye
E-mail: cigdem.sezerzhmurov@uskudar.edu.tr
(<https://orcid.org/0000-0002-8423-5063>)

Publicity managers

Dilan Akagunduz, Istanbul Technical University, Türkiye
E-mail: dilanakagunduz@gmail.com
(<https://orcid.org/0000-0002-8057-6688>)

Rumeysa Cebecioglu, Koc University, Türkiye
E-mail: rmyscbcglu@gmail.com
(<https://orcid.org/0000-0002-5996-5363>)

Sila Arslan, Istanbul University, Türkiye
E-mail: arslansilaa@gmail.com
(<http://orcid.org/0000-0001-8757-264X>)

Burak Kilinc, Uskudar University, Türkiye
E-mail: burakaliosman.kilinc@uskudar.edu.tr
(<https://orcid.org/0009-0005-0533-8064>)

Editorial assistant

Aksana Kavaleuskaya, Uskudar University, Türkiye
E-mail: aksana.kavaleuskaya@gmail.com
(<http://orcid.org/0009-0002-2310-5545>)

Publisher: Tunc Catal
Publishing manager: Prof. Dr. Tunc Catal
Editorial office: Uskudar University, Universite Sok. No:14 34662 Altunizade Uskudar, Istanbul-Türkiye
Email: editor@euchembioj.com; **Phone:** +90 216 400 2222 (ext. 2417)
WEB: <https://euchembioj.com/index.php/pub> **DOI:** <https://doi.org/10.62063/ecb-no4.2025>
ISSN: 3023-5839

The European Chemistry and Biotechnology Journal

Issue 4 • July 2025

CONTENTS

RESEARCH ARTICLES	Page no.
Seashell-based bioceramics for advanced electrospun tissue scaffolds Sema Nur Sahin, Erdi Bulus, Alper Tezcan, Muhammad Umar Farooq, Marwah Al-garash, Yesim Muge Sahin	1-13
Identification of new candidate molecules against SARS-CoV-2 through docking studies Punar Aliyeva, Beyza Yilmaz, Doruk Alp Uzunarslan, Vildan Enisoglu Atalay	14-23
Correlation of ferritin, D-dimer, and CRP with disease severity and outcome in COVID-19 patients Ia Murvanidze, Ilia Nakashidze, Teona Gogitidze, Ermira Java, Aleena Parveen Shaikh, Nino Tebidze, Nameera Parveen Shaikh, Besik Kakabadze, Maia Resulidze, Rajnesh Khurana, Eteri Saralidze, Otari Tsetskhladze, Davit Baratashvili, Nino Kedelidze, Tamar Peshkova, Irina Nakashidze	24-39
Nanosomes carrying mycosynthesized silver nanoparticles as a drug delivery tool against MDR <i>Salmonella typhi</i> BT CB170 Mehwish Iqtedar, Nimra Ilyas, Mehral Aslam, Roheena Abdullah, Afshan Kaleem	40-52
Immature morphology of adult-born granule cells alters responsiveness and excitability in a multi-compartmental conductance-based model Bahar Sert, Pinar Oz	53-68
Gango + BioFunctional: A computational tool for efficient functional gene analysis Alejandro Rodriguez-Mena, Xavier Tarragó-Claramunt, Giulia Castellani, Javier Méndez-Viera, Antonio Monleón-Getino	69-80

RESEARCH ARTICLE

Seashell-based bioceramics for advanced electrospun tissue scaffolds

Sema Nur Sahin^{1,2}  | Erdi Bulus^{1,3}  | Alper Tezcan^{1,4}  | Muhammad Umar Farooq⁵ 
Marwah Al-garash²  | Yesim Muge Sahin^{1,2*} 

¹ Istanbul Arel University, ArelPOTKAM (Polymer Technologies and Composite Application and Research Center), **Istanbul, Türkiye**
ROR ID: [03natay60](https://orcid.org/03natay60)

² Istanbul Arel University, Biomedical Engineering Department, **Istanbul, Türkiye**
ROR ID: [03natay60](https://orcid.org/03natay60)

³ Istanbul Arel University, Transportation Services Civil Aviation Cabin Services Program, Vocational School, **Istanbul, Türkiye**
ROR ID: [03natay60](https://orcid.org/03natay60)

⁴ Istanbul Arel University, Mechanical Engineering Department, **Istanbul, Türkiye**
ROR ID: [03natay60](https://orcid.org/03natay60)

⁵ East China University of Science and Technology, State Key Laboratory of Chemical Engineering, **Shanghai, China**
ROR ID: [01vyrm377](https://orcid.org/01vyrm377)

* **Corresponding author:** E-mail: ymugesahin@arel.edu.tr; Ph.: +90 5379757507

Citation: Sahin, S.N., Bulus, E., Tezcan, A., Farooq, M.U., Al-garash, M., & Sahin, Y.M. (2025). Seashell-based bioceramics for advanced electrospun tissue scaffolds. *The European chemistry and biotechnology journal*, 4, 01-13.
<https://doi.org/10.62063/ecb-49>

License: This article is licensed under a Creative Commons Attribution-NonCommercial 4.0 International License (CC BY-NC 4.0).

Peer review: Double Blind Refereeing.

Ethics statement: It is declared that scientific and ethical principles were followed during the preparation of this study and all studies utilized were indicated in the bibliography (Ethical reporting: editor@euchembioj.com).

Plagiarism Check: Done (iThenticate).
Article has been screened for originality.

Received: 05.01.2025
Accepted: 01.03.2025
Online first: 15.03.2025
Published: 11.07.2025

Abstract

The demand for tissue scaffolds to support the repair, regeneration, and restoration of damaged tissues is rapidly growing. Scaffolds fabricated using the electrospinning technique are particularly significant in tissue engineering due to their ability to provide micro- to nano-scale porosity and a large surface area. This study focuses on developing tissue scaffolds with enhanced cell adhesion, biodegradability, and tensile strength by employing aqueous solutions of polyvinyl alcohol (PVA), a biocompatible and biodegradable synthetic polymer; gelatin (GEL), a natural polymer that offers binding sites conducive to cell adhesion and differentiation; and synthesized bioceramics, all integrated through the electrospinning process. Composite tissue scaffolds were engineered by incorporating 1% to 3% GEL into the PVA solution, followed by the addition of 1% bioceramics to the 1% GEL-enriched PVA. The composite formulation not only emulates the extracellular matrix as a biomimetic strategy but also goes beyond merely enhancing ossification. Comprehensive structural, morphological, mechanical, and thermal characterizations were conducted to analyze the properties of the scaffolds containing the synthesized bioceramics. The tensile strengths of the fabricated nanocomposites were determined to be 6.25 MPa for 10:0 (PVA:GEL), 7.45 MPa for 10:1 (PVA:GEL), 8.01 MPa for 10:3 (PVA:GEL), and 8.22 MPa for 10:1:1 (PVA:GEL:Bioceramics), respectively, indicating a progressive enhancement in mechanical properties with the incorporation of GEL and bioceramics. The results demonstrate the successful production of a potential biomaterial with ideal properties for



tissue engineering applications. These composite scaffolds, providing a conducive environment for cell adhesion and exhibiting excellent mechanical properties, are anticipated to be suitable for dental applications as an intermediate layer which may support bone and connective tissue formation

Keywords: Bioceramic, tissue scaffold, electrospinning, gelatin, polyvinyl alcohol.

Introduction

Tissue engineering is based on three key factors: cells, growth factors, and tissue scaffolds, and it is a discipline aimed at functionally restoring damaged tissues. Tissue scaffolds are regenerative structures that support tissue repair and are significant as they are used in the healing of damaged tissues and organs. They support cells when seeded *in vitro* and promote matrix formation, laying the foundation for tissue transplantation (Howard et al., 2008).

The materials used in the production of tissue scaffolds play a crucial role in promoting cell proliferation and differentiation. An ideal tissue scaffold should possess good biocompatibility, appropriate pore size and porosity, and excellent mechanical strength, while also exhibiting characteristics suitable for the specific area of the body where it will be applied (Keçeciler et al., 2023). Tissue scaffolds fabricated via the electrospinning technique have garnered significant attention in tissue engineering due to their excellent biocompatibility, optimal biodegradability, non-toxic nature, micro-to nano-scale porosity, and their ability to achieve a high surface-to-volume ratio (Sadeghi et al., 2018; Cam et al., 2019). Tissue engineering has garnered significant attention in recent years (Aydogdu et al., 2019). Polymer/ceramic composite biomaterials and tissue scaffolds produced using the electrospinning technique exhibit enhanced mechanical strength and optimal cell adhesion. The superior performance of composite materials has led to a surge in research focusing on polymer and ceramic materials (Hoque et al., 2014).

Polymer materials provide a suitable framework for replicating the natural architecture of soft tissues. Integrating bioceramics into polymers enhances their potential for repair and regeneration strategies (Zou et al., 2018; Filippi et al., 2020; Jazayeri et al., 2020). PVA, a synthetic polymer, is both biocompatible and biodegradable; however, its limited cell recognition sites reduce its bioactivity. In contrast, GEL offers numerous integrin binding sites, facilitating cell adhesion and differentiation (Heydary et al., 2015; Perez-Puyana et al., 2018). Bioceramics are widely favored for incorporation into tissue scaffolds due to their ability to support cell growth and proliferation, exhibit antimicrobial properties, contribute to the repair of bone and dental tissues, and serve as effective materials for soft tissue healing applications (Xie et al., 2019; Zhang et al., 2021). Chemical precipitation, the most commonly used technique for bioceramic synthesis, enables the production of bioceramics with high efficiency and low cost in the absence of organic solvents. Moreover, the only by-product of the reaction is water, which does not contain any other elements, making this method quite suitable for biomedical applications (Mazumder et al., 2019; Santhosh et al., 2013; Gunduz et al., 2013; Şahin et al., 2018).

In the present study, it is aimed to produce a composite tissue scaffold that mimics the extracellular matrix (ECM). For this scaffold, which was fabricated using both ECM composite components and nanoscale production, the following steps were carried out: synthesizing bioceramics from sea snail shells via chemical precipitation, incorporating the synthesized bioceramics into a PVA/gelatin (GEL) solution, and producing tissue scaffolds with suitable cell adhesion and biocompatibility via electrospinning technique. Additionally, the structural, morphological, mechanical, and thermal

characterizations of the synthesized bioceramics and the fabricated tissue scaffolds were performed to evaluate their properties for tissue engineering applications.

Materials and methods

Materials

For the synthesis of bioceramics, marine snail shells were obtained from a seafood company in Eminönü, Istanbul. For tissue scaffold production, a polyvinyl alcohol (PVA) polymer with a molecular weight of 85.000-124.000 g/mol was purchased from Sigma-Aldrich (Turkey). Food-grade gelatin (GEL) was acquired from a local herbalist in Eminönü, Istanbul. Ultrapure water with a resistance of 18.3 MΩ was used as the solvent for preparing the polymer solution.

Bioceramics synthesis

Marine snail shells were selected as the source for bioceramic synthesis. Initially, the shells were sterilized in an ultrasonic bath at 90°C for 30 minutes, followed by drying in an oven at 100°C for 3 hours to ensure purification. The dried shells were then ground into powder using a ceramic mortar and further sieved through a stainless steel mesh with a size of 100 μm to achieve a uniform particle size.

Thermal analysis was conducted to quantify the calcium carbonate (CaCO₃) content in the powders. Using this data, the required amount of phosphoric acid (H₃PO₄) was calculated based on the stoichiometric (molar) calcium-to-phosphorus (Ca/P) ratios: 1.67 for hydroxyapatite and 1.50 for tricalcium phosphate. For each batch, 2 g of powdered shell was measured and transferred into a beaker containing 50 ml of pure water. The mixture was heated to 90°C on a magnetic stirrer, and the calculated H₃PO₄ solution was added dropwise. Once bubbling ceased, the mixture was continuously stirred at 90°C for 8 hours and then allowed to cool to room temperature to complete the reaction. The resulting precipitate was separated by centrifugation, and the wet powder was dried in an oven at 100°C for 24 hours. The dried precipitate was sintered at 850°C for 4 hours to obtain the final bioceramic product (Sahin et al., 2018; Yelten and Yılmaz, 2010).

Preparation of solutions

To produce composite tissue scaffolds, PVA, GEL, and bioceramic powders were dissolved in distilled water using a magnetic stirrer. A pure 10:0 (PVA: GEL) solution was prepared by dissolving 10 g of PVA in 100 ml w/v of distilled water and stirring at 80°C for 150 minutes. Subsequently, GEL was added to the 10:0 (PVA: GEL) solution in weight ratios of 1% and 3% w/v. These mixtures were stirred at 40°C for 150 and 180 minutes, respectively, to obtain 10:1 (PVA: GEL) and 10:3 (PVA: GEL) solutions (Linh et al., 2010). Finally, 1% bioceramic powder was added to the 10:1 (PVA: GEL) solution and stirred at 37°C for 210 minutes, resulting in the 10:1:1 (PVA:GEL:Bioceramics) solution (Song et al., 2010; Ba Linh et al., 2013). The preparation parameters for the solutions required for composite tissue scaffold fabrication are shown in Table 1.

Table 1. Preparation parameters of solutions used for the fabrication of composite tissue scaffolds.

Polymer weight ratio	Temperature (°C)	Time (min)
10:0 (PVA: GEL)	80	150
10:1 (PVA: GEL)	40	150
10:3 (PVA: GEL)	40	180
10:1:1(PVA:GEL:Bioceramics)	37	210

1.1. Production of composite tissue scaffolds

Composite tissue scaffolds were fabricated using the electrospinning technique by applying the working parameters listed in Table 2 (Sengor et al., 2018). To remove any residual solvents, the produced tissue scaffolds were dried in an oven at 45°C for 24 hours.

Table 2. Electrospinning production parameters for composite tissue scaffolds.

Polymer Content	Flow Rate (ml/hr)	Distance (cm)	Voltage (kV)
10:0 (PVA: GEL)	5.0	15	30
10:1 (PVA: GEL)	5.0	15	30
10:3 (PVA: GEL)	5.0	10	25
10:1:1(PVA: GEL:Bioceramics)	3.0	5	25

1.2. Characterization studies

Fourier transform infrared (FTIR) analysis: The presence of functional groups in the bioceramics and composite tissue scaffolds was determined by FTIR spectroscopy (FT/IR-6600, JASCO, Tokyo, Japan) in the wavelength range of 400-4400 cm^{-1} . These analyzes enabled the structural characterization of the bioceramics and composites, confirming their composition and the successful incorporation of bioceramics into the composite tissue scaffolds.

Field emission gun scanning electron microscopy (FEGSEM) analysis: Bioceramics and composite tissue scaffolds were coated with gold-palladium under Argon (Ar) gas and analyzed using a field emission gun scanning electron microscope (FEGSEM 450, FEI Quanta, Oregon, USA). Images were captured under high vacuum at a range of 12.00-15.00 kV potential, with scales from 100-500 nm to 500 nm-2 μm . The diameters of 40 nanofibers were measured from the images, their arithmetic mean was calculated, and the nanofiber diameter distributions were determined. For all the samples, morphological analysis was conducted at various magnifications.

Tensile test: The tensile test for composite tissue scaffolds was performed according to ASTM D882-10 standards using a tensile testing machine (DVT UZM K3, DVT DEVOTRANS, Istanbul, Türkiye). The test was conducted under a 500 N load, with a tensile speed of 5 mm/min.

Thermogravimetric analysis (TGA): The CaCO_3 content of marine snail shells was determined using a TGA device (STA7200, Hitachi, Tokyo, Japan). Thermal characterization of the samples was conducted under Nitrogen (N_2) atmosphere at a heating rate of 15°C /minute, within the temperature range of 30-900°C.

Results and discussion

Thermal characterization of bioceramics with TGA

Upon analysis of the TGA thermogram of sea snail shells (Figure 1), it was observed that 45.0% of the material was lost during heating, attributed to the decomposition of organic matter and impurities, while the remaining 55.0% was identified as inorganic CaO.

Using the 55.0% CaO content, the stoichiometric molar ratio corresponding to the mineral

composition of bone in the human body was calculated to determine the required amount of H_3PO_4 . This calculated H_3PO_4 quantity was subsequently incorporated into the CaO structure during the chemical precipitation process, enabling the successful synthesis of bioceramics.

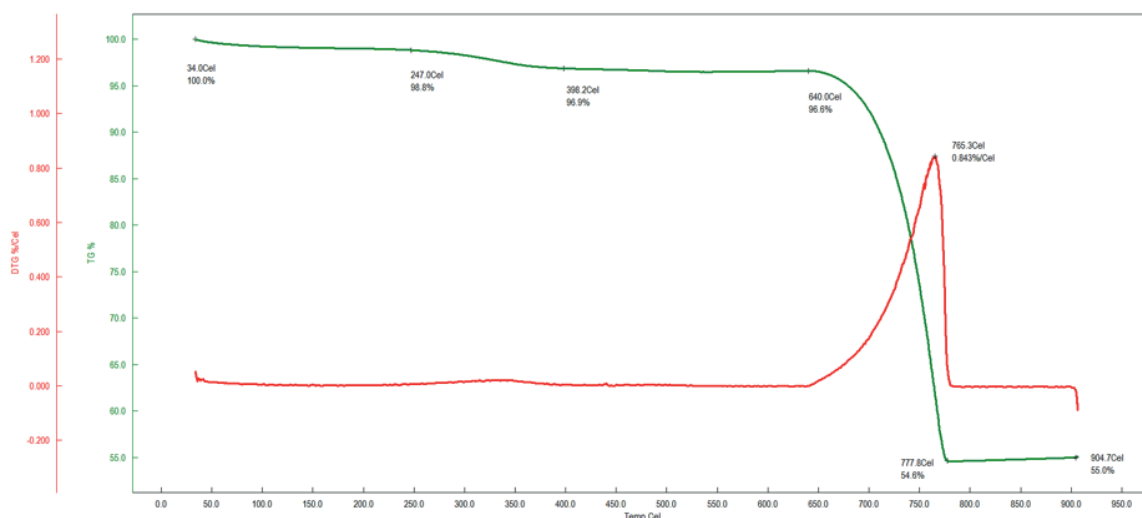


Figure 1. TGA thermogram of sea snail shells.

Structural characterization (FTIR analysis)

The FTIR spectra of the bioceramics and tissue scaffolds are presented in Figure 2. In the analysis of the spectra, the functional groups of the bioceramic powders sintered at 850°C for 4 hours were confirmed.

A phosphate group O–P–O bending mode was observed at 494, 528, 560, 609, 667 cm^{-1} and another bending band is detected at 471 cm^{-1} . P–O asymmetric stretching mode bands of the phosphate group were at 973, 1031, 1066, 1101, 1139, 1187, 1211 cm^{-1} . P–O–P symmetric stretching bands were obtained as medium intensity peaks at 726, 751 cm^{-1} . Similarly, the phosphate group P–O symmetric stretching vibration band at 954 cm^{-1} and harmonic overtone were detected at 1156 cm^{-1} . These findings can be attributed to the phosphate group that consists of the hydroxyapatite formulation of the synthesized bioceramic. On the other hand, the carbonate group function was also confirmed for the bioceramic with the following findings; a carbonate group stretching mode at 1415 cm^{-1} and a carbonate group bending mode at 1456 cm^{-1} . The characteristic peaks of PVA, the matrix of the composite, in the membrane were also observed. Hydroxyl (–OH) groups were indicated at 3272.61 cm^{-1} , and the alkyl group bands were observed at 2854.13 cm^{-1} for (– CH_3), 2916.81 cm^{-1} for (– CH_2) functional groups. The peak at 835.02 cm^{-1} is due to the (–C–C–) vibrations. A weak peak at 1700–1750 cm^{-1} , corresponding to the C=O (carbonyl group), can be due to residual acetic acid ester groups in PVA. The peak at 1718.26 cm^{-1} can be attributed to the hydrogen bonding between the carbonyl and hydroxyl groups in PVA chains, which occurs due to hydrophilic interactions (Hernández et al., 2024; Tüzün, 2023).

These bands can vary depending on the interactions of the composite parts. For example, the –OH vibration band of PVA was detected at 3272.61 cm^{-1} . When 1% GEL was added to a 10% PVA solution, no specific GEL peak was observed; however, the position of the PVA peaks shifted, and

their intensity increased. When examining the spectra of PVA and GEL, the —OH hydroxyl group at 3272.61 cm^{-1} was found in the same position for both polymers, which explains the superposition of the peaks. Nonetheless, the dominant effect of GEL on PVA caused the displacement of PVA peaks. This result confirms the successful formation of a composite material as explained in the similar studies in the literature (Bulus et al., 2020; Razzaq et al., 2021). The distinctive peaks of the functional groups of PVA, Gel and bioceramic materials are shown in Figure 2.

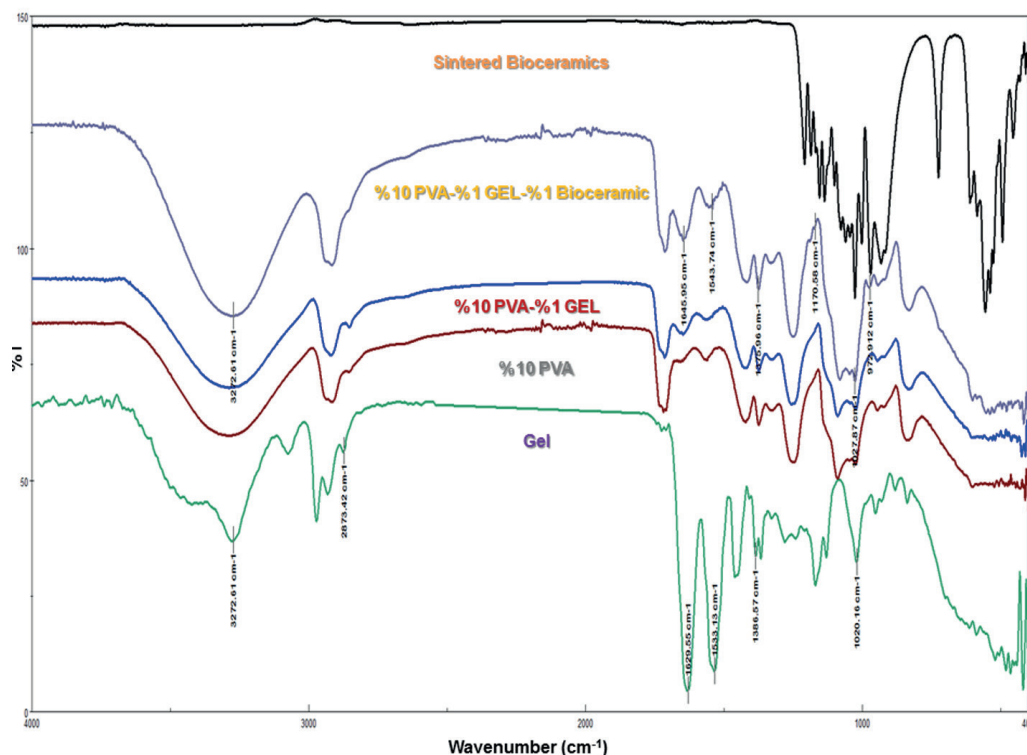


| **Figure 2.** FTIR spectra of bioceramics and scaffold composites.

Morphological characterization by FEGSEM analysis

When examining the FEGSEM morphological images of bioceramic powders synthesized from sea snail shells and sintered at 850°C for 4 hours (Figure 3), particles with various allotropic structures, including spherical, cubic, and needle-like forms, were observed (Buluş, 2017). These diverse particles exhibit high bioresorbability and bioactivity for a bioceramic (Biesuz et al., 2021).

The FEGSEM morphological analysis of the scaffolds (Figure 3) revealed that the fiber diameters of the 10:0 (PVA: GEL) sample ranged between 92 and 205 nm. The incorporation of 1% GEL produced the thinnest fibers observed in the study, with diameters measured between 72 and 142 nm. While the addition of 1% GEL promoted significant fiber thinning. Increasing the GEL content to 3% caused a rise in solution viscosity, leading to thicker fibers with diameters ranging from 145 to 308 nm. Moreover, the incorporation of 1% bioceramic into the 10% PVA/1% GEL composite resulted in nanofiber scaffolds with fiber diameters in the range of 85 to 280 nm. Among all the samples, the 10:1 (PVA: GEL) composite exhibited the thinnest average fiber diameter (Gautam et al., 2021). The mean fiber diameters for each scaffold composition are detailed in Table 3.

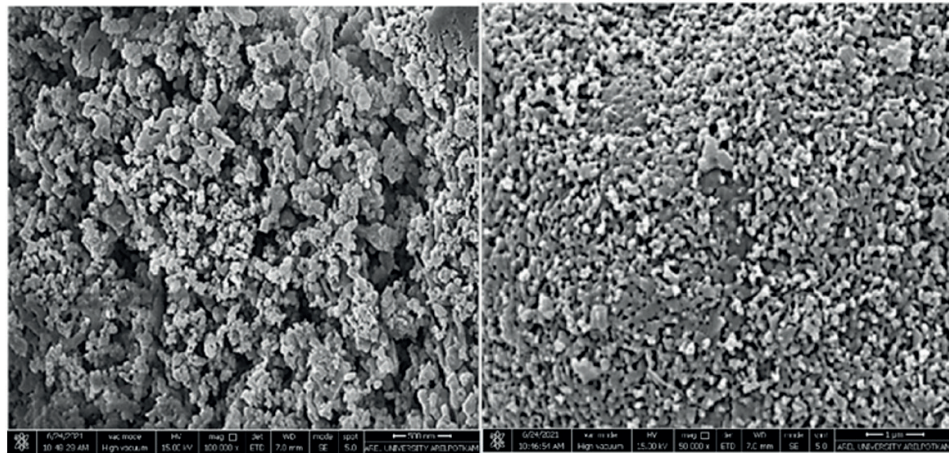


Figure 3. SEM Images of Bioceramic Powders Synthesized from Sea Snail Shells.

These findings underscore the critical role of additive materials in the composite, modulating the morphological properties of nanofiber scaffolds. Such insights are particularly valuable for advancing the design of scaffold materials in biomedical applications, where precise control over fiber dimensions is essential.

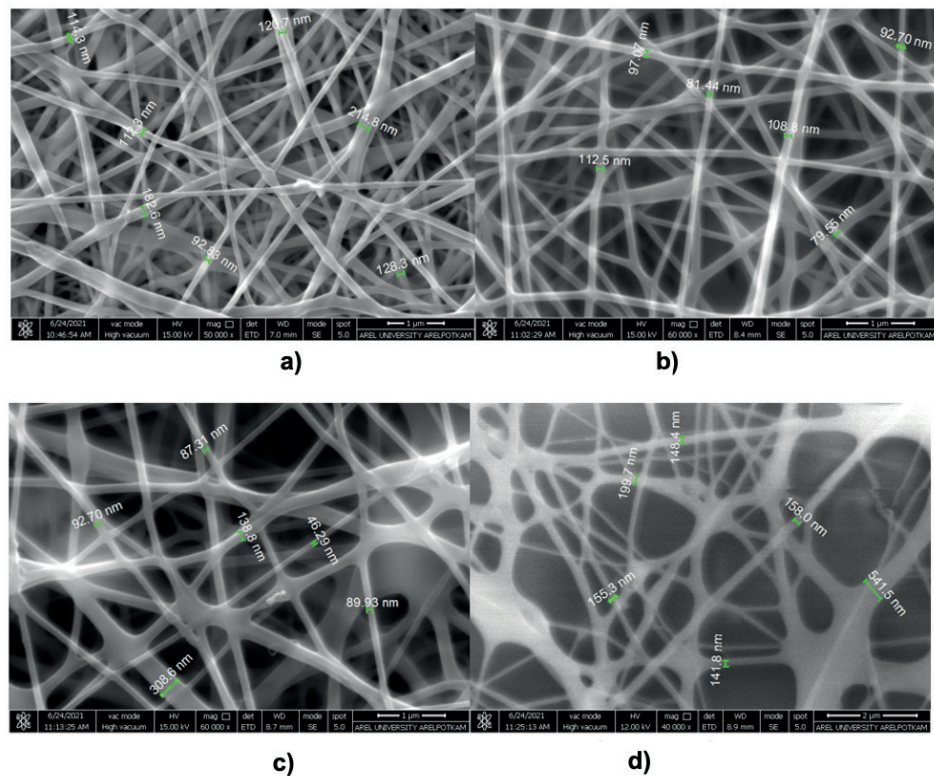


Figure 3. SEM images of tissue scaffolds a) 10:0 (PVA: GEL) b) 10:1 (PVA: GEL) c) 10:3 (PVA: GEL) d) 10:1:1(PVA: GEL: Bioceramics).

Table 3. Mean fiber diameters of tissue scaffolds.

Sample	Mean Fiber Diameter (nm)
10:0 (PVA: GEL)	92-205
10:1 (PVA: GEL)	72-142
10:3 (PVA: GEL)	145-308
10:1:1 (PVA: GEL:Bioceramics)	85-280

Mechanical characterization (Tensile test)

Tensile test results show that the 10:0 (PVA: GEL) sample exhibited a tensile strength of 6.25 MPa, which increased to 7.45 MPa with the addition of 1% GEL. The tensile strength in the 10:3 (PVA: GEL) sample was higher than that of the 10:1 (PVA: GEL) membrane. The gel is a protein-based polymer and has the capacity to form hydrogen bonds. PVA is also a polymer prone to hydrogen bonds. The increase in the gel ratio allows the formation of more hydrogen bonds in the PVA matrix. These bonds are thought to increase the mechanical strength of the nanofiber membrane by strengthening the interactions between the polymer chains (Qiao et al., 2015). Additionally, incorporation of 1% bioceramic into the 10% PVA/1% GEL composite further enhanced the tensile strength of the 10:1:1(PVA: GEL: Bioceramics) scaffolds. The strongest sample in the study was identified as the 10:1:1(PVA: GEL: Bioceramics) composite, achieving a tensile strength value of 8.22 MPa (Table 4).

Table 4. Tensile strenghts of the composite scaffolds.

Sample	Tensile Strength (MPa)
10:0 (PVA: GEL)	6.25
10:1 (PVA: GEL)	7.45
10:3 (PVA: GEL)	8.01
10:1:1(PVA:GEL:Bioceramics)	8.22

As a result of the homogeneous wrapping of the PVA-GEL nanofibers by the bioceramics, nanofibers with larger surface areas were obtained. This is an indication of the linear increase observed in the tensile strength of the membranes. Moreover, the addition of bioceramic material contributed to the reinforcement of the polymer fibers by integrating into the matrix and enhancing the fiber strength (Hejazi et al., 2021; Şahin,2019; Altan et al., 2024).These findings highlight the synergistic effect of GEL and bioceramic additives in optimizing the mechanical properties of nanofiber scaffolds, making them suitable for applications requiring enhanced structural integrity.

Conclusions

This study successfully synthesized bioceramics from sea snail shells through the chemical precipitation method. Using PVA, GEL, and bioceramic powders, nanofiber-structured tissue scaffolds were fabricated via the electrospinning technique. The methodology employed demonstrated the effective integration of bioceramic components into the polymer matrix, producing a composite material with desirable properties for tissue engineering applications. The results of the study indicate that the synthesized bioceramics, when incorporated into tissue scaffolds, yield a biomaterial with promising

characteristics, including ideal mechanical and structural properties. These scaffolds exhibited suitable porosity and nanofiber morphology, which are critical for mimicking the extracellular matrix and promoting cell adhesion, proliferation, and differentiation. The FTIR and SEM analyzes further confirmed the successful integration of bioceramics into the composite structure, demonstrating their compatibility with the polymer matrix and the maintenance of functional group integrity. The mechanical characterization results revealed that the composite scaffolds provide tensile strength, making them suitable for applications requiring load-bearing capacity, such as in bone and connective tissue regeneration. Moreover, the bioceramic component contributes to bioactivity and biocompatibility, facilitating interactions with surrounding tissues and promoting mineralization and osseointegration. Given these properties, it is anticipated that the composite scaffolds can serve as an interfacial layer in various tissue engineering applications. Their ability to create an environment conducive to cell adhesion and tissue regeneration suggests potential for use in dental applications, particularly for supporting bone and connective tissue formation. Additionally, the rapid biodegradability and bioresorbability of these scaffolds minimize long-term risks, making them a sustainable option for clinical applications. Future studies could focus on in vitro and in vivo assessments to further validate the bioactivity, biocompatibility, and mechanical performance of these scaffolds. Furthermore, exploring the scalability of the fabrication process and its adaptability to other bioceramic-polymer composites could pave the way for broader biomedical applications.

Acknowledgements

This research was supported by the Polymer Technologies and Composite Materials Research and Development Center (ArelPOTKAM) at Istanbul Arel University, Türkiye.

Funding

None.

Conflict of interest

The authors declare no conflict of interest.

Data availability statement

Data can be obtained from the corresponding author upon a reasonable request.

Ethics committee approval

Ethics committee approval is not required for this study.

Authors' contribution statement

The authors acknowledge their contributions to this paper as follows: **Study conception and design:** Y.M.S.; E.B.; **Data collection:** S.N.S., A.T.; **Analysis and interpretation of results:** S.N.S., A.T., E.B., M.U.F., M.A., Y.M.S.; **Manuscript draft preparation:** S.N.S., A.T., E.B., M.U.F., M.A., Y.M.S. All

authors reviewed the results and approved the final version of the manuscript.

Use of Artificial Intelligence: No artificial intelligence-based tools or applications were used in the preparation of this study. The entire content of the study was produced by the author(s) in accordance with scientific research methods and academic ethical principles.

ORCIDs and emails of the authors

Sema Nur Sahin | ORCID 0000-0003-3549-7646 | semanuursahin@gmail.com

Erdi Bulus | ORCID 0000-0002-2045-2499 | erdibulus@arel.edu.tr

Alper Tezcan | ORCID 0000-0002-4603-9061 | alpertezcan@arel.edu.tr

Muhammad Umar Farooq | ORCID 0000-0001-8804-9754 | ufbajwa@yahoo.com

Marwah Al-garash | meroalgarash@gmail.com

Yesim Muge Sahin | ORCID 0000-0003-2119-1216 | ymugesahin@arel.edu.tr

References

- Altan, D., Özarslan, A. C., Özel, C., Tuzlakoğlu, K., Sahin, Y. M., & Yücel, S. (2024). Fabrication of electrospun double layered biomimetic collagen–chitosan polymeric membranes with zinc-doped mesoporous bioactive glass additives. *Polymers*, 16(14), 2066–2084. <https://doi.org/10.3390/polym16142066>
- Aydogdu, M. O., Mutlu, B., Kurt, M., Inan, A. T., Kuruca, S. E., Erdemir, G., Sahin, Y.M., Ekren, N., Oktar, F.N., & Gunduz, O. (2019). Developments of 3D polycaprolactone/beta-tricalcium phosphate/collagen scaffolds for hard tissue engineering. *Journal of the Australian ceramic society*, 55, 849-855. <https://doi.org/10.1007/s41779-018-00299-y>
- Ba Linh, N. T., Lee, K. H., & Lee, B. T. (2013). Functional nanofiber mat of polyvinyl alcohol/gelatin containing nanoparticles of biphasic calcium phosphate for bone regeneration in rat calvaria defects. *Journal of biomedical materials research part A*, 101(8), 2412–2423. <https://doi.org/10.1002/jbm.a.34533>
- Biesuz, M., Galotta, A., Motta, A., Kermani, S., Grasso, J., Vontorová, V., Tyrpekl, M., Vilémová, M., & Sglavo, V. M. (2021). Speedy bioceramics: Rapid densification of tricalcium phosphate by ultrafast high-temperature sintering. *Materials science and engineering: C*, 127, 112246. <https://doi.org/10.1016/j.msec.2021.112246>
- Buluş, E. (2017). *Doğal izole edilmiş biyoseramiklerden elektrospinning yöntemi ile polimerik biyokompozit malzeme eldesi* (Master's thesis, Fen Bilimleri Enstitüsü).
- Bulus, E., Sakarya Bulus, G., & Sahin, Y. M. (2020). Production and characterization of nanotechnological tape for wounds caused by diabetes. *Journal of materials and electronic devices*, 5(1), 20–24.
- Cam, M. E., Cesur, S., Taskin, T., Erdemir, G., Kuruca, D. S., Sahin, Y. M., Kabasakal, L., & Gunduz, O. (2019). Fabrication, characterization and fibroblast proliferative activity of electrospun Achillea lycaonica-loaded nanofibrous mats. *European polymer journal*, 120, 109239. <https://doi.org/10.1016/j.eurpolymj.2019.109239>

[org/10.1016/j.eurpolymj.2019.109239](https://doi.org/10.1016/j.eurpolymj.2019.109239)

- Filippi, M., Born, G., Chaaban, M., & Scherberich, A. (2020). Natural polymeric scaffolds in bone regeneration. *Frontiers in bioengineering and biotechnology*, 8, 474. <https://doi.org/10.3389/fbioe.2020.00474>
- Gautam, S., Sharma, C., Purohit, S. D., Singh, H., Dinda, A. K., Potdar, C. F., Chou, P. D., & Mishra, N. C. (2021). Gelatin-polycaprolactone-nanohydroxyapatite electrospun nanocomposite scaffold for bone tissue engineering. *Materials science and engineering: C*, 119, 111588. <https://doi.org/10.1016/j.msec.2020.111588>
- Gunduz, O., Sahin, Y. M., Agathopoulos, S., Ağaoğulları, H., Gökçe, E. S., Kayali, C., Aktas, B., Ben-Nissan, B., & Oktar, F. N. (2013). Nano calcium phosphate powder production through chemical agitation from Atlantic deer cowrie shells (*Cypraea cervus Linnaeus*). *Key engineering materials*, 587, 80–85. <https://doi.org/10.4028/www.scientific.net/KEM.587.80>
- Hernández, G. R., Valdez, H. A., Arango-Ospina, M., Delgado, J. F., Aguilar-Rabiela, A. E., Gorgojo, J. P., Zhang, H., Beltrán, A.M., Boccaccini, A.R., & Sánchez, M. L. (2024). PVA-gelatine based hydrogel loaded with astaxanthin and mesoporous bioactive glass nanoparticles for wound healing. *Journal of drug delivery science and technology*, 101, 106235. <https://doi.org/10.1016/j.jddst.2024.106235>
- Hejazi, F., Bagheri-Khoulenjani, S., Olov, D., Zeini, A., Solouk, A., & Mirzadeh, H. (2021). Fabrication of nanocomposite/nanofibrous functionally graded biomimetic scaffolds for osteochondral tissue regeneration. *Journal of biomedical materials research part A*, 109(9), 1657–1669. <https://doi.org/10.1002/jbm.a.37161>
- Heydary, H. A., Karamian, E., Poorazizi, E., Heydaripour, J., & Khandan, A. (2015). Electrospun of polymer/bioceramic nanocomposite as a new soft tissue for biomedical applications. *Journal of asian ceramic societies*, 3(4), 417–425. <https://doi.org/10.1016/j.jascers.2015.09.003>
- Hong, J., Yeo, M., Yang, G. H., & Kim, G. H. (2019). Cell-electrospinning and its application for tissue engineering. *International journal of molecular sciences*, 20(24), 6208. <https://doi.org/10.3390/ijms20246208>
- Hoque, M. E., Sakinah, N., Chuan, Y. L., & Ansari, M. N. M. (2014). Synthesis and characterization of hydroxyapatite bioceramic. *International journal of scientific engineering and technology*, 3(5), 458–462.
- Howard, D., Buttery, L. D., Shakesheff, K. M., & Roberts, S. J. (2008). Tissue engineering: Strategies, stem cells and scaffolds. *Journal of anatomy*, 213(1), 66–72. <https://doi.org/10.1111/j.1469-7580.2008.00878.x>
- Jazayeri, H. E., Lee, S.-M., Kuhn, L., Fahimipour, F., Tahriri, M., & Tayebi, L. (2020). Polymeric scaffolds for dental pulp tissue engineering: A review. *Dental materials*, 36(2), e1–e10. <https://doi.org/10.1016/j.dental.2019.11.005>
- Keçeciler-Emir, C., Başaran-Elalmiş, Y. M., Şahin, Y., Buluş, E., & Yücel, S. (2023). Fabrication and characterization of chlorhexidine gluconate loaded poly (vinyl alcohol)/45S5 nano-bioactive glass nanofibrous membrane for guided tissue regeneration applications. *Biopolymers*, 114(10), e23562. <https://doi.org/10.1002/bip.23562>

- Linh, N. T., Min, Y. K., Song, H. Y., & Lee, B. T. (2010). Fabrication of polyvinyl alcohol/gelatin nanofiber composites and evaluation of their material properties. *Journal of biomedical materials research part B: applied biomaterials*, 95(1), 184–191. <https://doi.org/10.1002/jbm.b.31701>
- Mazumder, S., Nayak, A. K., Ara, T. J., & Hasnain, M. S. (2019). Hydroxyapatite composites for dentistry. In *Applications of nanocomposite materials in dentistry* (pp. 123–143). <https://doi.org/10.1016/B978-0-12-813742-0.00007-9>
- Perez-Puyana, V., Jiménez-Rosado, M., Romero, A., & Guerrero, A. (2018). Development of PVA/gelatin nanofibrous scaffolds for tissue engineering via electrospinning. *Materials research express*, 5(3), 035401. <https://doi.org/10.1088/2053-1591/aab164>
- Razzaq, A., Khan, Z. U., Saeed, A., Shah, K. A., Khan, N. U., Menaa, B., Iqbal, H., & Menaa, F. (2021). Development of cephradine-loaded gelatin/polyvinyl alcohol electrospun nanofibers for effective diabetic wound healing: *In vitro* and *in vivo* assessments. *Pharmaceutics*, 13(3), 349. <https://doi.org/10.3390/pharmaceutics13030349>
- Sadeghi, A., Pezeshki-Modaress, M., & Zandi, M. (2018). Electrospun polyvinyl alcohol/gelatin/chondroitin sulfate nanofibrous scaffold: Fabrication and *in vitro* evaluation. *International Journal of biological macromolecules*, 114, 1248–1256. <https://doi.org/10.1016/j.ijbiomac.2018.04.002>
- Sahin, Y. M. (2019). Natural nanohydroxyapatite synthesis via ultrasonication from *Donax trunculus* bivalve sea shells and production of its electrospun nanobiocomposite. *Acta physica polonica A*, 135(5), 1093–1096. <https://doi.org/10.12693/APhysPolA.135.1093>
- Sahin, Y. M., Orman, Z., & Yucel, S. (2018). *In vitro* studies of α -TCP and β -TCP produced from *Clinocardium ciliatum* seashells. *Journal of the Australian ceramic society*, 56, 477–488. <https://doi.org/10.1007/s41779-019-00355-1>
- Şahin, Y. M., Orman, Z., & Yücel, S. (2018). A simple chemical method for conversion of *Turritella terebra* sea snail into nanobioceramics. *Journal of ceramic processing research*, 19(6), 492–498. ISSN: 1229-9162
- Santhosh, S., & Balasivanandha Prabu, S. (2013). Thermal stability of nano hydroxyapatite synthesized from sea shells through wet chemical synthesis. *Materials letters*, 97, 121–124. <https://doi.org/10.1016/j.matlet.2013.01.081>
- Sengor, M., Ozgun, A., Corapcioglu, G., Ipekoglu, M., Garipcan, B., Ersoy, N., & Altintas, S. (2018). Core-shell PVA/gelatin nanofibrous scaffolds using co-solvent, aqueous electrospinning: Toward a green approach. *Journal of applied polymer science*, 135(32), 46582. <https://doi.org/10.1002/app.46582>
- Song, W., Markel, D. C., Wang, T., Shi, G., Mao, T., & Ren, W. (2012). Electrospun polyvinyl alcohol–collagen–hydroxyapatite nanofibers: A biomimetic extracellular matrix for osteoblastic cells. *Nanotechnology*, 23(11), 115101. <https://doi.org/10.1088/0957-4484/23/11/115101>
- Tüzün, E. (2023). Synthesis of novel antioxidant carboxymethylcellulose nanocomposites for Cu–Ni–Mo-based steel foams. *Cellulose*, 30(14), 8753–8768. <https://doi.org/10.1007/s10570-023-05436-w>
- Qiao, K., Zheng, Y., Guo, S., Tan, J., Chen, X., Li, J., Xu, D., & Wang, J. (2015). Hydrophilic nanofiber of bacterial cellulose guided the changes in the micro-structure and mechanical properties of

- nf-BC/PVA composites hydrogels. *Composites science and technology*, 118, 47-54. <https://doi.org/10.1016/j.compscitech.2015.08.004>
- Xie, W., Fu, X., Tang, F., Mo, Y., Cheng, J., Wang, H., & Chen, X. (2019). Dose-dependent modulation effects of bioactive glass particles on macrophages and diabetic wound healing. *Journal of materials chemistry B*, 7(6), 940–952. <https://doi.org/10.1039/C8TB02938E>
- Yelten-Yilmaz, A., & Yilmaz, S. (2010). Wet chemical precipitation synthesis of hydroxyapatite (HA) powders. *Ceramics international*, 44(8), 9703–9710. <https://doi.org/10.1016/j.ceramint.2018.02.201>
- Zhang, H., Xiong, Y., Dong, L., & Li, X. (2021). Development of hierarchical porous bioceramic scaffolds with controlled micro/nano surface topography for accelerating bone regeneration. *Materials science and engineering: C*, 130, 112437. <https://doi.org/10.1016/j.msec.2021.112437>
- Zou, Y., Zhang, L., Yang, F., Zhu, M., Ding, F., Lin, Z., Wang, Z., & Li, Y. (2018). 'Click' chemistry in polymeric scaffolds: Bioactive materials for tissue engineering. *Journal of controlled release*, 273, 160–179. <https://doi.org/10.1016/j.jconrel.2018.01.023>

RESEARCH ARTICLE

Identification of new candidate molecules against SARS-CoV-2 through docking studies

Punar Aliyeva¹  | Beyza Yilmaz²  | Doruk Alp Uzunarslan³  | Vildan Enisoglu Atalay^{4*} ¹ Uskudar University, Graduate School of Science, Department of Molecular Biology, 34662, Istanbul, Türkiye
ROR ID: 02dzjmc73² Uskudar University, Graduate School of Science, Department of Biotechnology, 34662, Istanbul, Türkiye
ROR ID: 02dzjmc73³ Uskudar American Academy, 34674, Istanbul, Türkiye⁴ Informatics Institute, Computational Science and Engineering, Istanbul Technical University, 34469, Istanbul, Türkiye
ROR ID: 059636586* Corresponding author: E-mail: enisogluatalayv@itu.edu.tr; Ph.: +90 (212) 444 1 488; Fax: +09 (212) 285 29 10

Citation: Aliyeva, P., Yilmaz, B., Uzunarslan, D.A., & Enisoglu-Atalay, V. (2025) Identification of new candidate molecules against SARS-CoV-2 through docking studies. *The European chemistry and biotechnology journal*, 4, 14–23.
<https://doi.org/10.62063/ecb-40>

License: This article is licensed under a Creative Commons Attribution-NonCommercial 4.0 International License (CC BY-NC 4.0).

Peer review: Double Blind Refereeing.

Ethics statement: It is declared that scientific and ethical principles were followed during the preparation of this study and all studies utilized were indicated in the bibliography (Ethical reporting: editor@euchembioj.com).

Plagiarism Check: Done (iThenticate).
Article has been screened for originality.

Received: 23.10.2024

Accepted: 16.05.2025

Online first: 27.05.2025

Published: 11.07.2025

Abstract

The recent outbreak of a new coronavirus disease known as COVID-19, caused by Severe Acute Respiratory Syndrome Coronavirus 2 (SARS-CoV-2), is a highly contagious and pathogenic viral infection that has spread worldwide. Coronaviruses are known to cause disease in humans, other mammals, and birds. Although specific therapeutics and vaccines require efforts in this direction, reaching the world's population with mutations of the virus can be a difficult target. The major proteases of coronavirus play a critical role during the spread of the disease and therefore still represent an important target for drug discovery. As of now, there is still no official treatment for infected patients. In this study, bioinformatics-based molecular docking studies were performed to identify potent inhibitors of novel candidate molecules against the spike protein S of SARS-CoV-2. The affinities of ligand molecules thought to be effective in the treatment of SARS-CoV-2 disease were investigated. For this purpose, 1,615 different FDA-approved drug ligand molecules were retrieved from ZINC15 database. Crystallographic structure of spike protein S of SARS-CoV-2 was retrieved from Protein Data Bank (PDB). Initial virtual screening was performed using *qvina-w*, an accelerated version of AutoDock Vina optimized for rapid docking, to evaluate binding affinities of all 1,615 compounds against the spike protein. The top 10 ligands with the most favorable binding affinities were selected for further analysis. These ligands were docked to the target protein with Autodock Vina. The complexes were first solvated and then run through Molecular Dynamics (MD) simulations, utilizing NAMD. The binding energies were computed through these interactions, which are used to compare the affinities of the ligands to the target protein. Ultimately, 10 different ligands



capable of inhibiting the spike protein of SARS-CoV-2 were selected and compared based on their affinities.

Keywords: Coronavirus, in silico, Molecular Docking, Drug Development

Introduction

The acute respiratory infection that we know as the novel coronavirus SARS-CoV-2 was first identified in Wuhan China in the year 2019 (Petersen et al. 2020). This infection is highly contagious and can be transmitted via droplet and contact. Coronavirus (CoV) belongs to the family Coronaviridae, suborder Cornidovirineae, and order Nidovirales. According to the phylogenetic analysis, the Coronaviridae family can be classified into 4 genera, namely alpha, beta, delta, and gamma (Payne 2017). Human and animal cells are both susceptible to infection by the single stranded RNA virus known as the coronavirus, which has a positive virulence. Human coronaviruses are among the rapidly evolving viruses, because of their high recombination rate and nucleotide element dominance (Fehr and Perlman 2015). Several recent reports, both genome wide and at the receptor level provided unique insights on many characteristics of the SARS-CoV-2 virus. One of these characteristics include the ability of different variants of SARS-CoV-2 to bind to Angiotensin-Converting Enzyme 2 (ACE2) cell receptors (Letko et al 2020). It is the binding of the spike protein (S) to the ACE2 receptor that allows SARS-CoV-2 to enter cells, as it facilitates the initiation of viral replication (Shang, J et al, 2020; Wang et al 2020).

SARS-CoV-2 is a virus with a long, single-stranded RNA genome, about 30,000 bases in length. This genome is one of the largest among all known RNA viruses, which boosts the virulence of the virus through reduced dependence on host cells for replication. The virus itself is small, measuring between 50-200 nanometers, and is covered with spike-like proteins that help invade human cells. SARS-CoV-2 is responsible for causing Severe Acute Respiratory Syndrome (SARS), which affects the respiratory system and can lead to serious complications (Payne, 2017). The symptoms of infection can vary widely among individuals. While some patients experience mild, cold-like symptoms, others suffer from severe respiratory distress or long-term complications, often referred to as “long COVID.” This variability in how the virus impacts individuals highlights the complexity of SARS-CoV-2 and its interactions with the human body.

Coronaviruses display spherical structure and include the following four main types of structural proteins; membrane (M), envelope (E), nucleocapsid (N) and spike (S) protein (Fehr and Perlman, 2015). Membrane protein lies within the range of 25 to 30 kDa and has three transmembrane N-terminal domains, a glycosylated ectodomain and a C terminal domain (Armstrong et al., 1984). The M protein is diamimic protein that fuses other outer structural proteins, foreboding the virus to bud out (Neuman et al., 2011). Envelope protein has an approximate mass of about 8 to 12 kDa (Schoeman and Fielding, 2019). The E protein consists of the N terminal ectodomain and C terminal endodomain (Nietto-Torres et al., 2014). The E protein increases the pathogenicity of the virus by acting on its ion channel as transmembrane proteins during the process of budding and the release of the virus (Li et al., 2014). The N protein has N terminal and C terminal domains.

The N protein is rich in phosphate esters and phosphates in general (Stohlgman and Lai, 1979). Because of the strong binding of N proteins to viral RNA, the N protein associates with the viral RNA genome and encapsulates it (Kuo and Masters 2013). The N protein assists in the packaging of the

viral RNA genome into the replicase-transcriptase complex (RTC) and afterwards the virus genome into the viral virus (Hurst et al. 2013).

Spike protein has a vital role in SARS-CoV-2 virus transmission (Shang et al., 2020). Attachment initiates with the trimetric spike protein's S1 subunit's interaction with ACE2 receptors in the heart, kidneys, and lungs (Hamming et al., 2004). S1 and S2 separation in the SARS-CoV-2 spike protein takes place owing to the presence of the proprotein convertase (PPC) section (Walls et al., 2020). The S protein is subsequently cleaved at the host cell membrane by the transmembrane serine protease 2 (TMPRSS2) which results in the release of S1 subunit while triggering the S2 subunit to become rearranged to a post-fusion conformation that assists in the merging of the viral and host cell membranes (Bestle et al., 2020). The peptide domain that is able to modulate this action comes from the S2 subunit and is activated via receptor recognition, allowing it to breach the host cell membrane (Xiu et al., 2020). Delta and Omicron variants have highlighted the importance of targeting conserved viral elements, as these variants exhibit increased transmissibility and resistance to neutralizing antibodies (Shuai et al., 2022).

The primary objective of molecular docking is to characterize and predict molecular recognition, through structural (identifying alternate binding modes) and energy-wise compatibility. Computer-based methods shorten the drug design process, providing low cost and speed drug development environments, while, contributing to the analysis of the interaction between ligands and the target protein structure by calculating the binding affinity (Kitchen et al., 2004). *In silico* studies, molecular docking in particular, have accelerated the identification of potential inhibitors targeting SARS-CoV-2 proteins. Examples include the identification of drugs that could bind to the spike protein receptor-binding domain through docking studies (Garg et al., 2021; Santos-Martins et al., 2021). Computational techniques have been employed for fast, affordable, and efficient compound screening, paving the way for drug discovery.

In this study, molecular docking simulations are used to identify novel molecules capable of inhibiting the spike protein found in SARS-CoV-2. By evaluating binding affinities and physicochemical properties of ligand candidates, this work aims to contribute to the ongoing efforts of developing therapeutic strategies against SARS-CoV-2 and its evolving variants. FDA-approved molecules identified as inhibitors of the relevant target structure through the ZINC15 database were included in the study as ligand molecules.

Materials and methods

To obtain the crystal structures of the proteins important for SARS-CoV-2, the ACE2-linked structure with PDB ID 6M0J (Figure 1) at 2.45 Å resolution was selected from the Protein Data Bank (<https://www.rcsb.org/>) database (Lan et al., 2020). In order to perform multiple docking operations in a concise manner, it was essential to define a specific region of interest on the protein surface where ligand binding is most likely to occur. The gridbox center coordinates for 6M0J were determined as x=-31.454, y=29.553, z=21.871 and a gridbox box with a size of 40x40x40 Å³ was determined. In this study, 1,615 different FDA-approved molecules were retrieved from the ZINC15 database (<https://zinc15.docking.org>). These molecules were then docked to the target protein. Through Autodock Vina, the binding affinities of the candidate molecules were scored and compared. The obtained physicochemical parameters of the ligand candidate molecules for effective treatment of SARS-CoV-2 disease were taken into consideration. All the docking studies were implemented using Autodock Vina (Eberhardt et al., 2021). After docking studies were performed, the interaction maps

of the ligands with the target protein structures were investigated in detail. The topmost 10 ligands were selected ranked by their binding affinities. These ligands were simulated for 2 nanoseconds using NAMD. Subsequently, the overall energy change was observed between the ligands and the target protein.

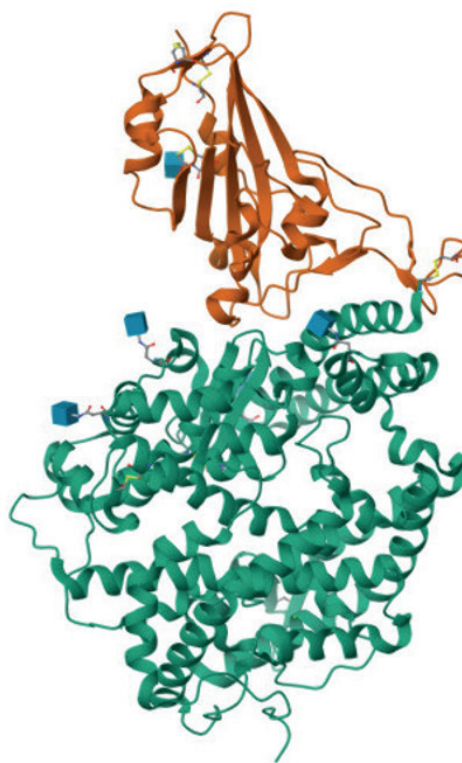


Figure 1. Crystal structure of SARS-CoV-2 spike receptor-binding domain bound with ACE2.

Results and discussion

Table 1 shows molecular weights and lipophilicities of candidate molecules that were docked against S spike protein of SARS-CoV-2. These physicochemical parameters, including molecular weight (Mw) and lipophilicity (logP), play a crucial role in determining the pharmacokinetic behavior of the ligands, such as absorption, distribution, and membrane permeability.

Table 1. Calculated Properties of the Investigated Ligands (Top 100 Ranked by Binding As

ZINC ID	Mw	logP	BE	ZINC000253387843	924.091	0.712	-8.7
ZINC000052955754	581.673	1.991	-10.1	ZINC000252286876	926.107	0.778	-8.7
ZINC000252286878	926.107	0.778	-9.7	ZINC000253630390	875.106	5.601	-8.6
ZINC000203757351	765.893	3.637	-9.2	ZINC000150338819	889.017	8.607	-8.4
ZINC000242548690	780.949	2.218	-9.1	ZINC000068202099	485.506	5.822	-8.2
ZINC000003927200	366.501	4.306	-8.8	ZINC000001530886	514.629	7.264	-8.2
ZINC000003978005	583.689	2.081	-8.8	ZINC000100378061	570.646	3.48	-8.2
ZINC000027990463	693.732	8.382	-8.8	ZINC000000968264	287.406	4.698	-8.2

ZINC000003784182	412.529	6.681	-8.2	ZINC000072318121	506.605	4.937	-7.6
ZINC000252286877	926.107	0.778	-8.2	ZINC000150338708	761.85	3.413	-7.6
ZINC000040430143	434.471	2.347	-8.1	ZINC000001612996	586.689	4.091	-7.5
ZINC000169621215	847.019	4.616	-8.1	ZINC000034089131	433.592	4.972	-7.5
ZINC000150588351	882.035	8.116	-8	ZINC000169621220	665.733	0.12	-7.5
ZINC000100013130	570.649	5.907	-8	ZINC000003882036	394.439	0.62	-7.5
ZINC000000538658	448.95	5.683	-8	ZINC000084758235	546.937	4.51	-7.5
ZINC000003985982	414.498	3.125	-8	ZINC000003860453	332.311	3.666	-7.5
ZINC000095617678	810.466	5.719	-8	ZINC000100073786	562.706	4.24	-7.5
ZINC000169289767	872.894	6.67	-8	ZINC000004074875	610.671	6.319	-7.5
ZINC000169621228	877.045	5.648	-8	ZINC000000897240	381.907	4.298	-7.5
ZINC000003932831	528.537	6.576	-8	ZINC000035902489	450.345	5.038	-7.5
ZINC000028232746	723.65	2.462	-7.9	ZINC000035328014	440.507	4.217	-7.5
ZINC000203686879	883.019	7.732	-7.9	ZINC000003816514	500.483	5.73	-7.5
ZINC000004175630	461.556	6.269	-7.9	ZINC000003920266	497.5	1.02	-7.5
ZINC000164528615	838.878	3.857	-7.9	ZINC000016052277	444.44	0.702	-7.5
ZINC000003918087	543.525	0.001	-7.8	ZINC000100017856	366.844	5.505	-7.5
ZINC000204073689	492.591	5.63	-7.8	ZINC000261527196	690.86	2.269	-7.5
ZINC000011681563	578.601	6.787	-7.8	ZINC000003993846	506.709	4.051	-7.5
ZINC000036701290	532.57	4.456	-7.8	ZINC000100370145	562.706	4.24	-7.5
ZINC000003927822	492.689	4.256	-7.8	ZINC000100013500	517.776	5.251	-7.4
ZINC000006716957	529.526	6.356	-7.8	ZINC000000643143	531.44	4.206	-7.4
ZINC000169621200	785.891	6.158	-7.8	ZINC000003931840	517.776	5.251	-7.4
ZINC000253632968	749.956	5.254	-7.8	ZINC000066166864	482.628	4.773	-7.4
ZINC000003872566	501.667	5.511	-7.7	ZINC000011617039	437.529	3.139	-7.4
ZINC000012503187	498.586	6.507	-7.7	ZINC000095551509	766.918	4.142	-7.4
ZINC000019632618	493.615	4.59	-7.7	ZINC000103105084	324.38	2.519	-7.4
ZINC000003831128	429.604	5.407	-7.7	ZINC000013831130	444.423	1.486	-7.4
ZINC000000538550	412.946	3.809	-7.7	ZINC000085537026	748.996	1.901	-7.4
ZINC000164760756	749.956	5.254	-7.7	ZINC000111460375	562.706	4.24	-7.4
ZINC000053683151	654.606	3.193	-7.7	ZINC000005844792	405.441	2.364	-7.4
ZINC000150338755	868.457	8.66	-7.7	ZINC000000004724	252.273	2.642	-7.4
ZINC000252286875	926.107	0.778	-7.7	ZINC000001539579	348.486	6.104	-7.4
ZINC000169621219	729.908	3.438	-7.7	ZINC000218037687	868.948	4.957	-7.4
ZINC000004213474	454.966	3.889	-7.6	ZINC000169621231	958.24	6.197	-7.4
ZINC000118912450	332.484	4.401	-7.6	ZINC000043207238	444.524	2.968	-7.4
ZINC000011616852	723.65	2.462	-7.6	ZINC000030691420	408.922	2.021	-7.4
ZINC000004213946	405.441	2.364	-7.6	ZINC000053683271	690.86	2.269	-7.4
ZINC000004214700	426.492	3.081	-7.6	ZINC000150601177	894.127	7.687	-7.4
ZINC000064033452	452.413	4.747	-7.6	ZINC000306122005	540.708	1.43	-7.4
ZINC000008220909	665.733	0.12	-7.6	ZINC000009574770	812.018	4.929	-7.3
ZINC000014261579	540.697	4.704	-7.6				
ZINC000169289388	914.187	6.181	-7.6				
ZINC000003917708	527.526	1.029	-7.6				

As demonstrated in Table 1, it is evident that the binding affinities of the candidate ligands to the S spike protein of SARS-CoV-2 vary significantly. -7.0 kcal/mol is acknowledged as a threshold for high protein-ligand binding affinity. As clearly shown on Table 1, multiple candidate ligands surpass this threshold with a relatively high margin. This underlines the fact that alternative options for highly affinitive ligands exist ubiquitously among FDA approved ligands.

Moreover, the 10 most suitable ligands compared based on Binding Affinities (kcal/mol) are put into molecular dynamics simulation for further analysis. The protein–ligand complex was subjected to a 2 nanosecond molecular dynamics simulation using Nanoscale Molecular Dynamics (NAMD) (Philips *et al.*, 2020). After the simulation was complete, visualization and trajectory analyses were performed using Visual Molecular Dynamics (VMD) (Humphrey, 1996). The system was solvated in a TIP3P water box, neutralized with counterions, and simulated under periodic boundary conditions using the CHARMM36 force field. Insights from these simulations will help identify ligands with both strong and stable interactions, potentially guiding future *in vitro* validation and drug repurposing efforts against SARS-CoV-2.

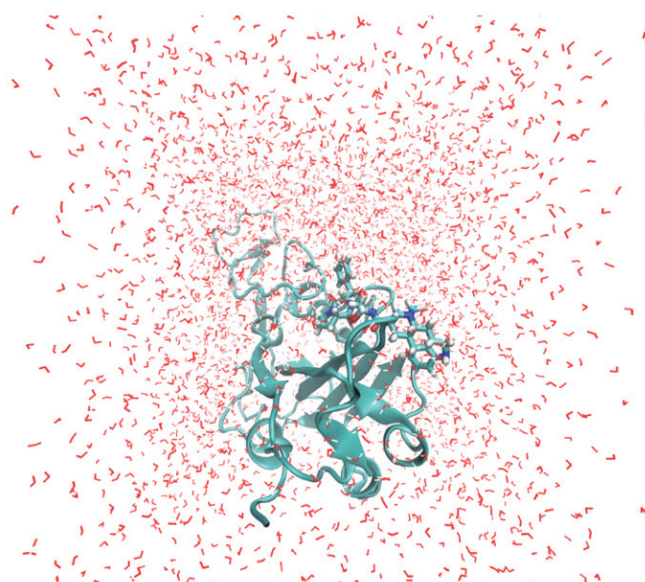


| **Figure 2.** ZINC000052955754 Docked to spike protein S of SARS-CoV-2.

Figure 2 shows the complex formed by ZINC000052955754 and spike protein S of SARS-CoV-2. Taking Table 1 into consideration, this ligand shows high binding affinity towards the spike protein of SARS-CoV-2. After this initial docking analysis, the complex was subjected to molecular dynamics simulation to evaluate the stability and behavior of the ligand within the binding pocket over time. Non-bonded interactions between the ligand and the protein were calculated through NAMD to provide a better viewpoint on the inhibition feature of the ligand. Calculated frame-by-frame, the mean of interaction energy was calculated as -62.811 kcal/mol. The negative value of the interaction energy suggests that the binding process is thermodynamically favorable and likely spontaneous under physiological conditions. This energy profile reinforces the notion that ZINC000052955754 forms a stable and energetically favorable complex with the spike protein.

Conclusions

This study identified potential candidate molecules for inhibiting the SARS-CoV-2 spike protein by molecular docking studies. Among the 1,615 compounds screened, the top ten candidates were further investigated through molecular docking and molecular dynamics simulations. The frequent and significant interactions between these ligands and the amino acids suggest their potential as inhibitors against SARS-CoV-2 spike protein. Furthermore, ligand with the ZINC ID of ZINC000052955754 demonstrated a strong and spontaneous interaction with the spike protein, supported by a mean interaction energy of -62.811 kcal/mol. These findings emphasize the potential of repurposing existing drugs as effective inhibitors of SARS-CoV-2. *In silico* methodologies applied in this study provide a cost-effective and efficient pathway for drug discovery. These results align with the understanding that structural compatibility between the ligand and active site is crucial for achieving high binding affinity. Moreover, the results reinforce the importance of structural complementarity and physicochemical optimization in achieving high-affinity protein–ligand interactions. Future work should focus on experimental validation through *in vitro* and *in vivo* assays to confirm the therapeutic potential of these candidates. Expanding the compound library and enhancing computational accuracy will further strengthen the applicability of such approaches in addressing current and emerging viral threats.

Acknowledgements

None.

Funding

None.

Conflict of interest

The authors declare no conflict of interest.

Data availability statement

Data can be obtained from the corresponding author upon a reasonable request.

Ethics committee approval

Ethics committee approval is not required for this study.

Authors' contribution statement

The authors acknowledge their contributions to this paper as follows: **Study conception and design:** P.A., B.Y., D.A.U., V.E.A.; **Data collection:** P.A., B.Y., D.A.U., V.E.A.; **Analysis and interpretation of results:** P.A., B.Y., D.A.U., V.E.A.; **Manuscript draft preparation:** P.A., B.Y., D.A.U., V.E.A. All authors reviewed the results and approved the final version of the manuscript.

Use of Artificial Intelligence: No artificial intelligence-based tools or applications were used in the preparation of this study. The entire content of the study was produced by the author(s) in accordance with scientific research methods and academic ethical principles.

ORCIDs and emails of the authors

Punar Aliyeva | ORCID 0000-0002-2868-0736 | pnar_aliyeva@mail.ru

Beyza Yilmaz | ORCID 0009-0007-5768-5070 | beyza.yilmaz@st.uskudar.edu.tr

Doruk Alp Uzunarslan | ORCID 0009-0001-4223-7984 | duzunarslan27@my.uaa.k12.tr

Vildan Enisoglu Atalay | ORCID 0000-0002-9830-9158 | enisogluatalayv@itu.edu.tr

References

















- Armstrong, J., Niemann, H., Smeekens, S., Rottier, P., & Warren, G. (1984). Sequence and topology of a model intracellular membrane protein, E1 glycoprotein, from a coronavirus. *Nature*, 308(5961), 751–752. <https://doi.org/10.1038/308751a0>
- Beniac, D. R., Andonov, A., Grudeski, E., & Booth, T. F. (2006). Architecture of the SARS coronavirus prefusion spike. *Nature Structural & Molecular Biology*, 13(8), 751–752. <https://doi.org/10.1038/nsmb1123>
- Bestle, D., Heindl, M. R., Limburg, H., Pilgram, O., Moulton, H., Stein, D. A., Harges, K., Eickmann, M., Dolnik, O., Rohde, C., Klenk, H. D., Garten, W., Steinmetzer, T., & Böttcher-Friebertshäuser, E. (2020). TMPRSS2 and furin are both essential for proteolytic activation of SARS-CoV-2 in human airway cells. *Life Science Alliance*, 3(9), e202000786. <https://doi.org/10.26508/lsa.202000786>
- Bhattacharya, S., Banerjee, A., & Ray, S. (2021). Development of new vaccine target against SARS-CoV2 using envelope (E) protein: An evolutionary, molecular modeling and docking based study. *International Journal of Biological Macromolecules*, 172, 74–81. <https://doi.org/10.1016/j.ijbiomac.2020.12.192>
- Bosch, B. J., Van der Zee, R., De Haan, C. A., & Rottier, P. J. (2003). The coronavirus spike protein is a class I virus fusion protein: Structural and functional characterization of the fusion core complex. *Journal of Virology*, 77(16), 8801–8811. <https://doi.org/10.1128/JVI.77.16.8801-8811.2003>
- Daina, A., Michielin, O., & Zoete, V. (2017). SwissADME: A free web tool to evaluate pharmacokinetics, drug-likeness and medicinal chemistry friendliness of small molecules. *Scientific Reports*, 7, 42717. <https://doi.org/10.1038/srep42717>
- Eberhardt, J., Santos-Martins, D., Tillack, A. F., & Forli, S. (2021). AutoDock Vina 1.2.0: New docking methods, expanded force field, and python bindings. *Journal of Chemical Information and Modeling*, 61(8), 3891–3898. <https://doi.org/10.1021/acs.jcim.1c00203>
- Fehr, A. R., & Perlman, S. (2015). Coronaviruses: An overview of their replication and pathogenesis. In H. J. Maier, E. Bickerton, & P. Britton (Eds.), *Coronaviruses: Methods and Protocols* (pp. 1–23). Humana Press. https://doi.org/10.1007/978-1-4939-2438-7_1
- Frenoy, P., Perduca, V., Cano-Sancho, G., Antignac, J. P., Severi, G., & Mancini, F. R. (2022). Application of two statistical approaches (Bayesian Kernel Machine Regression and Principal Component Regression) to assess breast cancer risk in association to exposure to mixtures of brominated flame retardants and per- and polyfluorinated alkylated substances in the E3N cohort. *Environmental Health*, 21(1), 27. <https://doi.org/10.1186/s12940-022-00817-0>
- Garg, M., Maralakunte, M., Garg, S., Dhooria, S., Sehgal, I., Bhalla, A. S., Vijayvergiya, R., Grover, S., Bhatia, V., Jagia, P., Bhalla, A., Suri, V., Goyal, M., Agarwal, R., Puri, G. D., & Sandhu, M. S. (2021). The conundrum of ‘Long-COVID-19’: A narrative review. *International Journal of General Medicine*, 14, 2491–2506. <https://doi.org/10.2147/IJGM.S316708>

- Hamming, I., Timens, W., Bulthuis, M. L. C., Lely, A. T., Navis, G. V., & van Goor, H. (2004). Tissue distribution of ACE2 protein, the functional receptor for SARS coronavirus. A first step in understanding SARS pathogenesis. *The Journal of Pathology*, 203(2), 631–637. <https://doi.org/10.1002/path.1570>
- Humphrey, W., Dalke, A., & Schulten, K. (1996). VMD - Visual Molecular Dynamics. *Journal of Molecular Graphics*, 14(1), 33–38. [https://doi.org/10.1016/0263-7855\(96\)00018-5](https://doi.org/10.1016/0263-7855(96)00018-5)
- Hurst, K. R., Koetzner, C. A., & Masters, P. S. (2013). Characterization of a critical interaction between the coronavirus nucleocapsid protein and nonstructural protein 3 of the viral replicase-transcriptase complex. *Journal of Virology*, 87(16), 9159–9172. <https://doi.org/10.1128/JVI.01075-13>
- Kamimura, A., Umemoto, H., Kawamoto, T., & Honda, T. (2021). Development of water solubility of 2-phenylsulfanylhydroquinone dimer dye. *ACS Omega*, 6(13), 9254–9262. <https://doi.org/10.1021/acsomega.1c00507>
- Kitchen, D. B., Decornez, H., Furr, J. R., & Bajorath, J. (2004). Docking and scoring in virtual screening for drug discovery: Methods and applications. *Nature Reviews Drug Discovery*, 3(11), 935–949. <https://doi.org/10.1038/nrd1549>
- Kumawat, P., Agarwal, L. K., & Sharma, K. (2024). An overview of SARS-CoV-2 potential targets, inhibitors, and computational insights to enrich the promising treatment strategies. *Current Microbiology*, 81, 169. <https://doi.org/10.1007/s00284-024-03615-1>
- Kuo, L., & Masters, P. S. (2013). Functional analysis of the murine coronavirus genomic RNA packaging signal. *Journal of Virology*, 87(9), 5182–5192. <https://doi.org/10.1128/JVI.03478-12>
- Lan, J., Ge, J., Yu, J., Shan, S., Zhou, H., Fan, S., Zhang, Q., Shi, X., Wang, Q., Zhang, L., & Wang, X. (2020). Structure of the SARS-CoV-2 spike receptor-binding domain bound to the ACE2 receptor. *Nature*, 581(7807), 215–220. <https://doi.org/10.1038/s41586-020-2180-5>
- Letko, M., Marzi, A., & Munster, V. (2020). Functional assessment of cell entry and receptor usage for SARS-CoV-2 and other lineage B betacoronaviruses. *Nature Microbiology*, 5(4), 562–569. <https://doi.org/10.1038/s41564-020-0688-y>
- Li, Y., Surya, W., Claudine, S., & Torres, J. (2014). Structure of a conserved Golgi complex-targeting signal in coronavirus envelope proteins. *Journal of Biological Chemistry*, 289(18), 12535–12549. <https://doi.org/10.1074/jbc.M113.528487>
- Molinspiration. (2015). Calculation of molecular properties and bioactivity score. <http://www.molinspiration.com/cgi-bin/properties>
- Neuman, B. W., Kiss, G., Kunding, A. H., Bhella, D., Baksh, M. F., Connelly, S., Droese, B., Klaus, J. P., Makino, S., & Buchmeier, M. J. (2011). A structural analysis of M protein in coronavirus assembly and morphology. *Journal of Structural Biology*, 174(1), 11–22. <https://doi.org/10.1016/j.jsb.2010.11.021>
- Nieto-Torres, J. L., DeDiego, M. L., Verdiá-Báguena, C., Jimenez-Guardeño, J. M., Regla-Nava, J. A., Fernandez-Delgado, R., Castano-Rodriguez, C., Alcaraz, A., Torres, J., Aguilera, V. M., & Enjuanes, L. (2014). Severe acute respiratory syndrome coronavirus envelope protein ion channel activity promotes virus fitness and pathogenesis. *PLoS Pathogens*, 10(5), e1004077. <https://doi.org/10.1371/journal.ppat.1004077>

- Payne, S. (2017). Family Coronaviridae. In *Viruses* (pp. 149–158). Academic Press. <https://doi.org/10.1016/B978-0-12-803109-4.00017-9>
- Petersen, E., Koopmans, M., Go, U., Hamer, D. H., Petrosillo, N., Castelli, F., Storgaard, M., Al Khalili, S., & Simonsen, L. (2020). Comparing SARS-CoV-2 with SARS-CoV and influenza pandemics. *The Lancet Infectious Diseases*, 20(9), e238–e244. [https://doi.org/10.1016/S1473-3099\(20\)30484-9](https://doi.org/10.1016/S1473-3099(20)30484-9)
- Phillips, J. C., Hardy, D. J., Maia, J. D. C., Stone, J. E., Ribeiro, J. V., Bernardi, R. C., Buch, R., Fiorin, G., Hénin, J., Jiang, W., McGreevy, R., Melo, M. C. R., Radak, B. K., Skeel, R. D., Singharoy, A., Wang, Y., Roux, B., Aksimentiev, A., Luthey-Schulten, Z., Kalé, L. V., Schulten, K., Chipot, C., & Tajkhorshid, E. (2020). Scalable molecular dynamics on CPU and GPU architectures with NAMD. *The Journal of Chemical Physics*, 153(4), 044130. <https://doi.org/10.1063/5.0014475>
- Rarey, M., Wefing, S., & Lengauer, T. (1996). Placement of medium-sized molecular fragments into active sites of proteins. *Journal of Computer-Aided Molecular Design*, 10(1), 41–54. <https://doi.org/10.1007/BF00124466>
- Rogers, D. M., Agarwal, R., Vermaas, J. V., Durrant, J. D., Welborn, V. V., Kireev, D., & Luthey-Schulten, Z. (2023). SARS-CoV2 billion-compound docking. *Scientific Data*, 10, 173. <https://doi.org/10.1038/s41597-023-02148-0>
- Schoeman, D., & Fielding, B. C. (2019). Coronavirus envelope protein: Current knowledge. *Virology Journal*, 16, 69. <https://doi.org/10.1186/s12985-019-1182-0>
- Sharma, V., Rai, H., Gautam, D. N. S., Prajapati, P. K., & Sharma, R. (2022). Emerging evidence on Omicron (B.1.1.529) SARS-CoV-2 variant. *Journal of Medical Virology*, 94(5), 1876–1885. <https://doi.org/10.1002/jmv.27526>
- Stohlgan, S. A., & Lai, M. M. (1979). Phosphoproteins of murine hepatitis viruses. *Journal of Virology*, 32(2), 672–675. <https://doi.org/10.1128/jvi.32.2.672-675.1979>
- Walls, A. C., Park, Y. J., Tortorici, M. A., Wall, A., McGuire, A. T., & Veesler, D. (2020). Structure, function, and antigenicity of the SARS-CoV-2 spike glycoprotein. *Cell*, 181(2), 281–292.e6. <https://doi.org/10.1016/j.cell.2020.02.058>
- Wang, Q., Qiu, Y., Li, J. Y., Zhou, Z. J., Liao, C. H., & Ge, X. Y. (2020). A unique protease cleavage site predicted in the spike protein of the novel pneumonia coronavirus (2019-nCoV) potentially related to viral transmissibility. *Virologica Sinica*, 35, 337–339. <https://doi.org/10.1007/s12250-020-00206-5>
- Wang, Y., Grunewald, M., & Perlman, S. (2020). Coronaviruses: An updated overview of their replication and pathogenesis. In H. J. Maier, E. Bickerton, & P. Britton (Eds.), *Coronaviruses: Methods and Protocols* (pp. 1–29). Humana. https://doi.org/10.1007/978-1-0716-0327-7_1
- Xia, S., Liu, M., Wang, C., Xu, W., Lan, Q., Feng, S., Qi, F., Bao, L., Du, L., Liu, S., Qin, C., Sun, F., Shi, Z., Zhu, Y., Jiang, S., & Lu, L. (2020). Inhibition of SARS-CoV-2 (previously 2019-nCoV) infection by a highly potent pan-coronavirus fusion inhibitor targeting its spike protein that harbors a high capacity to mediate membrane fusion. *Cell Research*, 30(4), 343–355. <https://doi.org/10.1038/s41422-020-0305-x>
- Xiu, S., Dick, A., Ju, H., Mirzaie, S., Abdi, F., Cocklin, S., Zhan, P., & Liu, X. (2020). Inhibitors of SARS-CoV-2 entry: Current and future opportunities. *Journal of Medicinal Chemistry*, 63(21), 12256–12274. <https://doi.org/10.1021/acs.jmedchem.0c00502>

RESEARCH ARTICLE

Correlation of ferritin, D-dimer, and CRP with disease severity and outcome in COVID-19 patients

Ia Murvanidze ¹  | Ilia Nakashidze ¹  | Teona Gogitidze ²  | Ermira Jahja ³ 
 Aleena Parveen Shaikh ¹  | Nino Tebidze ⁴  | Nameera Parveen Shaikh ⁴ 
 Besik Kakabadze ¹  | Maia Resulidze ¹  | Rajneesh Khurana ⁵  | Eteri Saralidze ¹ 
 Otar Tsetskhladze ¹  | Davit Baratashvili ¹  | Nino Kedelidze ¹  | Tamar Peshkova ¹ 
 Irina Nakashidze ^{1*} 

¹ Faculty of Natural Sciences and Health Care, Batumi Shota Rustaveli State University, **Batumi, Georgia**
 ROR ID: [0212gyx73](https://orcid.org/0212gyx73)

² BAU International University Batumi, **Batumi, Georgia**
 ROR ID: [03dw28302](https://orcid.org/03dw28302)

³ Faculty of Dental Medicine, Department of Basic Sciences, Western Balkans University, **Tirana, Albania**

⁴ School of Dental Medicine, BAU International University **Batumi, Batumi, Georgia**
 ROR ID: [03dw28302](https://orcid.org/03dw28302)

⁵ Montefiore Medical Center, Wakefield campus, **NY, United States**
 ROR ID: [044ntvm43](https://orcid.org/044ntvm43)

* **Corresponding author:** E-mail: irinanakashidze@yahoo.com, irina.nakashidze@bsu.edu.ge; Ph.: +599593 72 36 77

Citation: Murvanidze, I., Nakashidze, I., Gogitidze, T., Java, E., Shaikh, A.P., Tebidze, N., Shaikh, N.P., Kakabadze, B., Resulidze, M., Khurana, R., Saralidze, E., Tsetskhladze, E., Baratashvili, D., Kedelidze, N., Peshkova, T., & Nakashidze, I. (2025). Correlation of ferritin, D-dimer, and CRP with disease severity and outcome in COVID-19 patients. *The European chemistry and biotechnology journal*, 4, 24-39.
<https://doi.org/10.62063/ecb-59>

License: This article is licensed under a Creative Commons Attribution-NonCommercial 4.0 International License (CC BY-NC 4.0).

Peer review: Double Blind Refereeing.

Ethics statement: It is declared that scientific and ethical principles were followed during the preparation of this study and all studies utilized were indicated in the bibliography (Ethical reporting: editor@euchembioj.com).

Plagiarism Check: Done (iThenticate). Article has been screened for originality.

Received: 21.05.2025
Accepted: 23.06.2025
Online first: 27.06.2025
Published: 11.07.2025

Abstract

Higher levels of ferritin were associated with severe forms of COVID-19 disease. Given the above, our goal was to investigate the associations between ferritin levels within COVID-19-infected individuals from the Adjara population (Georgia). A nasopharyngeal swab was collected from 318 individuals, and SARS-CoV-2 infection was detected using the polymerase chain reaction (PCR) method. Ferritin levels were also investigated in the blood serum of the same individuals. Thus, the study of ferritin in COVID-19 patients (in the Adjara population) revealed significantly higher ferritin levels in COVID-19 patients. Higher levels of ferritin were detected in the male subjects than in the female population ($p=0.0001$). COVID-19 patients with lethal outcomes had nearly ~3 times higher levels of ferritin than the reference value, while those who successfully recovered had ~1.9 times above the reference value. It should be noted that the individuals with lethal outcomes were between 81 and 90 years old. An increased level of D-dimer compared to the reference level was also detected in the male population and was nearly ~4.1 times higher in those with lethal outcomes. D-dimer was also significantly increased in patients at the age 71-80 years, while their CRP levels were approximately ~5.8 times above the reference level; Moreover, CRP level was ~24.4 times increased in the case of women with lethal outcomes; In particular, according to the comparing age groups, a high level of CRP



was observed in 61-70 years patients. Our study revealed that the diseased population exhibited significantly higher ferritin levels. The ferritin levels in patients with lethal outcomes were considerably higher than those in patients who successfully recovered. Thus, the findings reveal a noteworthy elevation in D-dimer levels, particularly in men and deceased patients, with a notable elevation in the 71-80 age group. Additionally, CRP levels were markedly higher, especially among deceased women and individuals aged 61-70.

Keywords: Ferritin, COVID-19, Recovered patients, Lethal outcome

Introduction

Ferritin is often increased in acute inflammatory conditions. It is also known to act as an acute-phase reactant and contribute to immune dysregulation in severe cases of COVID-19. This suggests that ferritin may not only indicate the presence of inflammation but also actively participate in the cytokine storm observed in severe forms of COVID-19 (Kappert et al., 2020). The interaction between ferritin and cytokines may involve intricate feedback mechanisms in regulating pro-inflammatory and anti-inflammatory mediators. Cytokines can stimulate ferritin expression and vice versa; ferritin can also induce the expression of both pro- and anti-inflammatory cytokines (Ruddell et al., 2009).

Highly elevated levels of ferritin are a hallmark of hyperserotonemia syndromes, which include several severe medical conditions, such as macrophage activation syndrome, catastrophic antiphospholipid syndrome, adult-onset Still's disease, and septic shock (Colafrancesco et al., 2020). Generally, high ferritin levels in hospitalised patients are associated with poor prognosis (Shakaroun et al., 2023). In addition, studies have linked elevated levels of ferritin and other pro-inflammatory markers in COVID-19 with negative outcomes (Shakaroun et al., 2023). Consequently, researchers are investigating various anti-inflammatory biological agents to control the strong immune response in COVID-19 patients. However, whether ferritin can be used as a reliable predictor of outcomes in COVID-19 patients is yet to be determined.

A study conducted on a sample of 20 COVID-19 patients revealed interesting findings regarding serum ferritin levels in individuals with varying degrees of COVID-19 severity (Cheng et al., 2020). The results of this study indicated that patients with severe and very severe COVID-19 exhibited higher levels of serum ferritin than those with mild or moderate disease. Specifically, the group of patients with very severe COVID-19 had significantly higher serum ferritin levels than those with severe COVID-19, with a median of 1006.16 ng/mL versus 291.13 ng/mL, respectively (Vargas-Vargas & Cortés-Rojo 2020). These findings suggest that serum ferritin levels could help identify COVID-19 patients with severe disease and monitoring disease progression. Additionally, elevated levels of ferritin in COVID-19 patients could indicate the presence of a severe secondary bacterial infection and may indicate poor prognosis (Vargas-Vargas & Cortés-Rojo 2020).

The measures of ferritin levels in patients infected with COVID-19 may be crucial for disease prediction. Hyperferritinemia, often accompanied by a cytokine storm, is especially noticeable in acute COVID-19 patients with other inflammatory factors (Hadi et al., 2022). It is well established that the study of ferritin is a current issue across various fields. Among these, ferritin serves as a potential prognostic marker for individuals infected with COVID-19 (Para et al., 2022). Taking this into account, our goal was to study ferritin, D-dimer and CRP in patients with COVID-19.

Materials and methods

The study sample consisted of 318 patients with COVID-19. In addition to biological material, the patient's anamnesis, discharge and death epicrisis were studied. As about the comorbidities, from patients: Arterial hypertension: women: 40%; men: 57%; insulin-dependent diabetes: 33% women; men: 60%; heart disease: women: 28%, men: 79%. The gold standard polymerase chain reaction (PCR) method was used to detect COVID-19 infection. It is performed in single, high-tech laboratories. Nasopharyngeal swabs were used as the test material.

Blood serum was used as the test material for ferritin determination. (Analyser name: BECKMAN COULTER. Reference value: 10-150; M.20.9-350.0 ng/ml; Number of patients: 318; Blood plasma was used as the test material for D-dimer determination. Blood plasma was used as the test material. The turbidometer method was used to determine the amount of D-dimer (Name of the analyser: Finecare Wondfo Fluorescent Immunochromatographic Analysis System. Reference value: 0-500; Number of patients: -310); C-reactive protein was evaluated using immunoturbidimetry methods on a modern automated analyser, the Cobas c311 from Roche. The number of patients: 318.

Statistical analysis was performed using GraphPad Prism 10. version program. The following tests were used: 1. Column descriptive statistics, t-tests; $P < 0.05$ was considered statistically significant.

Results and discussion

As mentioned above, elevated ferritin levels detected in COVID-19 patients correlated with the disease's severity. Thus, ferritin is essential for assessing the disease's ongoing course and the correct treatment management. (Gómez-Pastora et al., 2020). Therefore, we studied the ferritin (FRT) level in patients infected with COVID-19. In the studied population, the levels were ~1.8 times higher among male patients than in female patients (Figure 1).

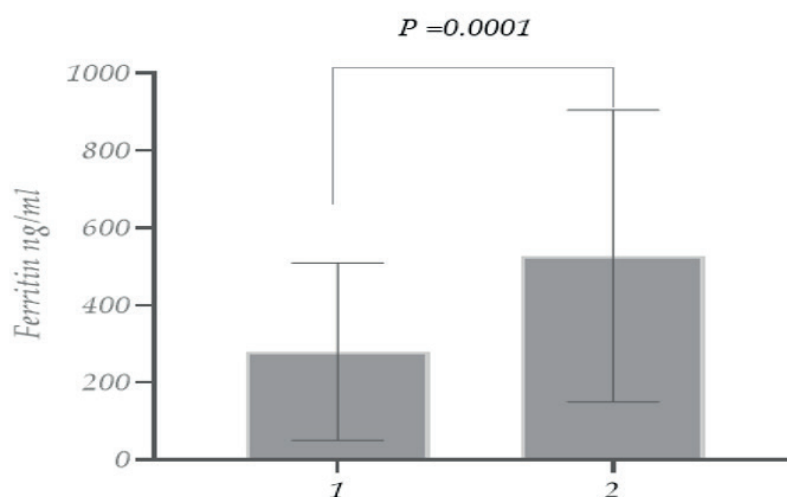


Figure 1. Ferritin level in patients with COVID-19 (1. Females; 2. Males).

As for ferritin levels in the case of recovered and deceased female patients, the levels of ferritin were ~ 3 times higher in patients with lethal outcomes (Figure 2).

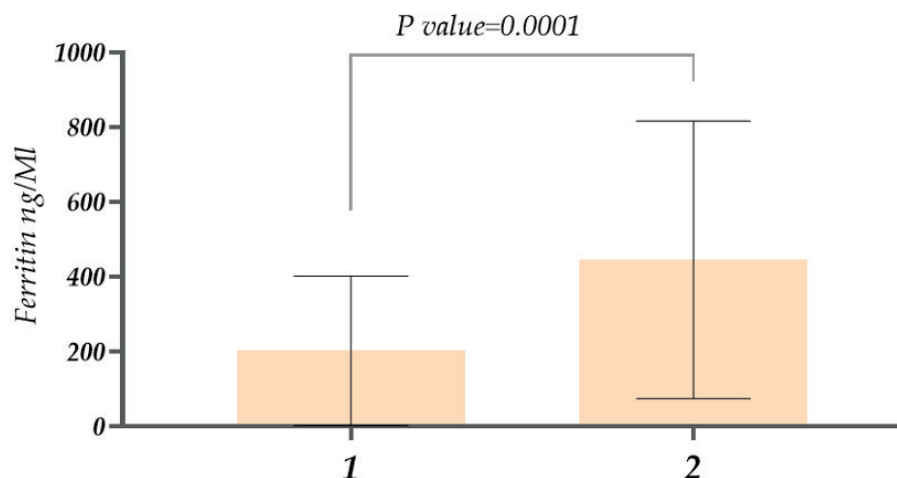


Figure 2. Study of ferritin count with COVID-19 (Female patients) (1. recovered; 2. deceased).

Regarding ferritin levels in men, the concentration was ~1.9 times higher in deceased male patients than in recovered patients (Figure 3). In addition to comparing genders, we also studied the ferritin level variations in different age groups. The research showed that in the case of 11-20-year-olds, ferritin was nearly ~1.3 times higher compared with younger patients between 1-10 years old. Similarly, in 21-30-year-old patients, ferritin levels were approximately 5.5 times higher compared with 11-20-year-olds. Considering patients aged 31-40 years, ferritin levels were ~1.3 times higher than in patients aged 21-30 years. A relatively low ferritin level was observed in 41-50-year-old patients, then there was an increase again in patients aged 51-60 years old. As for 71-80 year old patients, it was ~1.7 times higher than in 61-70 year old patients. And finally, the highest level of ferritin was detected in the case of 81-90-year-old patients. It is also noteworthy that a statistically significant difference was revealed between the 11-20 and 21-30 age groups when other age groups ($P=0.0001$)

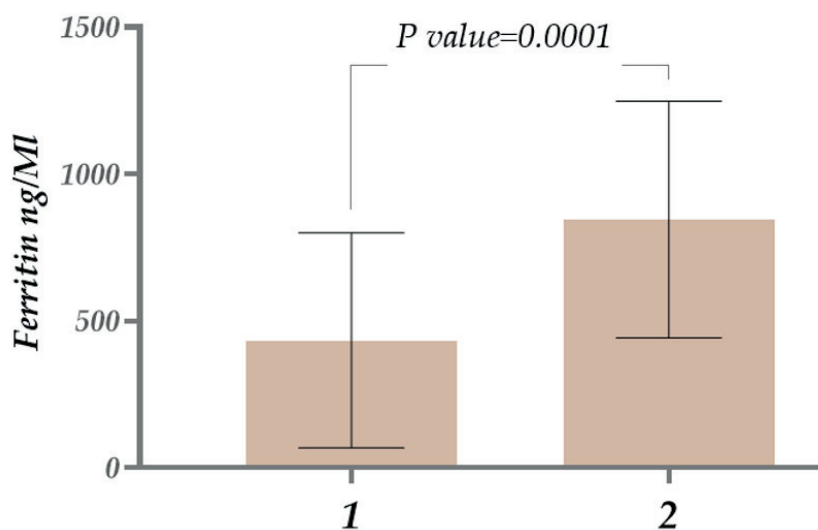


Figure 3. Study of ferritin levels in patients with COVID-19 (male patients) (1. recovered; 2. deceased).

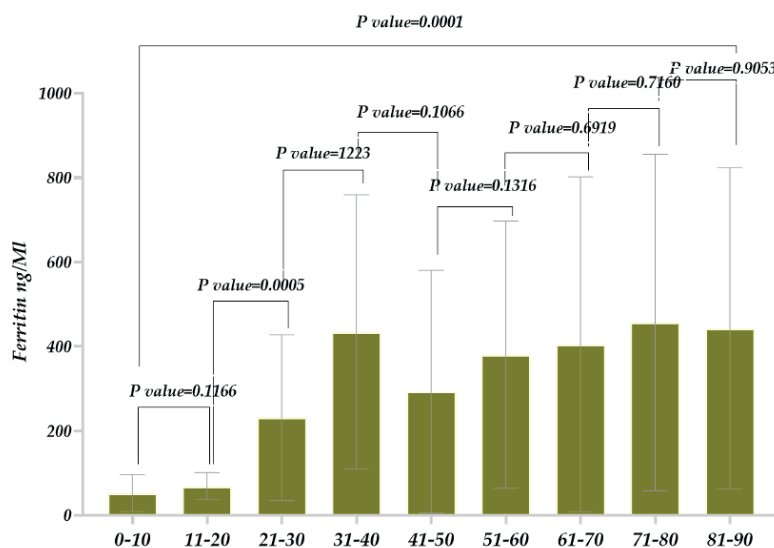


Figure 4. Ferritin level in patients with COVID-19 (different age groups).

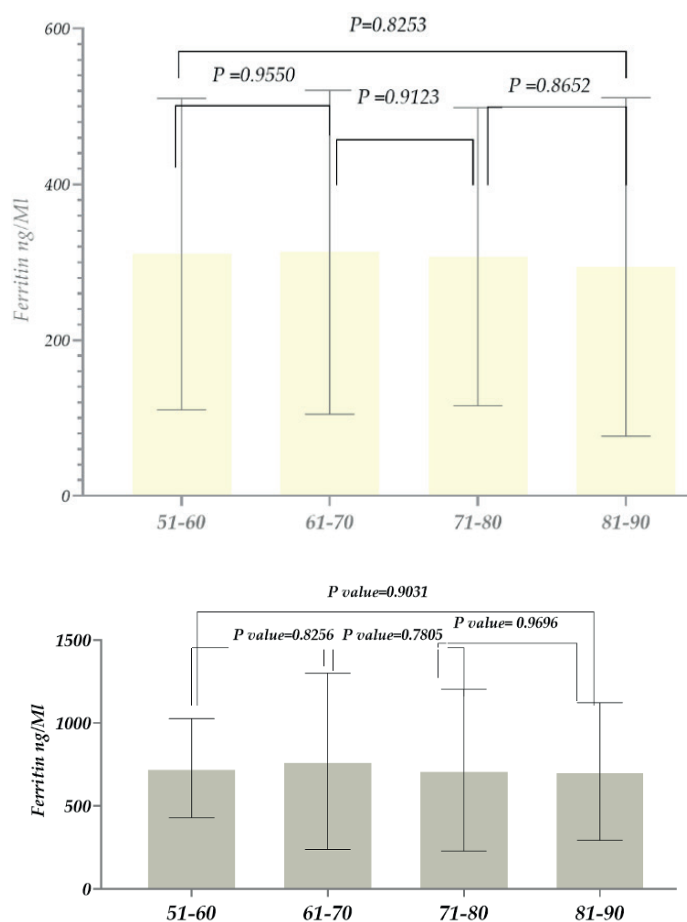


Figure 5. Ferritin level in patients with COVID-19 (different age groups) A. Recovered patients b. Deceased patients.

The study of ferritin among recovered patients (both female and male patients) showed that, in the case of surviving patients, the level of ferritin was consistent across all age groups (51-60 years: 310.5, 200; 61-70 years: 312.8, 207; 71-80 years: 312.8, 191.4; 81-90 years: 294, 217.2) (**Figure 5A**). In contrast, for deceased patients, the level of ferritin increased by 2.3, 2.46, 2.6, and 2.4 times compared to the corresponding age groups of surviving patients (**Figure 5A and B**). Notably, the ferritin level was highest in patients aged 71-80 years (**Figure 11B**). The inflammation during COVID-19 may represent part of the spectrum of hyperinflammatory syndromes. Furthermore, it is plausible that a common underlying pathogenic background could be successfully used to develop therapeutics targeting inflammatory mediators. (Colafrancesco et al., 2020). Infected patients may benefit if ferritin plays a pathogenic role as a mediator of COVID-19, thereby reducing ferritin and cytokine levels in SARS-CoV-2. Thus, ferritin monitoring during hospitalisation helps to identify severe patients/the possibility of controlling disease progression/possibly predicting clinical deterioration (Gómez-Pastora et al. 2020).

Considering the above, we also studied the D-dimer level in the case of patients suffering from COVID-19, along with ferritin. As the study results showed, the D-dimer level compared to its reference level was ~2 times higher within COVID-19 patients. It should also be noted that the levels were similar among both female and male patients (**Figure 6A**).

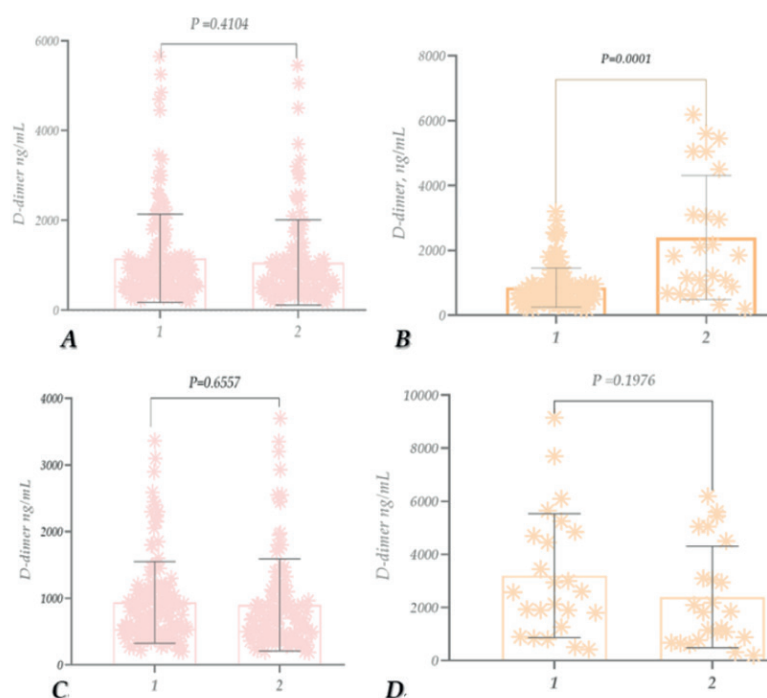


Figure 6. A D-dimer (DD) level in patients with COVID-19. A (1. females; 2. males); B, D-dimer (DD) levels in patients with COVID-19 -Males (1. recovered; 2. deceased); C, D-dimer (DD) levels in patients with COVID-19- recovered (1. females; 2. males); D, D-dimer (DD) levels in patients with COVID-19- deceased (1. females; 2. males).

As for the D-dimer levels in recovered and deceased female patients, the D-dimer level was high in both cases, ~1.8 and 4.6 times higher than the reference norm. As for the difference between recovered and

deceased patients, the level in deceased patients increased ~4.1 times (compared to recovered patients) (Figure 6 B). In the case of male patients, the D-dimer levels were also high, ~1.7 times and 4.7 times higher than the reference level. The level was ~2.8 times higher in deceased patients than in recovered patients (Figure 6C). The level of D dimer in recovered patients (Female and male patients) was almost the same, and it increased ~1.8 times compared to the reference norm (Figure 6D.); in deceased patients (female and male patients) its level increased by ~6.4 and ~4.7 times compared to normal (Figure 6D).

The study of D-dimer at different ages showed that its level was high (compared to the reference level) in all age groups: 51-60 years (~1.7), 61-70 years (~2.11), 71-80 years (~2.064), and 81-90 years (~2.37). However, the rate was highest in the 81-90 years age group (Figure 7A). For deceased patients, the level was exceptionally high compared to recovered patients in all age groups (3039 ng/mL, 2256 ng/mL, 3209 ng/mL, and 2220 ng/mL). However, it was particularly high in 71-80-year-old patients. Those 61-60 years old are noteworthy (Figure 7 B.).

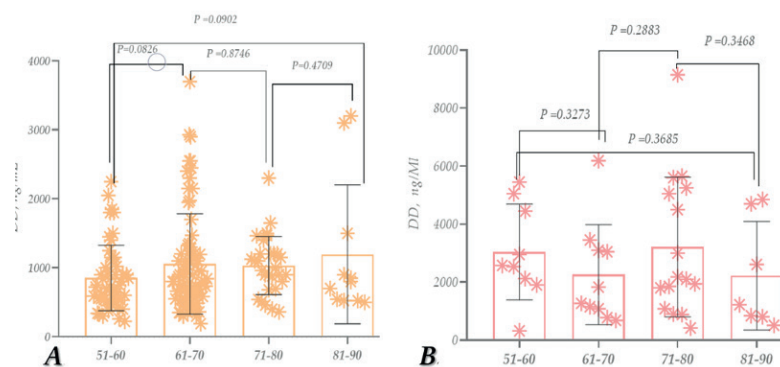


Figure 7. D-dimer (DD) levels in patients with COVID-19 recovered (A); D-dimer (DD) levels in patients with COVID-19 – deceased (B).

According to the study, the CRP level increased by approximately ~9.6-Times and 14 times compared to the reference norm. It is also noteworthy that the level was higher in male patients (Figure 8A). The CRP level, compared to its reference level, increased ~5.8-times for recovered patients and around ~24.4 times for deceased patients (female patients). Additionally, it increased by about 4.1 times in the case of deceased patients compared to healthy patients (Figure 8B).

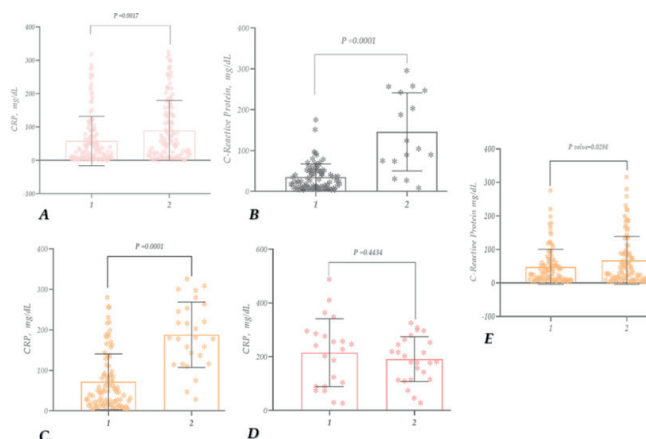


Figure 8. CRP study in patients with COVID-19 (1. females, 2. males) (A); CRP study in patients with COVID-19 – Females (1. recovered 2. deceased) (B); CRP study in patients with COVID-19 – males (1. recovered 2. deceased) (C); CRP study in dead patients with COVID-19 (1. females, 2. males) (D); CRP study in recovered patients with COVID-19 (1. females, 2. males) (E).

In the case of male patients, the CRP level in recovered patients was ~11.6-times higher, and ~31.3 times higher in deceased patients, compared to the reference norm. Regarding the difference between recovered and deceased patients, the CRP level increased by ~2.6-times (Figure 8C). When analysing the CRP levels of deceased patients, their rate had increased compared to the reference, especially in female patients (Figure 8D).

No statistically significant difference was observed in comparing the CRP indicator between age groups in recovered patients (Figure 9A); however, it was detected in deceased patients (Figure 9B). In patients who died at the ages of 81-90, 71-80, 61-70, and 51-60, the CRP levels were ~4.3, 4.4, 3.5, and 2.1 times higher, respectively, compared to those who had recovered (compared to the corresponding age groups).

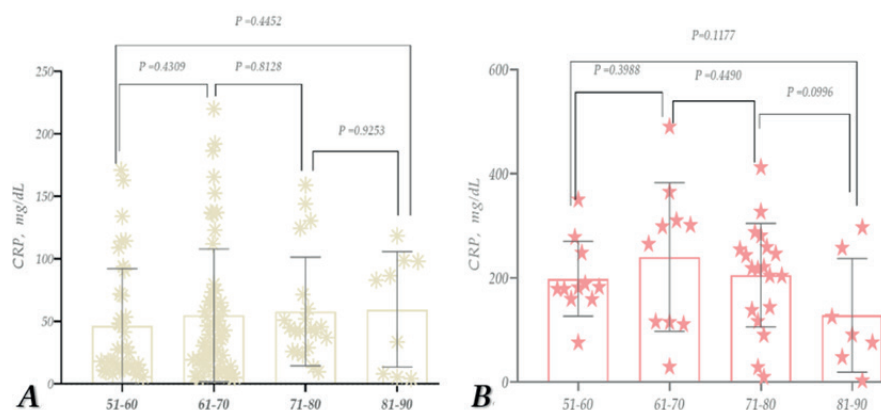


Figure 9. CRP study in patients with COVID-19 -recovered (females, males) (A); CRP study in patients with COVID-19 -deceased (females, males) (B).

Thus, according to the study, the CRP level is elevated in patients infected with COVID-19, especially in the case of deceased female patients. When comparing age groups, the significant representation of individuals aged 61-70 is noteworthy. In patients, this age group was also notably high compared to all other age groups and recovered patients of their corresponding age (Figure 9).

The study supports the idea that high ferritin levels indicate a poor prognosis for COVID-19 patients. Zhou et al. (2020a) conducted a retrospective, multicentre cohort study to examine the clinical course of COVID-19 patients, including laboratory biomarkers. The study included a total of 191 patients, of whom 137 were discharged (survivor group) and 54 died (deceased group) while in the hospital. The findings revealed that serum ferritin levels were significantly higher in non-survivors compared to survivors at the time of admission (median: 1435.3 vs. 503.2 µg/L, $p < 0.0001$). Furthermore, the median serum ferritin levels exceeded the upper limit of detection after day 16 of hospitalisation in these

patients, indicating a continuous increase in ferritin levels. The results suggest that serum ferritin is a valuable biomarker for predicting clinical outcomes in patients with COVID-19. The elevated levels of ferritin observed in non-survivors may indicate that these patients are more susceptible to developing an inflammatory storm linked to severe illness and mortality in COVID-19. The study provides important insights into the role of ferritin in COVID-19 pathogenesis and emphasises the significance of monitoring this biomarker in patients with COVID-19 (Zhou et al., 2020a; Carubbi et al., 2021). Chen et al. (2020) conducted a retrospective study on 99 COVID-19-infected patients, out of which 63 showed significantly elevated serum ferritin levels beyond the normal range during the infection (Chen et al., 2020). Additionally, autopsies of 12 patients who died from SARS-CoV-2 infection also exhibited elevated ferritin levels (Fox et al., 2020). Several studies have investigated the relationship between ferritin levels and comorbidities in patients with COVID-19. One such study aimed to investigate the impact of diabetes mellitus as a risk factor contributing to the poorer prognosis of COVID-19. The study collected and analysed data from 174 consecutive patients with confirmed COVID-19. The patients were divided into diabetic and non-diabetic cases based on their medical history, with 37 diabetic cases and 137 non-diabetic cases. To ensure that no biases are present in the study due to other medical factors, patients with pre-existing conditions apart from diabetes were not considered to be a part of this research. The assessment revealed that cases had increased levels of ferritin compared with controls (764.8 vs. 128.9 µg/L), respectively ($p < 0.01$). The investigation found similar disparities in ESR levels, D-dimer, CRP, and IL6. While patients with other pre-existing conditions also had elevated serum ferritin levels, these increases were not as significant. Furthermore, it concluded that activation of the monocyte-macrophage system, contributing to an inflammatory storm, can be demonstrated through elevated ferritin levels. These results suggest that cases were more prone to hyperinflammatory response, potentially leading to rapid deterioration and a poor outcome for COVID-19-infected patients (Guo et al., 2020). Moreover, there is an association between ferritin levels and severe, life-threatening COVID-19 cases. Liu et al. (2020) analysed peripheral blood samples from patients with advanced COVID-19 and compared them with non-advanced COVID-19 controls. An advanced level of infection was indicated by elevated ferritin levels, demonstrating a close association (Liu et al., 2020). Moreover, laboratory findings showed an immune system over-activation with elevated inflammatory biomolecules, including ferritin (Mehta et al., 2020). Although most studies found a strong association, some studies contradict significant findings on ferritin levels and COVID-19 severity. Feld et al. reported that levels of ferritin obtained throughout the disease or at specific durations were not a strong predictor of evaluated outcomes, including all-cause mortality, new mechanical ventilation, and the need for kidney transplantation. Based on this study's data, it can be concluded that while higher ferritin levels are linked with deaths throughout the course of an disease, they cannot be used as a reliable predictor for several significant outcomes, such as death. (Feld et al., 2020). Since the outbreak of COVID-19, D-dimer has become a potential biomarker for prognosis and treatment management in clinical settings. Elevated D-dimer levels and normal fibrinogen levels are a hallmark of coagulopathy in COVID-19. This condition is associated with high inflammation during COVID-19 illness, which can lead to mortality and morbidity due to thrombotic complications.

In severe or critical COVID-19 patients, D-dimer levels are significantly higher than in mild/moderate patients. This suggests a markedly high inflammation and consumptive coagulation state (Liu et al., 2020). D-dimer levels can help predict the risk of complications in COVID-19 patients, such as venous thromboembolism (VTE). By measuring D-dimer levels at admission, healthcare professionals

can identify patients at high risk for developing VTE and strategically manage them to prevent further complications (Nauka et al., 2021). Several studies have found that high levels of D-dimer at admission are associated with poor outcomes and in-hospital mortality in COVID-19 patients (Poudel et al., 2021).

Tang et al. conducted a retrospective analysis and reported that deceased COVID-19 patients had higher levels of D-dimer, fibrinogen degradation products (FDP), and prothrombin time (PT) at the time of admission than those who survived the disease. D-dimer levels can serve as an essential biomarker for predicting the risk of complications and mortality in COVID-19 patients. By monitoring and managing D-dimer levels, healthcare professionals can improve patient outcomes and prevent further complications. In non-survivors, a marked increase in D dimer levels ($> 15.0 \mu\text{g/mL}$) and decreasing levels of antithrombin III are associated with progressive consumptive coagulopathy and critical disease (Tang et al., 2020). Additionally, high D dimer levels ($>1 \mu\text{g/mL}$) have been linked to a significant increase in mortality (18 times higher) compared to those with lower levels among COVID-19 patients (Zhou et al., 2020b). Moreover, patients with high D dimer levels ($>3 \mu\text{g/mL}$) are unresponsive to prophylactic treatment for VTE (Maatman et al., 2020). Patients with COVID-19 pneumonia are at high risk of developing acute pulmonary embolism (APE) if they have elevated levels of D-dimer, which is a serious condition associated with mortality (Santos-Poleo et al., 2020). Although the pathophysiology behind the development of APE in COVID-19 patients is still being studied, all patients with elevated D-dimer levels should undergo Computed Tomography Pulmonary Angiography (CTPA) to rule out this clinical suspicion and initiate early treatment. A study by Sakka et al. recommended using D-dimer levels to sort COVID-19 patients at the time of admission to efficiently manage clinically severe patients (Sakka et al., 2020). Monitoring its levels can facilitate timely treatment initiation for high-risk patients. Additionally, D-dimer testing is a cost-effective laboratory procedure. Initially known to cause only respiratory distress and illness, it has now been ascertained that the virus can affect any organ and lead to organ dysfunction. There have been several studies to find the most suitable biomarkers reflecting the disease severity and predicting the prognosis. As the infection is a hyperinflammatory state, several markers that reflect the inflammatory state in the body have risen in these patients. A cytokine storm is the appropriate word for the surplus increase in the markers, leading to complications in multiple organs (Ceci et al., 2022). Although, why some patients fall critically ill while others don't remain a topic of great interest and an unsolved puzzle. But, out of many markers, three important ones that might predict the severity of the disease are: CRP, Ferritin, and D-Dimer. These markers can increase in the blood within 6-10 hours of any tissue damage (Black et al., 2004). There is mounting evidence that these can be used as diagnostic and prognostic markers; hence, hospitals have also used these in their practice accordingly when measured at the right time. These markers can help in proper resource allocation and management if critical patients, especially in the context of respiratory support (Wang et al., 2020; Gao et al., 2020; Linarez Ochoa et al., 2022).

Acute phase proteins or reactants (APRs) are a class of proteins that increase or decrease during the process of inflammation. Physiologically, the level of positive APRs is higher than the negative APRs. Positive APRs include Albumin, Transferrin, etc., and negative APRs include CRP, Fibrinogen, Ferritin, Procalcitonin, etc. During inflammation, where normal physiology is disrupted, negative APRs go up and hence can be used as a marker for an inflammatory state. CRP is an acute-phase reactant produced by the liver that can get elevated in multiple inflammatory, autoimmune, and cardiovascular conditions (Sproston and Ashworth, 2018). D-dimer is a fibrin degradation product that

signifies breakdown of clots in the body. Studies have reported that COVID-19 infection can induce formation of microthrombi in different vessels of the body, especially that of the lungs and the brain (Luo et al., 2020). 3.75–68.0% of the COVID-19 patients have been found to have raised D-dimer levels (Wu et al., 2020). Ferritin is an iron storage molecule generally, but like CRP also has a role on an acute phase reactant. Haematological changes occurring in COVID-19 were demonstrated. As per the meta-analysis performed by Huang et al (2020) elevated serum CRP was associated with an increased composite poor outcome [RR 1.84 (1.45, 2.33), $p < 0.001$; I²: 96%, $p < 0.001$] that included severe COVID-19 [RR 1.41 (1.14, 1.74), $p = 0.002$; I²: 93%, $p < 0.001$], need for ICU care [RR 1.96 (1.40, 2.74), $p < 0.001$], but not mortality [RR 2.95 (0.90, 9.68), $p = 0.07$; I²: 99%, $p < 0.001$] (Huang et al., 2020). Elevated D-dimer reflected increased mortality amongst those patients. In 10 studies, it was found that hyperferritinemia was seen in fatal cases rather than just severe cases (Huang et al., 2020). It is also important to denote that besides ferritin, D-dimer and CRP, there are some other potential biomarkers and potential targets for the treatment of Sars-CoV-2 that may be also applied and used to predict severity of SARS-CoV-2 infection, especially the ones associated with ferritin, D-dimer, CRP, and ferritin, and inflammatory mediators. For example, some miRNAs that were initially described in various tumor models, such as miR-19a-3p/19b-3p, and miR-92a-3p or miR-16-5p (Feng et al., 2014; Ghafouri-Fard et al., 2022) are described with a good potential to be used as biomarkers for early stage of SARS-CoV-2 infections, as well as reviewed and listed by Ergun et al. (2023) such as miR-146a/155/18a-5p/133/21-5p also linked with the disease severity (Ergun et al., 2023). For example, miR-92a-3p was especially found to be decreased in critically ill patients (De Gonzalo-Calvo et al., 2021). The same authors, observed association between miRNAs miR-92a-3p, miR-16-5p, miR-451a/486-5p/150-5p with ferritin and D-dimer, while CRP was found to be in a correlation with miR-27a-3p/27b-3p/451a/148a-3p/491-5p and miR-199-5p (De Gonzalo-Calvo et al., 2021) indicating that miRNA up or downregulation and targeting may be one of the mechanisms for additional treatment of SARS-CoV-2. Another study regarding liver function of COVID-19-infected patients revealed that the high creatinine levels are associated with the severity of COVID-19 disease (Murvanidze et al., 2023).

Thus, the study of ferritin in patients suffering from COVID-19 (using the population of Adjara as an example) revealed a significantly higher ferritin level than the reference level in the diseased population. A relatively high level of ferritin was detected in the samples of men compared to women. Regarding the level of ferritin in the deceased, a ~3 times and a ~1.9 times higher level was detected in female patients compared to those who recovered, and in men, respectively. As for the highest level of ferritin in the case of dead patients, the latter was observed in patients aged 81-90 years. An increased level of D-dimer compared to the reference level was detected; Its level is especially elevated in men; And as for its amount in deceased patients, it has increased ~4.1 times; D-dimer level is significantly increased at the age of 71-80 years; The level of CRP is ~5.8 times higher compared to the reference level; Moreover, CRP level increased ~24.4 times in case of dead women; In particular, according to the comparing age groups, a high level of CRP was observed in 61-70 years' patients. Future treatment modalities should not only rely on symptomatic therapy but also gene therapy, specifically modulating molecules such as miRNAs.

Conclusions

Our study revealed that the diseased population exhibited significantly higher ferritin levels. The ferritin levels in patients with lethal outcomes were considerably higher than those in patients who

successfully recovered. Thus, the findings reveal a noteworthy elevation in D-dimer levels, particularly in men and deceased patients, with a notable elevation in the 71-80 age group. Additionally, CRP levels were markedly higher, especially among deceased women and individuals aged 61-70.

Acknowledgements

None

Funding

None

Conflict of interest

The authors declare no conflict of interest.

Data availability statement

Data can be obtained from the corresponding author upon a reasonable request.

Ethics committee approval

The study was approved by the National Council on Bioethics of Georgia and written informed consent was obtained from all subjects.

Authors' contribution statement

The authors acknowledge their contributions to this paper as follows: **Study conception and design:** I.N.; **Data collection:** I.M., T.G., N.T.; **Analysis and interpretation of results:** I.M., M.R., II.N., **Manuscript draft preparation:** I.N., E.J., T.P., A.P.S., N.P.S., R.K., B.K., O.T., E.S., D.B., N.K. All authors reviewed the results and approved the final version of the manuscript.

Use of Artificial Intelligence: No artificial intelligence-based tools or applications were used in the preparation of this study. The entire content of the study was produced by the author(s) in accordance with scientific research methods and academic ethical principles.

ORCIDs and emails of the authors

Ia Murvanidze | ORCID 0000-0002-2351-9177 | murvanidze.ia@gmail.com

Ilia Nakashidze | ORCID 0009-0007-3365-7788 | nakashidze_ilo@bsu.edu.ge

Teona Gogitidze | ORCID 0000-0003-3451-5777 | teona.gogitidze@bauinternational.edu.ge

Ermira Jahja | ORCID 0000-0003-2941-5173 | ermira.hodo@wbu.edu.al

Aleena Parveen Shaikh | ORCID 0000-0002-1473-4334 | aleena.bsu@gmail.com

Nino Tebidze | ORCID 0000-0002-0769-7010 | ninoqedelidze@yahoo.com

Nameera Parveen Shaikh | ORCID 0000-0002-7393-0263 | nameera.ali7@gmail.com

Besik Kakabadze | ORCID 0009-0002-4557-4545 | Kakabadze567@gmail.com

Maia Resulidze | ORCID 0009-0003-8821-5566 | resulidze.maiko1@gmail.com

Rajneesh Khurana | ORCID 0000-0002-8856-4120 | rajneesh.khurana@gmail.com

Eteri Saralidze | ORCID 0000-0001-6841-1525 | saralidze.eteri@bsu.edu.ge

Otar Tsetskhladze | ORCID 0009-0006-7177-6297 | tsetskhladze.otari@bsu.edu.ge

Davit Baratashvili | ORCID 0000-0003-4912-4330 | baratashvili.daviti@bsu.edu.ge

Nino Kedelidze | ORCID 0000-0002-1414-9653 | ninoqedelidze@bsu.edu.ge

Tamar Peshkova | ORCID 0009-0009-4579-5170 | tamar.peshkova@bsu.edu.ge

Irina Nakashidze | ORCID 0000-0001-8934-6312 | irina.nakashidze@bsu.edu.ge

References

- Black, S., Kushner, I., & Samols, D. (2004). C-reactive protein. *Journal of Biological Chemistry*, 279(47), 48487–48490. <https://doi.org/10.1074/jbc.R400025200>
- Carubbi, F., Salvati, L., Alunno, A., Maggi, F., Borghi, E., Mariani, R., Mai, F., Paoloni, M., Ferri, C., Desideri, G., Cicogna, S., & Grassi, D. (2021). Ferritin is associated with the severity of lung involvement but not with worse prognosis in patients with COVID-19: Data from two Italian COVID-19 units. *Scientific Reports*, 11(1), 4863. <https://doi.org/10.1038/s41598-021-83831-8>
- Ceci, F. M., Fiore, M., Gavaruzzi, F., Angeloni, A., Lucarelli, M., Scagnolari, C., Bonci, E., Gabanella, F., Di Certo, M. G., Barbato, C., Petrella, C., Greco, A., De Vincentiis, M., Ralli, M., Passananti, C., Poscia, R., Minni, A., Ceccanti, M., Tarani, L., & Ferraguti, G. (2022). Early routine biomarkers of SARS-CoV-2 morbidity and mortality: Outcomes from an emergency section. *Diagnostics*, 12(1), 176. <https://doi.org/10.3390/diagnostics12010176>
- Chen, N., Zhou, M., Dong, X., Qu, J., Gong, F., Han, Y., Qiu, Y., Wang, J., Liu, Y., Wei, Y., Xia, J., Yu, T., Zhang, X., & Zhang, L. (2020). Epidemiological and clinical characteristics of 99 cases of 2019 novel coronavirus pneumonia in Wuhan, China: A descriptive study. *The Lancet*, 395(10223), 507–513. [https://doi.org/10.1016/S0140-6736\(20\)30211-7](https://doi.org/10.1016/S0140-6736(20)30211-7)
- Cheng, L., Li, H., Li, L., Liu, C., Yan, S., Chen, H., & Li, Y. (2020). Ferritin in the coronavirus disease 2019 (COVID-19): A systematic review and meta-analysis. *Journal of Clinical Laboratory Analysis*, 34(10), e23618. <https://doi.org/10.1002/jcla.23618>
- Colafrancesco, S., Alessandri, C., Conti, F., & Priori, R. (2020). COVID-19 gone bad: A new character in the spectrum of the hyperferritinemic syndrome? *Autoimmunity Reviews*, 19(7), 102573. <https://doi.org/10.1016/j.autrev.2020.102573>
- De Gonzalo-Calvo, D., Benítez, I. D., Pinilla, L., Carratalá, A., Moncusí-Moix, A., Gort-Paniello, C., Molinero, M., González, J., Torres, G., Bernal, M., Pico, S., Almansa, R., Jorge, N., Ortega, A., Bustamante-Munguira, E., Gómez, J. M., González-Rivera, M., Micheloud, D., Ryan, P., Martinez, A., Tamayo, L., Aldecoa, C., Ferrer, R., Ceccato, A., Fernandez-Barat, L., Motos, A., Riera, J., Menendez, R., Garcia-Gasulla, D., Penuelas, O., Torres, A., Bermejo-Martin, J.F., & Barbé, F. (2021). Circulating microRNA profiles predict the severity of COVID-19 in hospitalized patients. *Translational Research*, 236, 147–159. <https://doi.org/10.1016/j.trsl.2021.05.004>
- Ergun, S., Sankaranarayanan, R., & Petrović, N. (2023). Clinically informative microRNAs for SARS-CoV-2 infection. *Epigenomics*. <https://doi.org/10.2217/epi-2023-0179>
- Feld, J., Tremblay, D., Thibaud, S., Kessler, A., & Naymagon, L. (2020). Ferritin levels in patients

- with COVID-19: A poor predictor of mortality and hemophagocytic lymphohistiocytosis. *International Journal of Laboratory Hematology*, 42(6), 773–779. <https://doi.org/10.1111/ijlh.13309>
- Feng, Y., Liu, J., Kang, Y., He, Y., Liang, B., Yang, P., & Yu, Z. (2014). miR-19a acts as an oncogenic microRNA and is up-regulated in bladder cancer. *Journal of Experimental & Clinical Cancer Research*, 33(1), 67. <https://doi.org/10.1186/s13046-014-0067-8>
- Fox, S. E., Akmatbekov, A., Harbert, J. L., Li, G., Brown, J. Q., & Vander Heide, R. S. (2020). Pulmonary and cardiac pathology in African American patients with COVID-19: An autopsy series from New Orleans. *The Lancet Respiratory Medicine*, 8(7), 681–686. [https://doi.org/10.1016/S2213-2600\(20\)30243-5](https://doi.org/10.1016/S2213-2600(20)30243-5)
- Gao, Y., Li, T., Han, M., Li, X., Wu, D., Xu, Y., Zhu, Y., Liu, Y., Wang, X., & Wang, L. (2020). Diagnostic utility of clinical laboratory data determinations for patients with the severe COVID-19. *Journal of Medical Virology*, 92(7), 791–796. <https://doi.org/10.1002/jmv.25770>
- Ghafari-Fard, S., Khoshbakht, T., Hussien, B. M., Abdullah, S. T., Taheri, M., & Samadian, M. (2022). A review on the role of miR-16-5p in the carcinogenesis. *Cancer Cell International*, 22(1), 342. <https://doi.org/10.1186/s12935-022-02754-0>
- Gómez-Pastora, J., Weigand, M., Kim, J., Wu, X., Strayer, J., Palmer, A. F., Zborowski, M., Yazer, M., & Chalmers, J. J. (2020). Hyperferritinemia in critically ill COVID-19 patients—Is ferritin the product of inflammation or a pathogenic mediator? *Clinica Chimica Acta*, 509, 249–251. <https://doi.org/10.1016/j.cca.2020.06.033>
- Guo, W., Li, M., Dong, Y., Zhou, H., Zhang, Z., Tian, C., Qin, R., Wang, H., Shen, Y., Du, K., Zhao, L., Fan, H., Luo, S., & Hu, D. (2020). Diabetes is a risk factor for the progression and prognosis of COVID-19. *Diabetes/Metabolism Research and Reviews*, 36(7), e3319. <https://doi.org/10.1002/dmrr.3319>
- Hadi, J. M., Mohammad, H. M., Ahmed, A. Y., Tofiq, S. S., Abdalrahman, L. B., Qasm, A. A., & Ameer, A. M. (2022). Investigation of serum ferritin for the prediction of COVID-19 severity and mortality: A cross-sectional study. *Cureus*. <https://doi.org/10.7759/cureus.31982>
- Huang, I., Pranata, R., Lim, M. A., Oehadian, A., & Alisjahbana, B. (2020). C-reactive protein, procalcitonin, D-dimer, and ferritin in severe coronavirus disease-2019: A meta-analysis. *Therapeutic Advances in Respiratory Disease*, 14, 175346662093717. <https://doi.org/10.1177/1753466620937175>
- Kappert, K., Jahić, A., & Tauber, R. (2020). Assessment of serum ferritin as a biomarker in COVID-19: Bystander or participant? Insights by comparison with other infectious and non-infectious diseases. *Biomarkers*, 25(8), 616–625. <https://doi.org/10.1080/1354750X.2020.1797880>
- Linarez Ochoa, N. E., Rodríguez, G., Reyes, I. D., Rico Rivas, K. M., Ramírez, C., & Durón, R. M. (2022). Differences in inflammatory markers between coronavirus disease 2019 and sepsis in hospitalised patients. *Clinical Epidemiology and Global Health*, 15, 101059. <https://doi.org/10.1016/j.cegh.2022.101059>
- Liu, T., Zhang, J., Yang, Y., Ma, H., Li, Z., Zhang, J., Cheng, J., Zhang, X., Zhao, Y., Xia, Z., Zhang, L., Wu, G., & Yi, J. (2020). The role of interleukin-6 in monitoring severe cases of coronavirus disease 2019. *EMBO Molecular Medicine*, 12(7), e12421. <https://doi.org/10.15252/emmm.202012421>
- Luo, W. R., Yu, H., Gou, J. Z., Li, X. X., Sun, Y., Li, J. X., He, J. X., & Liu, L. (2020). Histopathologic

Findings in the Explant Lungs of a Patient With COVID-19 Treated With Bilateral Orthotopic Lung Transplant. *Transplantation*, 104(11), e329–e331. <https://doi.org/10.1097/TP.00000000000003412>

Maatman, T. K., Jalali, F., Feizpour, C., Douglas, A., McGuire, S. P., Kinnaman, G., Hartwell, J. L., Maatman, B. T., Kreutz, R. P., Kapoor, R., Rahman, O., Zyromski, N. J., & Meagher, A. D. (2020). Routine venous thromboembolism prophylaxis may be inadequate in the hypercoagulable state of severe coronavirus disease 2019. *Critical Care Medicine*, 48(9), e783–e790. <https://doi.org/10.1097/CCM.0000000000004466>

Mehta, P., McAuley, D. F., Brown, M., Sanchez, E., Tattersall, R. S., & Manson, J. J. (2020). COVID-19: Consider cytokine storm syndromes and immunosuppression. *The Lancet*, 395(10229), 1033–1034. [https://doi.org/10.1016/S0140-6736\(20\)30628-0](https://doi.org/10.1016/S0140-6736(20)30628-0)

Murvanidze, I., Tsetskhladze, O., Saralidze, E., Gogitidze, T., Khurana, R., Kedelidze, N., Peshkova, T., Nakashidze, I., & Nakashidze, I. (2023). The study of liver and kidney function within COVID-19 patients. *Georgian Medical News*, 337, 96–98.

Nauka, P. C., Baron, S. W., Assa, A., Mohrmann, L., Jindal, S., Oran, E., Glazman-Kuczaj, G., Southern, W. N., & Chekuri, S. (2021). Utility of D-dimer in predicting venous thromboembolism in non-mechanically ventilated COVID-19 survivors. *Thrombosis research*, 199, 82–84. <https://doi.org/10.1016/j.thromres.2020.12.023>

Para, O., Caruso, L., Pestelli, G., Tangianu, F., Carrara, D., Maddaluni, L., Tamburello, A., Castelnovo, L., Fedi, G., Guidi, S., Pestelli, C., Pennella, B., Ciarambino, T., Nozzoli, C., & Dentali, F. (2022). Ferritin as prognostic marker in COVID-19: The FerVid study. *Postgraduate Medicine*, 134(1), 58–63. <https://doi.org/10.1080/00325481.2021.1990091>

Poudel, A., Poudel, Y., Adhikari, A., Aryal, B. B., Dangol, D., Bajracharya, T., Maharjan, A., & Gautam, R. (2021). D-Dimer as a biomarker for assessment of COVID-19 prognosis: D-Dimer levels on admission and its role in predicting disease outcome in hospitalized patients with COVID-19. *PLOS ONE*, 16(8), e0256744. <https://doi.org/10.1371/journal.pone.0256744>

Ruddell, R. G., Hoang-Le, D., Barwood, J. M., Rutherford, P. S., Piva, T. J., Watters, D. J., Santambrogio, P., Arosio, P., & Ramm, G. A. (2009). Ferritin functions as a proinflammatory cytokine via iron-independent protein kinase C zeta/nuclear factor kappaB-regulated signaling in rat hepatic stellate cells. *Hepatology*, 49(3), 887–900. <https://doi.org/10.1002/hep.22716>

Sakka, M., Connors, J. M., Hékimian, G., Martin-Toutain, I., Crichi, B., Colmegna, I., Bonnefont-Rousselot, D., Farge, D., & Frere, C. (2020). Association between D-Dimer levels and mortality in patients with coronavirus disease 2019 (COVID-19): A systematic review and pooled analysis. *JMV- Journal de Médecine Vasculaire*, 45(5), 268–274. <https://doi.org/10.1016/j.jdmv.2020.05.003>

Santos-Poleo, Y. D., Perez-Sanchez, L., Ocanto, A., Oquillas-Izquierdo, D., & Rodriguez-Recio, F. (2020). Elevated D-dimer and acute pulmonary thromboembolism in patients with COVID-19. *Journal of Negative and No Positive Results*, 5(12), 1516–1527. <https://doi.org/10.19230/jonnpr.3960>




Shakaroun, D. A., Lazar, M. H., Horowitz, J. C., & Jennings, J. H. (2023). Serum ferritin as a predictor of outcomes in hospitalized patients with COVID-19 pneumonia. *Journal of Intensive Care Medicine*, 38(1), 21–26. <https://doi.org/10.1177/08850666221113252>

Sproston, N. R., & Ashworth, J. J. (2018). Role of C-reactive protein at sites of inflammation and infection. *Frontiers in Immunology*, 9, 754. <https://doi.org/10.3389/fimmu.2018.00754>

- Tang, N., Li, D., Wang, X., & Sun, Z. (2020). Abnormal coagulation parameters are associated with poor prognosis in patients with novel coronavirus pneumonia. *Journal of Thrombosis and Haemostasis*, 18(4), 844–847. <https://doi.org/10.1111/jth.14768>
- Vargas-Vargas, M., & Cortés-Rojo, C. (2020). Ferritin levels and COVID-19. *Revista Panamericana de Salud Pública*, 44, e72. <https://doi.org/10.26633/RPSP.2020.72>
- Wang, D., Hu, B., Hu, C., Zhu, F., Liu, X., Zhang, J., Wang, B., Xiang, H., Cheng, Z., Xiong, Y., Zhao, Y., Li, Y., Wang, X., & Peng, Z. (2020). Clinical characteristics of 138 hospitalized patients with 2019 novel coronavirus–infected pneumonia in Wuhan, China. *JAMA*, 323(11), 1061–1069. <https://doi.org/10.1001/jama.2020.1585>
- Wu, J., Liu, J., Zhao, X., Liu, C., Wang, W., Wang, D., Xu, W., Zhang, C., Yu, J., Jiang, B., Cao, H., & Li, L. (2020). Clinical characteristics of imported cases of coronavirus disease 2019 (COVID-19) in Jiangsu Province: A multicenter descriptive study. *Clinical Infectious Diseases*, 71(15), 706–712. <https://doi.org/10.1093/cid/ciaa199>
- Zhou, F., Yu, T., Du, R., Fan, G., Liu, Y., Liu, Z., Xiang, J., Wang, Y., Song, B., Gu, X., Guan, L., Wei, Y., Li, H., Wu, X., Xu, J., Tu, S., Zhang, Y., Chen, H., & Cao, B. (2020). Clinical course and risk factors for mortality of adult inpatients with COVID-19 in Wuhan, China: A retrospective cohort study. *The Lancet*, 395(10229), 1054–1062. [https://doi.org/10.1016/S0140-6736\(20\)30566-3](https://doi.org/10.1016/S0140-6736(20)30566-3)

RESEARCH ARTICLE

Nanosomes carrying mycosynthesized silver nanoparticles as a drug delivery tool against MDR *Salmonella typhi* BT CB170

Mehwish Iqtedar ^{1,*}  | Nimra illyas ¹ | Mehral Aslam ^{1,2,*}  | Roheena Abdullah ¹ 
Afshan Kaleem ¹ 

¹ Department of Biotechnology, Lahore College for Women University, Lahore, Pakistan
ROR ID: 02bf6br77

² Department of Nutrition and Health Promotion, University of Home Economics, Lahore, Pakistan
ROR ID: 01jdwf714

* Corresponding authors: E-mail: miqtedar@gmail.com (M.I.), mehral.92@gmail.com (M.A.); Ph.: +92 306 5630693

Citation: Iqtedar M., Illyas N., Aslam M., Abdullah R., & Kaleem A. (2025). Nanosomes carrying mycosynthesized silver nanoparticles as a drug delivery tool against MDR *Salmonella typhi* BT CB170. *The European chemistry and biotechnology journal*, 4, 40-52.
<https://doi.org/10.62063/ecb-61>

License: This article is licensed under a Creative Commons Attribution-NonCommercial 4.0 International License (CC BY-NC 4.0).

Peer review: Double Blind Refereeing.

Ethics statement: It is declared that scientific and ethical principles were followed during the preparation of this study and all studies utilized were indicated in the bibliography (Ethical reporting: editor@euchembioj.com).

Plagiarism Check: Done (iThenticate). Article has been screened for originality.

Received: 27.05.2025

Accepted: 28.06.2025

Online first: 01.07.2025

Published: 11.07.2025

Abstract

New regimes of treatments and delivery systems are of great need today because of the increasing emergence of antimicrobial resistance among pathogens. In this study, initially liposomes were prepared comprising mycosynthesized silver nanoparticles in combination with meropenem. As a result of this combination, nanosomes were designed. *In vitro analysis* of the prepared formulation was done to check its effectiveness against MDR *Salmonella typhi*. Extracellular synthesis of (AgNPs) silver-nanoparticles through *Aspergillus fumigatus* BT CB01 was conducted. The particles were then characterized through by a zeta sizer, and they had particle size (299.6 nm), zeta potential (-2.64 mV) with a polydispersity value (0.4). Different liposomal formulations were prepared and characterized, each with different in size i.e. control liposomes had 318.7 nm, drug-encapsulated liposomes had 237.4 nm, silver-nanoparticles incorporated liposomes had 320.3 nm and Silver-nanoparticles incorporated drug liposomes had 215.3 nm size with different zeta potential and polydispersity index for each, i.e. -45.8 (PDI:0.3), -41.3 (PDI:0.3), -42.5 (PDI:0.4) and -39.6 mV (PDI:0.3), respectively, signifying a good stable and homogeneous solution. Meropenem encapsulated liposomes had (94%) encapsulation efficiency, whereas Silver-nanoparticles incorporated drug liposomes had (86%) encapsulation efficiency. The release study of drugs through dialysis membranes graded in order of drug encapsulated liposomes > Silver-nanoparticles incorporated drug liposomes > control liposomes. *In vitro analysis* revealed that the antibacterial assay through the disk diffusion method revealed that drug-encapsulated liposomes showed a 1-fold increase in activity as compared to



those which were incorporated with the silver nanoparticles. Conclusively, the addition of silver nanoparticles did not affect the stability of liposomes; however, they affected the encapsulation efficiency and drug release property of the delivery system.

Keywords: Antibacterial activity, (AgNPs) silver-nanoparticles, liposomes, *Salmonella typhi*.

Introduction

Constant deployment of antimicrobial medications in treating diseases has prompted the emergence of resistance among different pathogens (S. Singh et al., 2010). Nanodrugs where nanoparticles, have promising applications in drug delivery systems and diagnostics for the treatment of different diseases (Marcato & Durán, 2008; R. Singh & Nalwa, 2011). Liposomes are appropriate as vehicles for transporting antimicrobials since they generally provide a safe release of drug, reduced toxicity and protection of the encapsulated drug from becoming ineffective (Omri et al., 2002).

Upon direct fusion, the encapsulated or entrapped antimicrobial drug inside the liposomes can be discharged to the bacterial cell membrane or inside the microorganism. The exceptional structure of liposomes, a lipid layer encompassing an aqueous cavity, empowers them to convey both hydrophobic and hydrophilic drugs, while inhibiting any chemical modification (Zhang et al., 2010). Hydrophilic drugs are entrapped inside the aqueous core while hydrophobic drugs are incorporated in the lipid bilayers of the liposomes (Ding et al., 2006). Various clinical formulations of liposomes for treating various diseases have been made (Immordino et al., 2006). The effect of certain antimicrobials against different infectious microbes is increased by entrapping inside the liposomes (Fenske et al., 2008). New approaches for novel therapeutic applications are strengthened by consolidating the properties of liposomal nanocarriers and nanoparticles. The impact of nanoparticles incorporation on the lipid bilayers of liposome was also observed (Rivera Gil et al., 2010). Nanoparticles are incorporated inside the liposomal vesicles for a number of applications, providing extraordinary advances in drug delivery systems (Al-jamal & Kostarelos, 2007).

Silver nanoparticle's efficacy against many bacteria was explored by several researchers and their successful potential in opposition to a wide variety of microorganisms was demonstrated. At the start of the twentieth century, Mukherjee and co-workers reported the first production of silver nanoparticles by means of a fungus-assisted method (Mukherjee et al., 2001). For the synthesis of silver nanoparticles of the diameter ranging from 25 ± 12 nm, the fungus *Verticillium* was utilized. Hussein with his co-worker in 2015 synthesized Ag nanoparticles from *Fusarium oxysporum* and evaluated their antimicrobial activity against pathogenic bacteria through *Staphylococcus aureus*, and *Escherichia coli* (Hussein et al., 2015).

In one of the previous study the combined effectiveness of biologically synthesized silver nanoparticles and antibiotics of different types against bacteria that were multidrug resistant was also reported (Naqvi et al., 2013). Schumacher and Margalit (1997), employed lipid thin film hydration method for the preparation of liposome encapsulated ampicillin demonstrated polymyxin B encapsulated liposomes as another effective example of antibacterial liposomal drug delivery systems.

Hădărugă et al. (2011) synthesized stable liposomes containing cobalt ferrite nanoparticles using an ultrasonication method. The development of nanoliposomes containing silver nanoparticles as a potential antimicrobial tool against microbial resistance was reported by Eid and Azzazy (2014). Dextrose-capped spherical silver nanoparticles were prepared and incorporated into nanoliposomes,

resulting in the silver nanoparticles incorporating nanoliposomes of a size ranging from 25-80 nm by using reverse phase evaporation method. Nanoparticle/liposome interactions are thus playing a vital role in the research development of nanomedicine. Liposomes serve as model systems by consolidating the properties of silver nanoparticles and lipid vesicles, resulting in novel nanomedical applications. Nanoparticles are thus used while preparing liposomes in order to control the membrane properties of vesicles. For the photo-induced release of drugs, fluorescent silver nanoparticles were embedded in the bilayers of liposomes by Li et al. (2014). Thus, in the current study, mycosynthesized silver nanoparticles will be incorporated in liposomes to find their effectiveness in the drug delivery system.

Materials and methods

Mycosynthesis of silver nanoparticles

For microbial synthesis of extracellular silver nanoparticles, the fungal strain *Aspergillus fumigatus* BTCB01 was obtained from the Culture Bank BTCB of Lahore College for Women University, Department of Biotechnology (Shahzad et al., 2019).

Biomass preparation

Biomass for this purpose was prepared in the minimal media with neutral pH comprising glucose (0.75%), $\text{MgSO}_4 \cdot 7\text{H}_2\text{O}$ (0.30 mM), KH_2PO_4 (38.6 mM), K_2HPO_4 (8.63 mM), $(\text{NH}_4)_2\text{SO}_4$ (5.68 mM), and yeast extract (0.045%). Media was inoculated with a loop full of spores and incubated at 25°C with a continuous shaking at 120 rpm for 72 hours (Madakka et al., 2018). Biomass was filtered using Whatman filter paper (grade A) no. 1 (Ahlstrom, Spain) and was resuspended in double distilled water (150 mL) in a 250 ml Erlenmeyer flask after rinsing it three times, and later it was incubated at 25°C with continuous shaking (120 rpm) for 72 hours.

Addition of salt in nanoparticle synthesis

After 72 hours of shaking, the biomass was again filtered using filter paper and the remaining cell-free extract was obtained. Silver nitrate (1 mM) was added to 100 mL of distilled water in 1:1 ratio. The flasks were incubated at 25°C at 120 rpm until the color change occurred, indicating the formation of silver nanoparticles (Sadowski et al., 2008).

Preparation of liposomes incorporating silver nanoparticles and drug encapsulation

Liposomes were prepared using the thin film hydration method as described previously (Fritze et al., 2006). For this purpose, 20 mg of PC (phosphatidylcholine) and 13.1 mg of CH (cholesterol) (3:1) were dissolved in the organic solvent methanol:chloroform (10 ml) (2:1, v/v) in a round bottom flask. Further, the evaporation of organic solvent was carried out using a rotary evaporator under high vacuum in a 40°C water bath and rotated at 180 rpm until the thin dry film of lipid was deposited on the wall of the flask. The swelling solution comprising 5 ml of (PBS) phosphate buffer saline (pH 7.6) was added to a previously prepared thin dry film and the flask containing the mixture solution was then again rotated for 30 minutes. Formed liposomes were (MLVs) multi-lamellar vesicles. For downsizing, MLVs were subjected to sonication for 30 minutes by placing them in a bath sonicator to obtain the (SUVs) small unilamellar vesicles. For meropenem, the chemical structure shown in Fig.1) encapsulated liposomes, the thin and dry lipid film was hydrated by adding 5 ml of antibiotic solution (32 mg of meropenem dissolved in 0.9% NaCl solution) as reported by (Gubernator et al., 2007). Then, after the incorporation of the drug in the liposomal solution Silver-nanoparticles (AgNPs) were added (5 ml) and hydrated by PBS in the mixture, according to Bernardi et al. (2012).

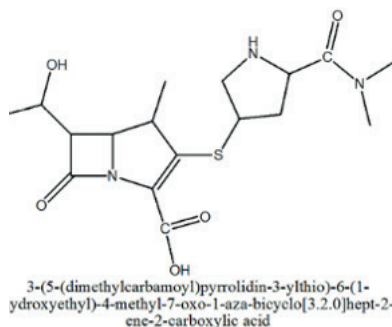


| **Figure 1.** Chemical structure of Meropenem (Waheed et al., 2016).

Characterization of liposomes

Each liposomal formulation was characterized by measuring the mean particle size diameter, its zeta potential and polydispersity index immediately after the formation of the liposomal formulation at 25°C using the zeta sizer Nano ZS (Karn et al., 2013).

Drug quantification by HPLC

To quantify meropenem in the liposomes, reverse-phase HPLC was performed (Yng, 2005). An octadecylsilane (10 µm) column with ambient temperature was used for this purpose. The mobile phase comprises of 70% acetonitrile and 30% (KH₂PO₄) di-hydrogen potassium phosphate buffer (0.03M, pH 3). The liposomal samples (50 µl) were dissolved in organic solvent methanol (950 µl), with a flow rate of 1 ml/min in the column. The calibration of HPLC was done with the standard solutions with concentrations ranging from 40 to 160 µg/ml at 235 nm.

Encapsulation efficiency of liposomes

Encapsulation efficiency of liposomal formulations was calculated as reported in a previously published paper (Schumacher & Margalit, 1997; Yng, 2005). HPLC was used to assay the amount of meropenem in the pre-centrifuged sample, the resuspended pellet and the collected supernatant.

In vitro drug release study

Adialysis method was used for the *in vitro* meropenem release study of liposome dispersion as reported by Panwar et al. (2010). Dialysis bags (12,000-14,000 MW cut off; Sigma-Aldrich) were soaked prior to use in distilled water at room temperature for 12 h for the sake of removal of the preservative. Each dialysis bag contained 5 ml of free meropenem as control, 5 ml of drug-encapsulated liposome and 5 ml of nanoparticle incorporated drug liposome, respectively. For the drug release, each dialysis bag was separately immersed in a conical flask containing 100 ml of (PBS) phosphate buffer saline (pH 7.4) and stirred through magnetic stirrer at 100 rpm at 37 °C. Throughout the experiment, 1 ml of the aliquot at different time intervals was removed from the receptor chamber and replaced with an equivalent volume of fresh PBS. The release run continued for 24 hrs and after 1/2 hr, 1 hr, 3 hr, 5 hr, 8 hr, 24 hr the aliquots were taken and analyzed through HPLC.

In vitro antimicrobial assay against MDR *Salmonella typhi* BTCB170

The antibacterial activity was checked through the disk diffusion method (Choi et al., 2011). The multi-drug-resistant pathogen *Salmonella typhi* BTCB170 was used. For this purpose, *S. typhi* inoculum was prepared according to 0.5 McFarland standard. Nutrient agar plates were prepared

and inoculated with the *S. typhi* inoculum by swabbing vertically and horizontally. Each disk was loaded with 20 μ l of the prepared formulations and placed on the agar plates and incubated at 37°C for 24 hrs overnight. Inhibition zones were measured after 24 hours of incubation in millimeters.

Statistical Analysis

One-way ANOVA was used to find the significance ($p \leq 0.05$) between means of different treatments. SPSS program version 16 was used for the analysis. Each experiment was repeated thrice.

Results and discussion

Mycosynthesis of silver nanoparticles

A colony of fungal strain *Aspergillus fumigatus* BTCB 01 on potato dextrose agar was obtained, which is shown in Figure 2.

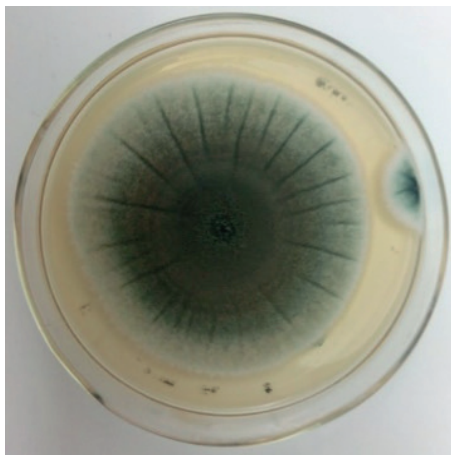


Figure 2. Appearance of *Aspergillus Fumigatus* BTCB01; colony on potato dextrose agar medium after 7 days of incubation at 30°C.

The initial indication of the prepared silver nanoparticles was the change in color of the reaction mixture as shown in Figure 3. Further confirmation of AgNP's presence was confirmed by the appearance of excitation peaks in the range of 300-376 nm in the UV-visible spectrum (data not shown).

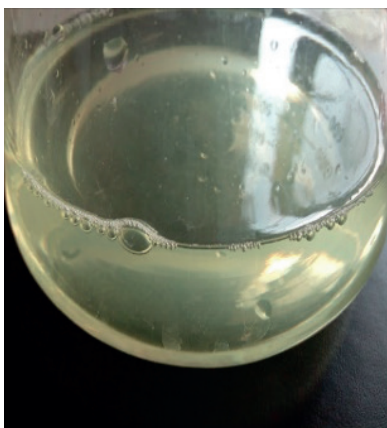


Figure 3. Mycosynthesized AgNPs after mixing cell filtrate (72 h) of *Aspergillus fumigatus* BTCB01 with silver nitrate (1 mM).

In the present study, the extracellular biosynthesis of fungal nanoparticles was carried out using the strain, *Aspergillus fumigatus* BTCB01. The fungal silver nanoparticles showed a polydispersity value of 0.4 due to no particle aggregations (Table 1). It is well known that nanoparticles having a PDI of less than 0.7 are stable, and no aggregation occurs, while the greater the zeta potential, the more stable the particles are. Many studies have shown the successful synthesis of silver nanoparticles of varying size and characteristics from different fungal species such as *Trichoderma harzianum* (Bawaskar et al., 2010; Shelar & Chavan, 2015), *Aspergillus flavus* (Jain et al., 2011) and *Metarhizium anisopliae* (Amerasan et al., 2015).

Synthesis and characterization of liposomes

Table 1 summarizes the z-average diameters in nm, zeta potential values and polydispersity index of all the liposomal formulations i.e. A (liposomes), B (drug-encapsulated liposomes), C (silver nanoparticles incorporating liposomes) and D (silver nanoparticles incorporating drug liposomes). Control (Formulation A) comprising of only liposomes had the z-average diameter of 318.7 nm, zeta potential of -45.8 mV and polydispersity of 0.3, indicating stable particles. Whereas, Formulation B, comprising drug-encapsulated liposomes, showed a z-average diameter of 237.4 nm with a zeta potential of -41.3 mV and polydispersity index value of 0.3, indicating the homogeneous stable liposomes. Formulation C (silver nanoparticle incorporated liposomes) exhibited greater particle stability with a z-average diameter of 320.3 nm and a zeta potential value of -42.5 mV, showing polydispersity of 0.4. Similarly, the formulation D (silver nanoparticles incorporating drug liposomes) had a z-average diameter of 215.3 nm and a zeta potential value of -39.6 mV with 0.3 polydispersity index, indicating no aggregations of liposomes. For the characterization of the present liposomal formulations, the mean particle diameters, zeta potential values and polydispersity index were determined by using zeta sizer Nano ZS. The samples were diluted in water and all the measurements were made at 25°C. This was in close agreement with (Hue et al., 2015) who characterized the liposomes size as 167.8 ± 3.6 nm while having negative zeta potential value of -27.5 ± 3.5 mV. A very similar study conducted previously also revealed the mean diameter of 278.46 nm and zeta potential of -18.3 mV of the silver-nanoparticle incorporated liposomes. Those results confirmed that obtained silver-nanoparticle incorporated liposomes had a mean diameter between 321 and 373 nm, with polydispersity index close to 0.2 and a negative zeta potential around -40 mV, indicating greater stability to the AgNPs (Espinoza et al., 2020).

Table 1. Zeta analysis of different liposomal formulations.

Experimental Groups	Liposomal Formulations	z-average diameter (nm)	Zeta Potential (mV)	Polydispersity Index
Group A	Liposomes	318.7	-45.8	0.3
Group B	Drug encapsulated liposomes	237.4	-41.3	0.3

Group C	Silver nanoparticle incorporated liposomes	320.3	-42.5	0.4
Group D	Silver nanoparticle incorporated drug liposomes	215.3	-39.6	0.3

Similarly, in another study using *Aspergillus fumigatus* and under optimized parameters, extracellular synthesis of AgNPs (yellow colored) was achieved within 20 seconds having 0.681 nm size at 400 nm with negative zeta potential of -23.4 mV, whereas in another previous study, extracellular brown-colored spherical AgNPs was also reported from *Aspergillus flavus*, synthesized within 72 hrs having an average size of 8.92 nm at 420 nm.

Drug quantification

In the present study, a reverse phase HPLC assay was performed for the quantification of meropenem in the liposomal formulations. By plotting the calibration plot of peak area versus meropenem standard concentration, all the four standard solutions of meropenem at the concentration of 40, 80, 120 and 160 µg/ml showed a good linear standard concentration curve having $r^2 = 0.99$. Both the pure meropenem standard solutions and the liposomal samples of drug-encapsulated liposomes and silver nanoparticles incorporated liposomes before and after centrifugation showed a retention time of 3.3 minutes (Figure 4).

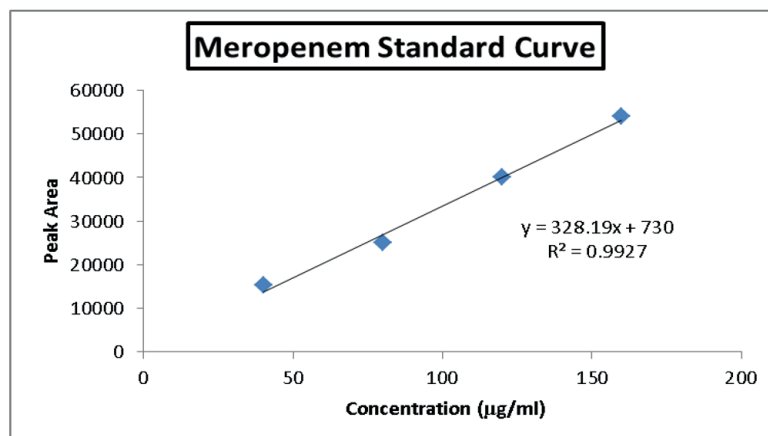


| **Figure 4.** Standard curve for meropenem shows the retention time of 3.3 minutes.

Encapsulation efficiency of liposomes

The preparation of various liposomal formulations involving meropenem encapsulation as well as AgNPs incorporation in the liposomes using the thin film hydration method resulted in the development of stable liposomal formulations. Overall, the encapsulation efficiency of drug-encapsulated liposomes was greater than AgNPs incorporated drug liposomes. It was observed that drug encapsulated liposomes depicted 94% encapsulation efficiency (direct method) whereas

86% from AgNPs incorporated drug liposomes (Table 2). In one of the previously conducted studies, the encapsulation efficiency of silver nanoparticle incorporated liposomes was between 51.81 to 58.83%, which was less than drug-encapsulated liposomes (Espinoza et al., 2020). Whereas, 95% (indirect method) encapsulation efficiency was observed in drug encapsulated liposomes and 89% for encapsulation efficiency of AgNPs incorporated drug liposomes (Table 2). Thus, meropenem was found to be encapsulated more effectively in the drug-encapsulated liposomes as compared to AgNPs incorporated drug liposomes. AgNPs have strong interactions with the inner hydrophobic region of the liposomes. Changes in encapsulation efficiency might be due to the interaction of AgNPs with the hydrophobic part of liposomes, affecting the liposomal membrane fluidity, thereby effecting the drug release (Bothun, 2008).

Table 2. The percentage encapsulation efficiencies of liposomal formulations prepared.

Experimental groups	Pre-centrifugation Sample (µg)	After centrifugation Pellet sample (ug)	Supernatant sample (ug)	EE (Indirect Method) (%)	EE (Direct Method) (%)	Diameter of zone (mm)±SEM*
Drug Encapsulated Liposomes	25601	24111	1190	94	95	8.6±0.01 ^e
Silver nanoparticles drug liposomes	22321	22321	19321	86	89	8.4±0.01 ^d

In vitro drug release study

In vitro drug release study of both the drug and silver nanoparticle-incorporated liposomes showed sustained release of meropenem. The drug release rate from the liposomes increased gradually over 24 h and can be ranked in the order of drug-encapsulated liposomes > Silver nanoparticles incorporated drug liposomes > AgNPs (Figure 5). However, in a similar study, it was observed that the drug release from gold NPs encapsulated liposomes showed increased drug release and that is due to change in membrane fluidity because of the presence of metal nanoparticles (Patra et al., 2018).

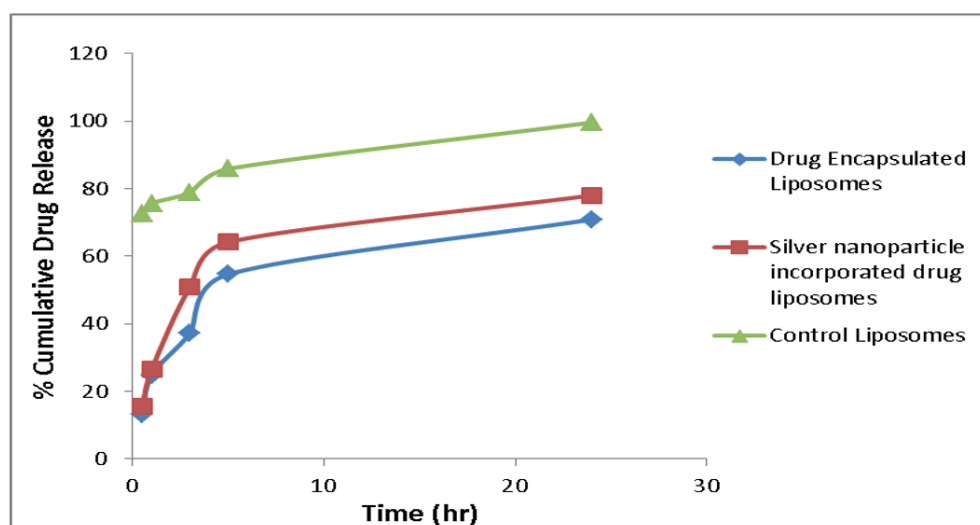
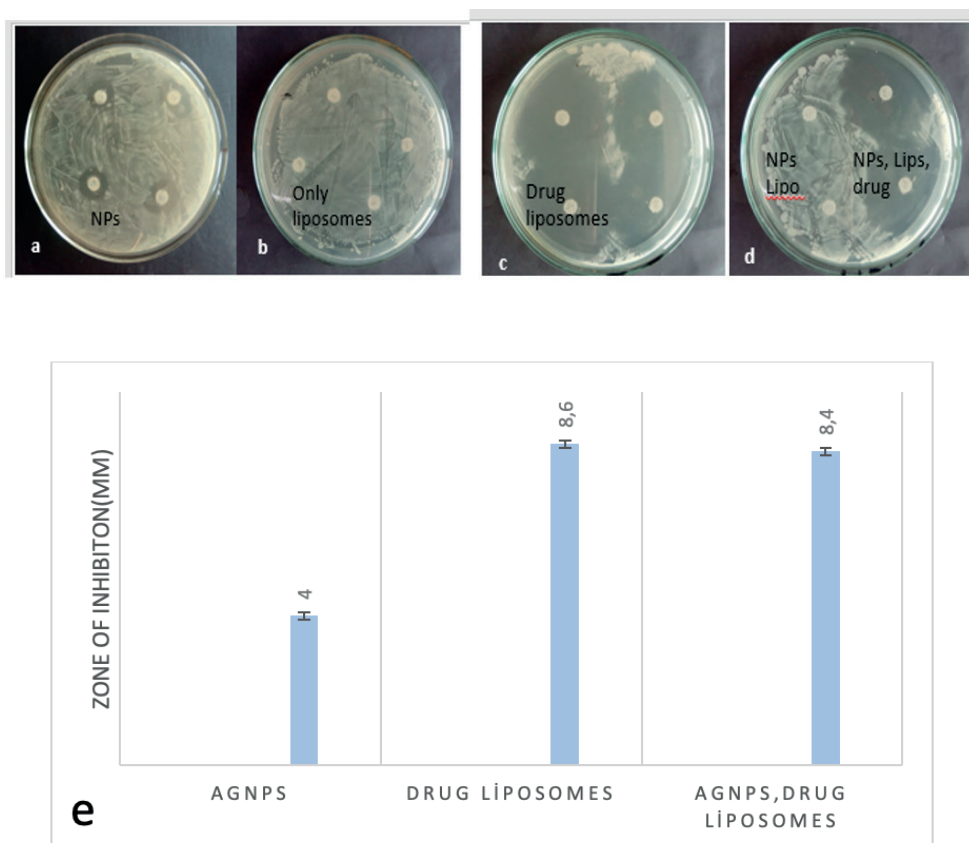


Figure 5. *In vitro* drug release profile of all liposomal formulations.

In vitro antimicrobial activity

An *In vitro* study was done for the prepared liposomal formulations against the pathogenic bacteria *Salmonella typhi* BTCB170. Clear zones of inhibition around the loaded discs on the plates indicate the effectiveness of the formulation in inhibiting the growth of pathogens. In this respect, no zones of inhibition were observed by the plate-carrying disks loaded with control liposome and nanoparticle-incorporated liposomes. Whereas clear zones of inhibition were observed around the discs-loaded with silver nanoparticles (4 mm), drug-loaded liposomes (8.6 mm) and drug and NPs-loaded liposomes (8.4 mm) (Figure 6a-e). The antimicrobial activity decreases to 1fold with AgNPs and drug-encapsulated liposomes. Table 2 summarizes the diameter of zone of inhibition of drug in liposomal formulations. It was observed that formulations carrying AgNPs incorporating drug liposomes somehow reduced the antimicrobial activity by showing less zone of inhibition as compared to control samples. Reduction in inhibition zone might be related to the effect of AgNPs on the size and stability of the liposomes.



| **Figure 6.** Antimicrobial activity results.

A report similar to the current study showed that the addition of metal NPs reduces the size of liposomes, therefore reducing the drug encapsulation efficiency and drug release effect (Torres et al., 2012). Similar observations were demonstrated by (Schumacher & Margalit, 1997), who performed antibacterial assay involving the samples of control liposomes, ampicillin encapsulated liposomes as well as free drug solutions by using paper disks against the test bacterium, *Micrococcus luteus* where liposomal formulations had lower MIC as compared to free drug. Drulis-Kawa et al., (2006) observed *in vitro* antibacterial efficacy of

meropenem and gentamicin encapsulated liposomes against Gram negative and Gram positive strains of bacteria and the strategy was found effective. However, in contrast to the current study, the incorporation of silver nanoparticles in nano liposomes was also studied by Hussein and co-workers and observed increased antibacterial activity against *Escherichia coli* and *Staphylococcus aureus* (Hussein et al., 2015). In one of the study, the presence of silver nanoparticles stabilized the nanoliposomes by narrowing their size and reducing the size of the zone and similar were the findings of the current study. However, the incorporation of silver nanoparticles did not alter the zeta potential values of liposomes.

Conclusions

Conclusively, in the present study, silver nanoparticles were synthesized from *Aspergillus niger* BTCB01. In order to enhance the efficiency of the drug delivery system, AgNPs were added to drug liposomes. But the addition of AgNPs altered the stability of liposomes and encapsulation efficiency of the drug, which overall affected the antimicrobial activity. The system can be made efficient by optimizing different parameters, and it can be further studied in vivo to obtain the efficiency of the drug delivery system in animal models.

Acknowledgment

Authors acknowledge the support provided by Lahore University of Management Sciences LUMS and Government College University, Lahore, Chemistry Department for providing access to high tech equipment.

Funding

Not applicable.

Conflict of interest

Authors declare no conflict of interest.

Data availability statement

All data are available here.

Ethics committee approval

Ethics committee approval is not required for this study.

Authors' contribution statement

The authors acknowledge their contributions to this paper as follows: **Study conception and design:** (MI); **Data collection:** (NI); **Analysis and interpretation of results:** (NI and MA); **Manuscript draft preparation:** (MA, RA and AK). All authors reviewed the results and approved the final version of the manuscript.

Use of Artificial Intelligence: No artificial intelligence-based tools or applications were used in the preparation of this study. The entire content of the study was produced by the author(s) in accordance with scientific research methods and academic ethical principles.

ORCIDs and emails of the authors

Mehwish Iqtedar | ORCID 0000-0002-2350-3431 | miqtedar@gmail.com

Nimra Ilyas | ilyasnimra0@gmail.com

Mehral Aslam | ORCID 0009-0000-4298-3998 | mehral.92@gmail.com

Roheena Abdullah | ORCID 0000-0003-3932-6297 | roheena_abdullah@yahoo.com

Afshan Kaleem | ORCID 0000-0002-3972-0051 | afshankaleem@yahoo.dk

References

- Al-jamal, W. T., & Kostarelos, K. (2007). Liposome–nanoparticle hybrids for multimodal diagnostic and therapeutic applications. *Nanomedicine*, 2(1), 85–98. <https://doi.org/10.2217/17435889.2.1.85>
- Amerasan, D., Nataraj, T., Murugan, K., Panneerselvam, C., Madhiyazhagan, P., Nicoletti, M., & Benelli, G. (2015). Myco-synthesis of silver nanoparticles using *Metarhizium anisopliae* against the rural malaria vector *Anopheles culicifacies* Giles (Diptera: Culicidae). *Journal of Pest Science*, 89(1), 249–256. <https://doi.org/10.1007/s10340-015-0675-x>
- Bawaskar, M., Gaikwad, S., Ingle, A., Rathod, D., Gade, A., Duran, N., Marcato, P. D., & Rai, M. (2010). A new report on mycosynthesis of silver nanoparticles by *Fusarium culmorum*. *Current Nanoscience*, 6(4), 376–380. <https://doi.org/10.2174/157341310791658919>
- Bernardi, D. S., Guidelli, E. J., Da Cruz, E. L. C. M., & Lopez, R. F. V. (2012). Preparation and characterization of liposome containing ovalbumin and silver nanoparticles. *Revista Eletrônica de Farmácia*, 9, Article 01.
- Bothun, G. D. (2008). Hydrophobic silver nanoparticles trapped in lipid bilayers: size distribution, bilayer phase behavior, and optical properties. *Journal of Nanobiotechnology*, 6, 13. <https://doi.org/10.1186/1477-3155-6-13>
- Choi, J. G., Kang, O. H., Lee, Y. S., Chae, H. S., Oh, Y. C., Brice, O. O., Kim, M. S., Sohn, D. H., Kim, H. S., & Park, H. (2011). In vitro and in vivo antibacterial activity of *Punica granatum* peel ethanol extract against *Salmonella*. *Evidence-Based Complementary and Alternative Medicine*, Article ID 717763. <https://doi.org/10.1093/ecam/nep105>
- Ding, B. S., Dziubla, T., Shuvaev, V. V., Muro, S., & Muzykantov, V. R. (2006). Advanced drug delivery systems that target the vascular endothelium. *Molecular Interventions*, 6(2), 98–112. <https://doi.org/10.1124/mi.6.2.7>
- Drulis-Kawa, Z., Gubernator, J., Dorotkiewicz-Jach, A., Doroszkiewicz, W., & Kozubek, A. (2006). A comparison of the *in vitro* antimicrobial activity of liposomes containing meropenem and gentamicin. *Cellular & Molecular Biology Letters*, 11(3), 360–375. <https://doi.org/10.2478/s11658-006-0030-6>
- Eid, K. A. M., & Azzazy, H. M. E. (2014). Sustained broad-spectrum antibacterial effects of nanoliposomes loaded with silver nanoparticles. *Nanomedicine*, 9(9), 1301–1310. <https://doi.org/10.2217/nnm.13.89>
- Espinoza, J. T., Novak, R. S., Magalhães, C. G., Budel, J. M., Justus, B., Gonçalves, M. M., Boscardin, P. M. D., Farago, P. V., & Paula, J. d. F. P. D. (2020). Preparation and characterization of liposomes loaded with silver nanoparticles obtained by green synthesis. *Brazilian Journal of Pharmaceutical Sciences*, 56, e18601. <https://doi.org/10.1590/s2175-97902020000118601>
- Fenske, D. B., Chonn, A., & Cullis, P. R. (2008). Liposomal nanomedicines: an emerging field. *Toxicologic Pathology*, 36(1), 21–29. <https://doi.org/10.1177/0192623307310960>

- Fritze, A., Hens, F., Kimpfler, A., Schubert, R., & Peschka-Süss, R. (2006). Remote loading of doxorubicin into liposomes driven by a transmembrane phosphate gradient. *Biochimica et Biophysica Acta – Biomembranes*, 1758(11), 1633–1640. <https://doi.org/10.1016/j.bbmem.2006.08.012>
- Gubernator, J., Drulis-Kawa, Z., Dorotkiewicz-Jach, A., Doroszkiewicz, W., & Kozubek, A. (2007). *In vitro* antimicrobial activity of liposomes containing ciprofloxacin, meropenem and gentamicin against Gram-negative clinical bacterial strains. *Letters in Drug Design & Discovery*, 4(4), 297–304. <https://doi.org/10.2174/157018007784620040>
- Hădărugă, N. G., Hădărugă, D. I., Vlăzan, P., & Barbu-Tudoran, L. (2011). New liposomes containing cobalt ferrite nanoparticles: synthesis and characterization. *Journal of Agroalimentary Processes and Technologies*, 17(1), 1–6.
- Hue, P., Linh, L., Lam, N., Hai, N., Son, H., Toan, N., & Tung, B. (2015). Developing and evaluating *in vitro* effect of pegylated liposomal doxorubicin on human cancer cells. *Journal of Chemical and Pharmaceutical Research*, 7, 2239–2243.
- Husseiny, S. M., Salah, T. A., & Anter, H. A. (2015). Biosynthesis of size-controlled silver nanoparticles by *Fusarium oxysporum*: their antibacterial and antitumor activities. *Beni-Suef University Journal of Basic and Applied Sciences*, 4(2), 225–231. <https://doi.org/10.1016/j.bjbas.2015.07.004>
- Immordino, M. L., Dosio, F., & Cattel, L. (2006). Stealth liposomes: review of the basic science, rationale, and clinical applications, existing and potential. *International Journal of Nanomedicine*, 1, 297–315.
- Jain, N., Bhargava, A., Majumdar, S., Tarafdar, J., & Panwar, J. (2011). Extracellular biosynthesis and characterization of silver nanoparticles using *Aspergillus flavus* NJP08: a mechanistic perspective. *Nanoscale*, 3(2), 635–641. <https://doi.org/10.1039/C0NR00656D>
- Karn, P. R., Cho, W., Park, H. J., Park, J. S., & Hwang, S. J. (2013). Characterization and stability studies of a novel liposomal cyclosporin A prepared using the supercritical fluid method: comparison with the modified conventional Bangham method. *International Journal of Nanomedicine*, 8, 365–377. <https://doi.org/10.2147/IJN.S39025>
- Li, J., An, X., & Pan, Z. (2014). Photoinduced drug release from complexes of liposome and fluorescent silver nanoparticles. *RSC Advances*, 4(18), 9476–9483. <https://doi.org/10.1039/C3RA48082H>
- Madakka, M., Jyrajau, N., & Rajesh, N. (2018). Mycosynthesis of silver nanoparticles and their characterization. *MethodsX*, 5, 20–29. <https://doi.org/10.1016/j.mex.2017.12.003>
- Marcato, P. D., & Durán, N. (2008). New aspects of nanopharmaceutical delivery systems. *Journal of Nanoscience and Nanotechnology*, 8(5), 2216–2229. <https://doi.org/10.1166/jnn.2008.274>
- Mukherjee, P., Ahmad, A., Mandal, D., Senapati, S., Sainkar, S. R., Khan, M. I., Parishcha, R., Ajaykumar, P., Alam, M., & Kumar, R. (2001). Fungus-mediated synthesis of silver nanoparticles and their immobilization in the mycelial matrix: A novel biological approach to nanoparticle synthesis. *Nano Letters*, 1(10), 515–519. <https://doi.org/10.1021/nl0155274>
- Naqvi, S. Z., Kiran, U., Ali, M. I., Jamal, A., Hameed, A., Ahmed, S., & Ali, N. (2013). Combined efficacy of biologically synthesized silver nanoparticles and different antibiotics against multidrug-resistant bacteria. *International Journal of Nanomedicine*, 8, 3187–3195. <https://doi.org/10.2147/IJN.S49284>
- Omri, A., Suntres, Z. E., & Shek, P. N. (2002). Enhanced activity of liposomal polymyxin B against *Pseudomonas aeruginosa* in a rat model of lung infection. *Biochemical Pharmacology*, 64(8),

- 1407–1413. [https://doi.org/10.1016/S0006-2952\(02\)01346-1](https://doi.org/10.1016/S0006-2952(02)01346-1)
- Panwar, P., Pandey, B., Lakhera, P., & Singh, K. (2010). Preparation, characterization, and in vitro release study of albendazole-encapsulated nanosize liposomes. *International Journal of Nanomedicine*, 5, 101–107. <https://doi.org/10.2147/IJN.S8030>
- Patra, J. K., Das, G., Fraceto, L. F., Campos, E. V. R., Rodriguez-Torres, M. P., Acosta-Torres, L. S., Diaz-Torres, L. A., Grillo, R., Swamy, M. K., & Sharma, S. (2018). Nano-based drug delivery systems: Recent developments and future prospects. *Journal of Nanobiotechnology*, 16, 71. <https://doi.org/10.1186/s12951-018-0392-8>
- Rivera Gil, P., Oberdörster, G., Elder, A., Puentes, V., & Parak, W. J. (2010). Correlating physicochemical with toxicological properties of nanoparticles: The present and the future. *ACS Nano*, 4(10), 5527–5531. <https://doi.org/10.1021/nn1025687>
- Sadowski, Z., Maliszewska, I., Grochowalska, B., Polowczyk, I., & Kozlecki, T. (2008). Synthesis of silver nanoparticles using microorganisms. *Materials Science-Poland*, 26(2–3), 419–424.
- Schumacher, I., & Margalit, R. (1997). Liposome-encapsulated ampicillin: Physicochemical and antibacterial properties. *Journal of Pharmaceutical Sciences*, 86(6), 635–641. <https://doi.org/10.1021/js9503690>
- Shahzad, A., Saeed, H., Iqtedar, M., Hussain, S. Z., Kaleem, A., Abdullah, R., Sharif, S., Naz, S., Saleem, F., & Aihetasham, A. (2019). Size-controlled production of silver nanoparticles by *Aspergillus fumigatus* BTCB10: Likely antibacterial and cytotoxic effects. *Journal of Nanomaterials*, Article ID 2019, 168698. <https://doi.org/10.1155/2019/5168698>
- Shelar, G. B., & Chavan, A. M. (2015). Myco-synthesis of silver nanoparticles from *Trichoderma harzianum* and its impact on germination status of oil seed. *Biolife*, 3(2), 109–113.
- Singh, S., Yadav, A. S., Singh, S. M., & Bharti, P. (2010). Prevalence of *Salmonella* in chicken eggs collected from poultry farms and marketing channels and their antimicrobial resistance. *Food Research International*, 43(8), 2027–2030. <https://doi.org/10.1016/j.foodres.2010.07.021>
- Singh, R., & Nalwa, H. S. (2011). Medical applications of nanoparticles in biological imaging, cell labeling, antimicrobial agents, and anticancer nanodrugs. *Journal of Biomedical Nanotechnology*, 7(4), 489–503. <https://doi.org/10.1166/jbn.2011.1327>
- Torres, I. M. S., Bento, E. B., Almeida, L. D. C., Sá, I. Z. C. M. D., & Lima, E. M. (2012). Preparation, characterization and in vitro antimicrobial activity of liposomal ceftazidime and cefepime against *Pseudomonas aeruginosa* strains. *Brazilian Journal of Microbiology*, 43(4), 984–992. <https://doi.org/10.1590/S1517-83822012000400022>
- Waheed, N. A., Azeez, H. J., & Abachi, F. T. (2016). Combinations of carbapenem with fluoroquinolones or 1,3,4-oxadiazole-2-thione derivatives as new broad spectrum bactericidal antibiotics for ophthalmic preparation. *Journal of Drug Design and Medicinal Chemistry*, 2(5), 47–50. <https://doi.org/10.11648/j.jddmc.20160205.11>
- Yng, O. S. (2005). Liposomal preparations of benzoyl peroxide for the treatment of acne. <https://scholarbank.nus.edu.sg/entities/publication/d9cc9837-5616-4ee2-ba0c-ac6d99c5a4d7>
- Zhang, L., Pornpattananangkul, D., Hu, C. M., & Huang, C. M. (2010). Development of nanoparticles for antimicrobial drug delivery. *Current Medicinal Chemistry*, 17(6), 585–594. <https://doi.org/10.2174/092986710790416290>

RESEARCH ARTICLE

Immature morphology of adult-born granule cells alters responsiveness and excitability in a multi-compartmental conductance-based model

Bahar Sert¹  | Pinar Oz^{1,2,*} 

¹ Department of Neuroscience, Institute of Health Sciences, Üsküdar University, **Istanbul, Türkiye**
ROR ID: 02dzjmc73

² Department of Molecular Biology and Genetics(Engl.), Faculty of Engineering and Natural Sciences, Üsküdar University, **Istanbul, Türkiye**
ROR ID: 02dzjmc73

* Corresponding author: E-mail: pinar.oz@uskudar.edu.tr; Ph.: +90-216-400-2222.

Citation: Citation: Sert B., & Oz, P. (2025). Immature morphology of adult-born granule cells alters responsiveness and excitability in a multi-compartmental conductance-based model. *The European chemistry and biotechnology journal*, 4, 53-68.
<https://doi.org/10.62063/ecb-57>

License: This article is licensed under a Creative Commons Attribution-NonCommercial 4.0 International License (CC BY-NC 4.0).

Peer review: Double Blind Refereeing.

Ethics statement: It is declared that scientific and ethical principles were followed during the preparation of this study and all studies utilized were indicated in the bibliography (Ethical reporting: editor@euchembioj.com).

Plagiarism Check: Done (iThenticate).
Article has been screened for originality.

Received: 23.02.2025

Accepted: 01.07.2025

Online first: 04.07.2025

Published: 11.07.2025

Abstract

The dentate gyrus of the hippocampus is emerging as a focal target in pattern separation and completion in recent years. Adult neurogenesis in the subgranular zone further provides a unique developmental advantage to this region by supporting the regional activity of newborn granule cells, when required. The contribution of adult-born granule cells (AdB GCs) to the local circuits can be attributed to their differences from embryonic-born mature GCs in terms of their morphological and biophysical characteristics. AdB GCs are highly excitable cells that show sparse activity. In this study, our focus was on how the morphological distinction of early AdB GCs from mature GCs affects their responsiveness. The reduced multi-compartmental conductance-based models are designed on Python environment with Brian2 module with simple Hodgkin-Huxley type Na and K conductances. Our results indicate that the early morphology of AdB GCs is optimized for faster action potential kinetics and higher excitability compared to mature GCs, even without any biophysical differences.

Keywords: Adult-Born Granule Cells, Mature Granule Cells, Computational Models of Granule Cells, Morphology, Neural Dynamics.



Introduction

The hippocampal trisynaptic circuit and extensive connections with entorhinal cortex neurons form a microcircuit that is crucial in spatial memory encoding, storage and recall (Remondes & Schuman, 2003). Dentate gyrus (DG) plays a key role especially in the pattern separation and distinction paradigms (Chavlis et al., 2017; Marr, 1971; Santoro, 2013; Treves & Rolls, 1994; Yassa & Stark, 2011). In mammals, adult neurogenesis in the subgranular zone of DG has the potential of generating adult-born (AdB) immature granule cells (GC) that can be integrated into the DG circuitry and modulate the activity in the region (Coulter & Carlson, et al., 2007). The adult-born (AdB) immature neurons have distinct morphological and biophysical features when compared to embryonic-born mature granule cells (GCs), which rises several questions about their contribution to the regional function (Zhao et al., 2006; Llorens-Martin et al., 2015; Llorens-Martin et al., 2016).

The elliptical cell body of the mature DG GC is 10–18 μm in diameter (Amaral et al., 2007). The apical dendrites of GC extend and branch into the molecular layer, where the axonal projections from entorhinal cortex (EC) cells, i.e. layer II stellate cells, reach to form glutamatergic synapses (Zhou et al., 2004). GC axons branch extensively throughout the hilus as they project further to contact CA3 pyramidal neuron apical dendrites (Lee et al., 2014). The nonmyelinated GC axons with several collaterals (a.k.a. mossy fibers) also communicate heavily with the interneurons around the GC layer. Among the interneurons of DG, parvalbumin-positive (PV) basket cells and somatostatin-positive interneurons are known to regulate GC activity through reciprocal connections (Lee et al., 2014).

The GC morphology (i.e., dendritic and axonal branching patterns) (Figure 1) and its wide range of connections (e.g., mossy fibers projecting to the CA3 region) allow them to filter perforant pathway inputs arriving in the molecular layer of DG and project signals to the CA3 selectively. Here, they play a key role in pattern separation, which ensures similar input patterns are stored as distinct representations in the hippocampus (Yassa & Stark, 2011). The unmyelinated axons of GC with dense collaterals form the mossy fibers that project to the apical dendrites of CA3 pyramidal neurons.

AdB GCs have initial electrophysiological characteristics different from mature GCs. They have a higher input resistance, lower voltage thresholds, and slower membrane time constants (Amaral et al., 2007). They are also more prone to LTP (Espósito et al., 2005; Laplagne et al., 2006). Input resistance for mature GCs is around 100–300 $\text{M}\Omega$, where it can be as high as 4 $\text{G}\Omega$ for AdB GCs (Heigele et al., 2016). GCs have reduced ion channels that open at resting potential, such as inward-rectifier potassium channels (Kir). The kinetics of Kir, as well as dendritic and axonal processes, increase the input resistance of immature neurons up to 1 $\text{G}\Omega$ (Liu et al., 1996; Schmidt-Hieber et al., 2004). Another distinctive feature of AdB GCs is the short-term expression of T-type calcium channels, which underlies the sudden voltage spike caused by low-threshold calcium induced by physiological conditions (Goncalves et al., 2016). However, mature GCs are unable to produce calcium-induced voltage spikes to a low threshold and no significant sodium-induced voltage spikes are seen when pharmacologically blocking T-type channels (Schmidt-Hieber et al., 2004). Action potentials initiated by sodium currents trigger short-term calcium currents with a high amplitude in both mature and AdB GCs (Stocca et al., 2008). However, AdB GCs can perform temporal summation of inputs more efficiently than mature GCs because they show longer-lasting temporal wave spikes in their proximal and distal dendrites (Stocca et

al., 2008). Differences in calcium currents may also result from synaptic plasticity. Dendrites of mature GCs are generally described as passive integrators that strongly dampen voltage signals (Krueppel et al., 2011). As a consequence, the amplitude of the backpropagating action potential is attenuated throughout the dendrites of mature GCs, and excitatory postsynaptic potentials (EPSPs) show a steep decline from the dendrites to the soma.

Our focus on morphology in the model is to study structural characteristics without delving into other functional aspects. Morphological analysis provides valuable insights into the physical organization and development of cells, which is crucial for understanding how these structures relate to overall neural activity and behavior. Focus on morphology helps to examine how variations in cell shape, size, and organization contribute to broader cognitive and physiological processes. This approach allows for a more controlled and specific investigation of the structural factors involved.

Materials and methods

The model construction and simulations were performed in a Python environment with the Brian2 module (Stimberg et al., 2019). The analyses were performed with user-defined functions in Python, partially utilizing Brian2. The morphological parameters were gathered through a survey of *in vitro* and *in vivo* experimental findings and reduced into a simplified multi-compartmental topology that reflects the main branching patterns. Simulations were run with a time step $\Delta t = 0.01$ ms and the implicit backward Euler integration. The voltage traces were recorded from the midpoint of every compartment. All custom scripts and simulation codes used in this study will be shared publicly through ModelDB or GitHub to ensure transparency and reproducibility.

Morphological design

The model topology and morphological parameters are determined by a comparative analysis of existing experimental and computational studies. The morphologies used to construct simplified topological models in Figure 1 were derived from Chavlis et al. (2017), specifically granule cells of the dentate gyrus from rats. We included a total of 2 granule cells as adults born (very early developmental stage) and mature. These morphologies were chosen to represent the morphologically most diverse developmental stages and ensure consistent topological comparison. The most striking morphological difference between mature and AdB GCs is the length and branching of the axon, which was reflected in the reduced topology of our models. For dendritic branching, we adapted the 3-dendrite model of Chavlis et al. (2017), with shortened segment length in AdB GCs. The general topology of the morphological parameters for each compartment of GCs is given in Table 1.

Table 1. Morphological parameters of DG GC models.

		<i>Mature GC</i>			<i>Immature AdB GC</i>		
		Length (μm)	Initial Diameter (μm)	End Diameter (μm)	Length (μm)	Initial Diameter (μm)	End Diameter (μm)
<i>Soma</i>		12	12	-	10	10	-
<i>Dendrite</i>	<i>Stem</i>	1	3	1.9	1	3	1.9
	<i>Proximal I</i>	20	0.95	0.95	20	1	0.95
	<i>Proximal II</i>	55	0.95	0.9	25	0.95	0.9
	<i>Medial</i>	75	0.9	0.8	45	0.9	0.8
	<i>Distal</i>	75	0.8	0.8	45	0.8	0.8
	<i>Lamina Moleculare</i>	50	0.8	0.8	25	0.8	0.8
<i>Axon</i>	<i>Axon Hillock</i>	10	1.5	1.3	10	1.5	1.3
	<i>Axon Initial Segment</i>	40	1.3	1	40	1.3	1
	<i>Axonal Segment</i>	100	1	1	100	1	1
	<i>Axon Terminal</i>	4	1	2	4	1	2

Detailed topology of the models is given in Figure 1.

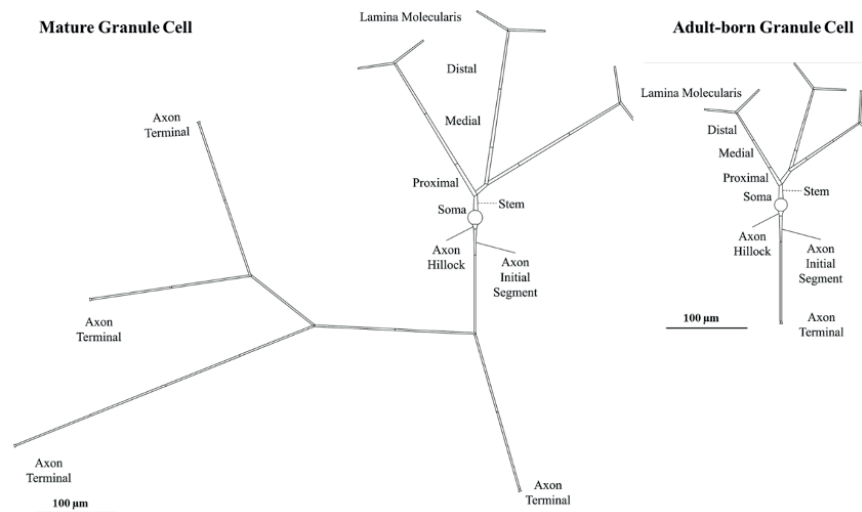


Figure 1. DG Mature GC and Immature AdB GC Model Morphologies. Simplified topologies of mature and adult-born granule cells derived from averaged morphologies in rodent GC samples (Chavlis et al., 2017). These topologies are schematic representations used for compartmental modeling purposes and do not correspond to direct reconstructions. In both models, the proximal segment on the right branches into two, where the segment prior to the branching point is titled as Proximal I and the segment after the branching point is titled as Proximal II. Mature GC axon has three branching points: (1) Immediately after the first axonal segment, where the right branch (axon.R) consists of two axonal segments and an axon terminal, (2) after the second segment on the left branch (axon.L), followed by a four-segment long left branch (axon.LL) ending with an axon terminal, and a right branch (axon.LR), (3) after the first segment of axon.LR, each branch has two axonal segments ending with axon terminals. Immature AdB GC has only one axonal segment followed by an axon terminal.

Biophysical model

The conductance-based model was designed as

$$C_m \frac{dv}{dt} = -I_m - I_{syn} + I_{inj}$$

where the membrane capacitance, C_m , was $0.88 \mu\text{F}/\text{cm}^2$ for AdB GC and $1 \mu\text{F}/\text{cm}^2$ for mature GC. The membrane current, I_m , consisted of Hodgkin-Huxley type Na^+ , K^+ and leak conductances as

$$I_m = g_L(v - E_L) + g_{Na}m^3h(v - E_{Na}) + g_Kn^4(v - E_K)$$

where the leak conductance, g_L , was $0.0003 \text{ S}/\text{cm}^2$ and the specific K_v channel conductance, g_K , was $0.036 \text{ S}/\text{cm}^2$ for all compartments. The density distribution of Na_v channels are reflected on the

specific channel conductance, g_{Na} , as 0.05 S/cm² for soma, 0.5 S/cm² for AIS and NR, and 0.005 S/cm² for dendrites. The reversal potentials were $E_L = -76.5$ mV, $E_{Na} = 50$ mV and $E_K = -90$ mV.

The gating kinetics for any voltage-gated channel was defined as the activation and inactivation rates of channel subunits as

$$\frac{dz}{dt} = \frac{z_{\infty} - z}{\tau_z}$$

$$z_{\infty} = \frac{\alpha_z}{\alpha_z + \beta_z}$$

$$\tau_z = \frac{1}{\alpha_z + \beta_z}$$

where z is a generalized gating particle. The gating kinetics for Na_v was defined over the activation (m) and inactivation (h) functions, whereas K_v was defined with a singular activation (n) function as follows (Aradi & Holmes, 1999) :

$$\alpha_m = \frac{0.32(13 - v_T)}{e^{\frac{13-v_T}{4}} - 1}$$

$$\beta_m = \frac{0.28(v_T - 40)}{e^{\frac{v_T-40}{5}} - 1}$$

$$\alpha_h = 0.128 e^{\frac{17-v_T}{18}}$$

$$\beta_h = \frac{4}{1 + e^{\frac{40-v_T}{5}}}$$

$$\alpha_n = \frac{0.032(15 - v_T)}{e^{\frac{15-v_T}{5}} - 1}$$

$$\beta_n = 0.5 e^{\frac{10-v_T}{40}}$$

Current injection

In order to mimic the rheobase activity driven by baseline ionic current load at a given time, a sustained constant current (I_{inj}) was placed at the soma for each cell. The measurements for the characterization of action potential waveforms are performed on voltage traces from soma and axon initial segment (AIS) with the minimum input current required for generating an action potential, $I_{inj} = I_{min}$. Firing rate responses and frequency-current plots were also obtained under constant current, increased with repeated tests with a current increment ΔI for a duration of $T = 200$ ms for each step.

Model response analysis

Action potential waveform characteristics. We defined the characteristics of each cell's action potential waveform over threshold potential (V_{thr}), onset rapidness (ρ), peak potential (V_{peak}) and action potential width ($\Delta t_{1/2}$). V_{thr} was measured as the voltage at the time when reaches and

exceeds 10 V/s (Naundorf et al., 2006; Oz et al., 2015).. The action potential half amplitude ($V_{1/2}$) was measured as the half difference between V_{peak} and V_{thr} , and $\Delta t_{1/2}$ was estimated as the full width of action potential at $V_{1/2}$. The two methods used to measure ρ were the inverse full width at half maximum (IFWd²) and the inverse half width at half maximum (IHWd²) of d^2V/dt^2 peak as described by Aldohbeyb et al. (2021).

Action potential propagation. The delay of action potential propagation from AIS to other compartments (t_d) was measured as $t_d = t_{1/2,i} - t_{1/2,AIS}$ where $V_m(t_{1/2,i}) = V_{1/2,i}$ at compartment “i”. The attenuation of action potential amplitude was recorded by the attenuation of V_{peak} ($V_{peak,i}$) at compartment “i” as $V_{peak,i} = V_{peak,AIS} - V_{peak,i}$. Both t_d and $V_{peak,i}$ were plotted over the distance to the center of AIS from the center of the respective compartments. The velocity of dendritic (v_d) and axonal (v_a) propagation was estimated by fitting a (x, t_d) plot with a linear function, $x = v t + a$, where a is a constant.

Frequency-current plots. The frequency – current (fI) plots were obtained by injecting a step-wise increasing constant current for 200 ms intervals, starting with $I_{inj} < I_{min}$. And increasing with the increment ΔI . The firing frequency was estimated over the somatic voltage traces.

The action potentials (APs) from soma and axon initial segment (AIS) of mature and AdB GCs were recorded under constant current injection at the soma ($I_{inj} = I_{min}$), which resulted in a 10 Hz firing rate. The changes in V_{peak} for AdB and mature GCs are given in Table 2.

Results and discussion

The goal of this study was to reveal how the distinct morphological features of adult-born granule cells (AdB GCs) impact neural response characteristics. To this end, we constructed conductance-based models of both AdB and mature GCs using reduced topologies that emphasize their most distinctive morphological difference—axon length and branching patterns (Zhao et al., 2006). By implementing identical biophysical parameters across both models, we isolated the effect of morphology and eliminated confounding influences from intrinsic membrane properties.

Interestingly, our results showed that AdB GCs achieved firing rates similar to those of mature GCs in response to increasing constant input current. Additionally, parameters such as somatic backpropagation delay, dendritic propagation, and signal attenuation were comparable across the two models. This finding aligns with previous studies reporting that smaller somatic size and less dendritic arborization in AdB GCs lead to lower capacitance and faster signal conduction (Brunner et al., 2014), while mature GCs exhibit greater capacitance and slower temporal dynamics. Schmidt-Hieber et al. (2004) also demonstrated that the current threshold is lower in AdB GCs (141 ± 12 pA) compared to mature GCs (234 ± 9 pA), which typically corresponds to a lower voltage threshold, consistent with our observation of higher excitability in AdB GCs.

Although our models revealed no significant differences in propagation rates or frequency-current (f-I) relationships, this may be due to the simplified biophysical characteristics. Thomas et al. (2009) showed that variations in sodium and potassium channel gating kinetics significantly influence firing dynamics in more detailed models. The use of identical channel kinetics in our approach likely explains the lack of divergence in f-I curves, a finding also supported by Tejada & Roque (2014).

Recent modeling frameworks such as TREES-to-NEURON (T2N) offer enhanced integration of complex morphologies with compartmental biophysics (Beining et al., 2017), supporting more realistic simulations of AdB and mature GC function. However, in this study, the use of a reduced,

yet representative multi-compartmental morphology combined with a simplified Hodgkin-Huxley (HH) type limited to Na^+ and K^+ currents allowed us to focus on morphological contributions while minimizing the variability introduced by differing ion channel dynamics.

Action potential waveform characteristics

The APs from soma and AIS of mature GC and immature AdB GCs were recorded under constant current injection at the soma, which resulted in a 10 Hz firing rate. The changes in V_{peak} , V_{thr} , $\Delta t_{1/2}$ and ρ according to two different methods (IFWd² and IHWd²) for AdB and mature GCs are given in Table 3. V_{peak} is 34.5 mV for mature GCs and 34.7 mV for immature AdB GC. The timing of AP is also slightly different, with mature GC initiating a spike slightly later than AdB GC (Figure 2-A and C). For AIS, V_{peak} for mature GC is 46.1 mV and 47.6 mV for immature AdB GC. This indicates that strong depolarization occurs at AIS for both groups, with a slightly higher maximum potential in AdB GC. V_{thr} is approximately -37.4 mV for mature GC and approximately -39.8 mV for AdB GC both in soma and AIS. This indicates the higher excitability of immature AdB GC. Moreover, the $V_{1/2}$ is -2.5 mV for AdB GC and -1.4 mV for mature GC, which implies that AdB GC might have a faster depolarization phase. The $\Delta t_{1/2}$ values for both models are similar at the soma and AIS. For the onset rapidness (ρ), the IFWd² method yielded a notable difference between AdB (20 ms⁻¹) and mature GCs (12.5 ms⁻¹), which indicates sharper AP onsets for immature AdB GC at soma (Figure 2-B).

Table 3. Action potential waveform characteristics for mature GC and immature AdB GC models.

	SOMA						AIS					
	V_{peak} (mV)	V_{thr} (mV)	$V_{1/2}$ (mV)	$\Delta t_{1/2}$ (ms)	$\rho(\text{IFWd}^2)$ (ms ⁻¹)	$\rho(\text{IHWd}^2)$ (ms ⁻¹)	V_{peak} (mV)	V_{thr} (mV)	$V_{1/2}$ (mV)	$\Delta t_{1/2}$ (ms)	$\rho(\text{IFWd}^2)$ (ms ⁻¹)	$\rho(\text{IHWd}^2)$ (ms ⁻¹)
Mature GC	34.5	-37.4	-1.4	0.46	12.5	33.3	46.1	-37.4	4.3	0.66	25	50
AdB GC	34.7	-39.8	-2.5	0.48	20	33.3	47.6	-39.8	3.9	0.66	25	33.3

Immature AdB GC displayed a slightly higher peak depolarization velocity (ρ) compared to mature GC in AIS (Figure 2-D). AdB GC also displayed a steeper depolarization rate (ρ) at soma compared to the mature GC (Figure 2-B). It was previously shown that AdB GCs are hyperexcitable and display a faster depolarization phase compared to mature GCs (Vyleta & Snyder, 2023), which is in agreement with our findings.

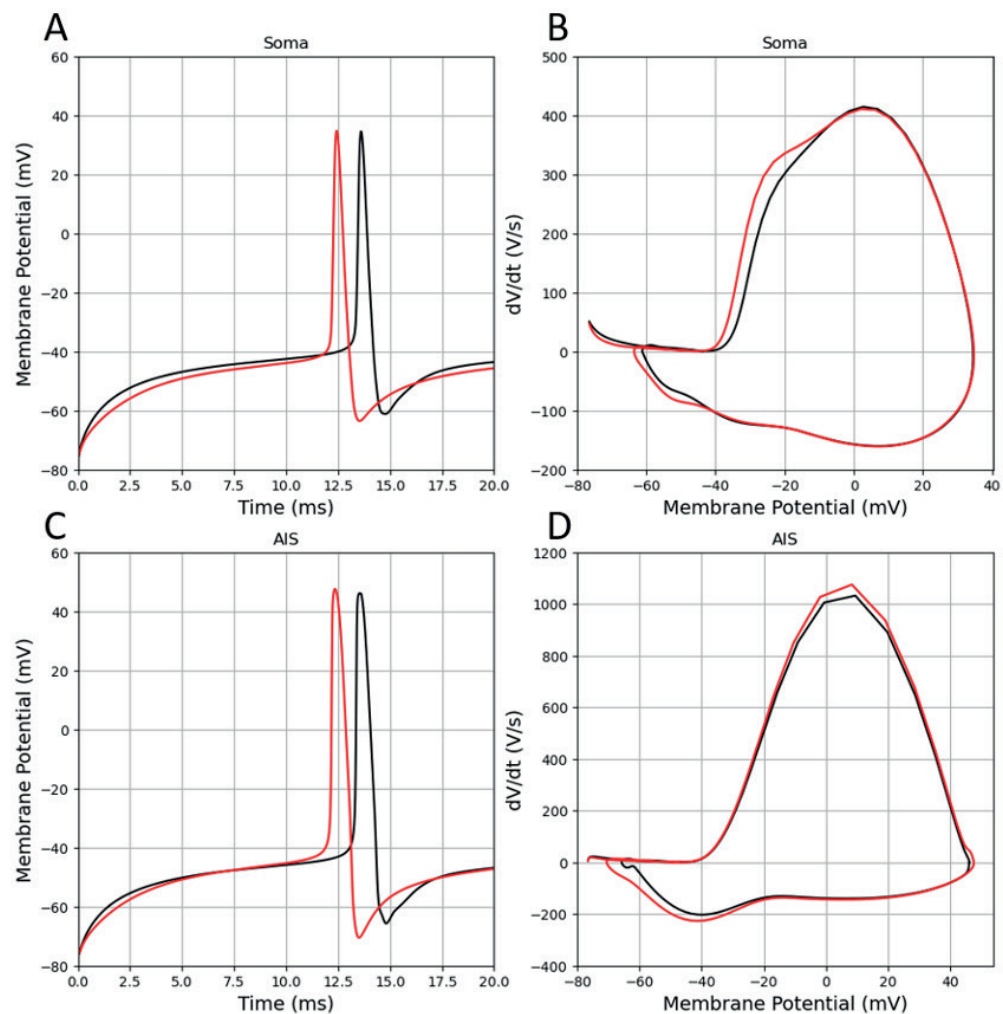


Figure 2. Action Potentials and Phase Plots from mature GC and immature AdB GCs. Black: Mature GC, Red: Immature AdB GC. A-B: Soma, C-D: AIS.

In our immature AdB GC model, the length of the axon is considerably shorter and can not reach to CA3. The model was designed to reflect the early phases of immature AdB GCs, where they strictly limit their communication to local interneurons. It has been suggested that the excitability of GCs decreases with maturation, and they become tightly coupled to inhibitory circuits (Brunner et al., 2014). Our findings also replicate this notion and may indicate that the morphological differences between immature AdB and mature GC models may be sufficient to reproduce the higher excitability of AdB GC.

Frequency-current relationship

The f-I curve (Figure 3) shows how the firing rate coupled to the injected current amplitude. Both models display a Type I respond, with a nonlinear increase in frequency as the amplitude of the current injection increases. At low input current increments, the increase in firing rate grows relatively fast, while at higher input current increments the increase becomes slower approaching saturation.

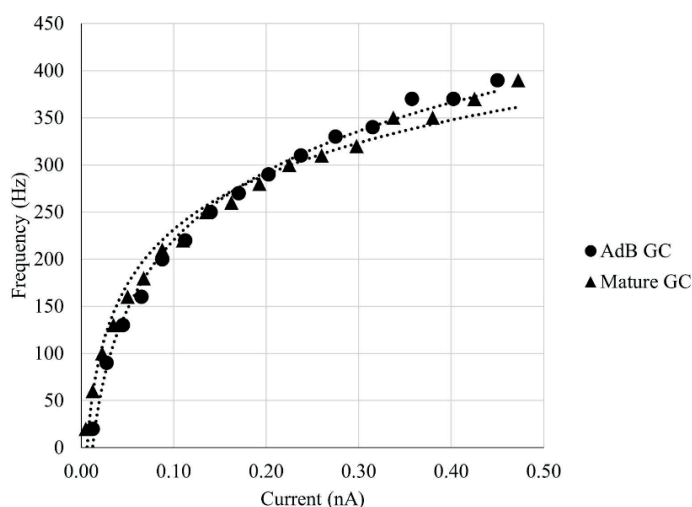


Figure 3. Frequency-current amplitude curves for mature GC and immature AdB GCs. The dotted lines represent the curve fitting as explained in the text.

The firing rate (f) in response to current (I) injection were fit with the function $f = f_h * \ln(I) + f_{limit}$ using least square method with Levenberg-Marquadt algorithm, where f_h is the inflection frequency and f_{limit} is the saturation frequency. The variables and root mean square deviation (RMSD) for mature and immature AdB GCs are given in Table 4. The f - I curves for mature GC and immature AdB GCs slightly differ in f_h and f_{limit} . The f_h of immature AdB GC is slightly lower than mature GC, however, the firing rates converge, showing that the two cell types exhibit similar maximal firing capacities at higher currents.

Table 4. Frequency-Current Plot Curve Fitting Parameters. f_h : Inflection frequency, f_{limit} : Limiting saturation frequency, RMSD : Root mean square deviation for least square method.

	f_h	f_{limit}	RMSD
Mature GC	105.2	462.45	0.9923
AdB GC	83.714	424.27	0.9781

Action potential propagation

The delay (Δt_d) of AP propagation from AIS to other compartments was measured as $\Delta t_d = t_{1/2,i} - t_{1/2,AIS}$ where $V_{m,i}(t_{1/2}) = V_{1/2,i}$ at the midpoint of the AP in compartment 'i'. Linear regression was performed to calculate the velocities of dendritic (v_d) and axonal (v_a) AP propagation by fitting (x , Δt_d) plot with the function $x = v t + a$, where a is a constant (Table 5). Mature GC and immature AdB GCs show increased delay with increasing distance from AIS (Figure 4-A and B), where immature AdB GC exhibits slower dendritic back-propagation compared to mature GC (Table 5). The high v_a for immature AdB GC might be due to the shorter and non-branching axon of this model compared to mature GC.

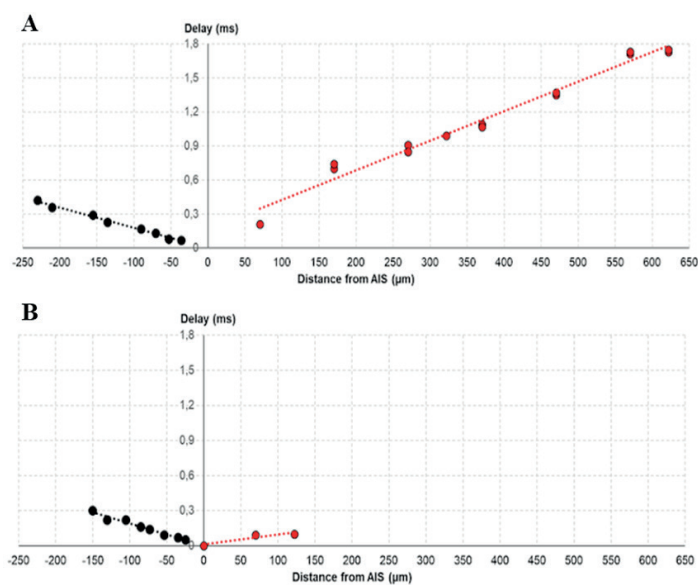


Figure 4. Distance-dependent (x,t) delay in action potential propagation for mature GC (A) and immature AdB GC (B).

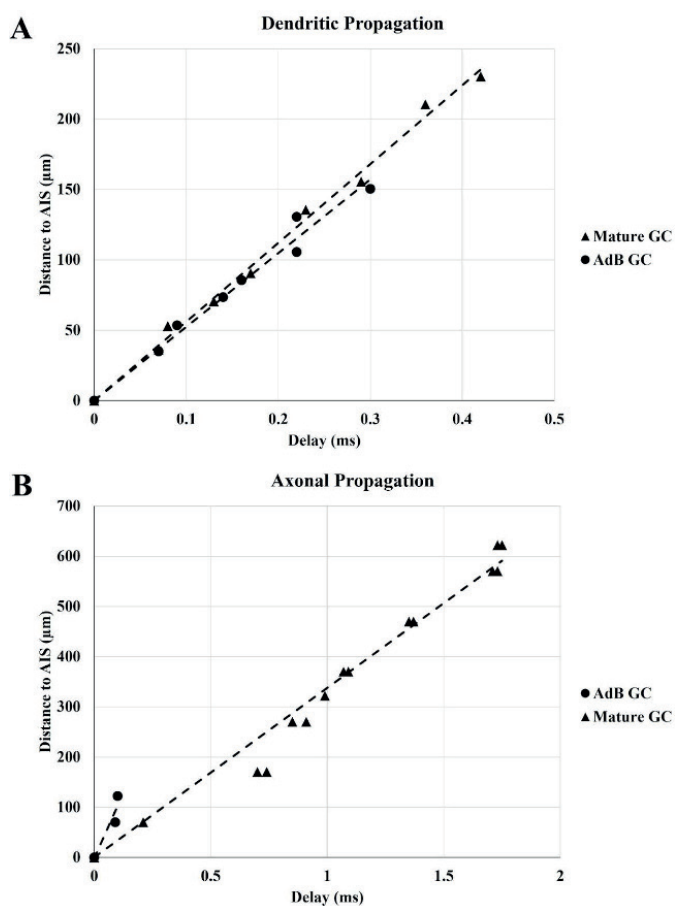


Figure 5. Delay-dependent distance (t,x) in action potential propagation for dendritic and axonal propagation.

gation for mature GC and immature AdB GC. Dendritic propagation is given in (A) and axonal propagation in (B).

Table 5. The velocity of dendritic (v_d) and axonal (v_a) propagation for mature GC and immature AdB GC.

	v_d ($\mu\text{m/ms}$)	v_a ($\mu\text{m/ms}$)
Mature GC	560.21	337.57
AdB GC	523.69	1045.1

The attenuation of AP amplitude ($\Delta V_{\text{peak},i}$) across dendritic and axonal compartments was calculated by the attenuation of $V_{\text{peak},i}$ at compartment “i” as $\Delta V_{\text{peak},i} = V_{\text{peak,AIS}} - V_{\text{peak},i}$. Both GCs exhibit a decrease in dendritic V_{peak} as distance increases (Figure 6), but there is no significant difference between both models. This implies that AdB GC display similar performance in dendritic backpropagation in terms of signal integrity and propagation efficiency.

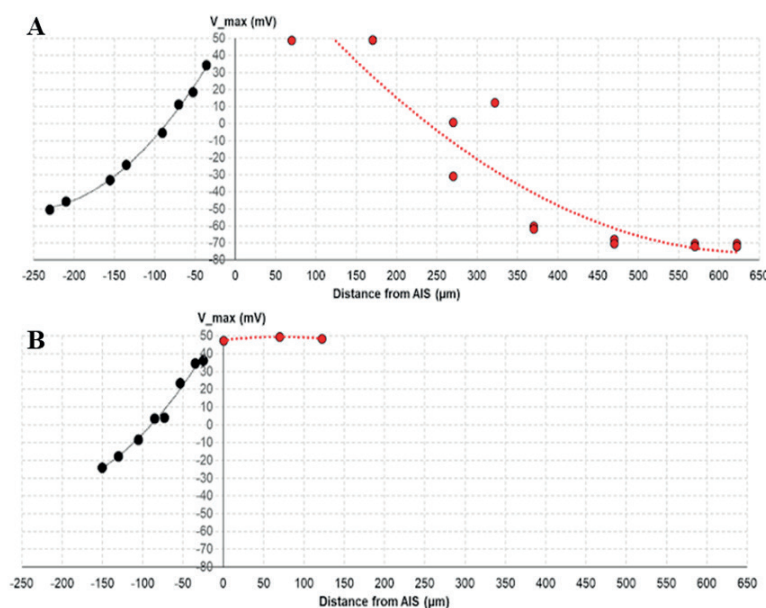
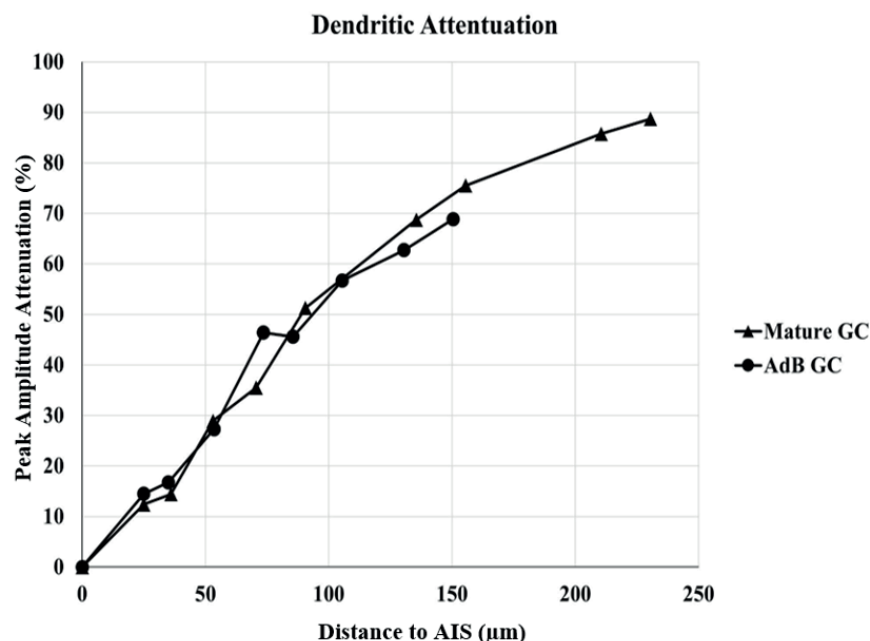


Figure 6. V_{peak} -dependent (t-x) distance in action potential propagation for mature GC (A) and immature AdB GC (B).



| **Figure 7.** The dendritic peak AP amplitude attenuation in GC models.

For our goal, the use of the HH model allowed for precise isolation of ionic dynamics because it provides a biophysically simplified conductance-based model. Keeping the biophysical parameters constant in both models was essential for isolating and addressing how distinct morphological features impact the neural response characteristics. Compared to more advanced models, such as T2N (Beining et al., 2017) and SAS (Santhakumar et al., 2005), our models certainly have limitations, e.g., our model does not focus on biophysical properties where it focuses on morphological comparison.

Conclusions

Morphological differences between mature and AdB GCs have been shown to have an impact on dentate gyrus functionality. In particular, structural differences such as dendrite branching and sizes of compartments have provided insight into how these cells play different roles in information processing. Future research should focus on the axonogenesis and the maturation stages of the AdB GC model, as it would be helpful in understanding how the change of response and excitability during their integration into the hippocampal network. Additionally, exploring how the ratio of AdB GCs in the total GC population in DG influences the microcircuit response and hippocampal function can explain the balance between circuit stability and responsiveness. Investigating an optimal neurogenesis range may reveal critical thresholds for therapeutic interventions in conditions such as depression, epilepsy, and age-related cognitive decline.

Acknowledgements

The authors would like to thank Çağla Koca and Berzan Burulday for their support.

Funding

This research was not funded by an organization.

Conflict of interest

The authors declare no conflict of interest.

Data availability statement

Data can be obtained from the corresponding author upon a reasonable request.

Ethics committee approval

Ethics committee approval is not required for this study.

Authors' contribution statement

The authors acknowledge their contributions to this paper as follows: **Study conception and design:** PÖ; **Data collection:** BS; **Analysis and interpretation of results:** BS, PÖ; **Manuscript draft preparation:** BS, PÖ. All authors reviewed the results and approved the final version of the manuscript.

Use of Artificial Intelligence: No artificial intelligence-based tools or applications were used in the preparation of this study. The entire content of the study was produced by the author(s) in accordance with scientific research methods and academic ethical principles.

ORCIDs and emails of the authors

Bahar Sert | ORCID 0009-0003-3806-9791 | bahaarsertt@gmail.com

Pinar Oz | ORCID 0000-0001-6006-9921 | pinar.oz@uskudar.edu.tr

References

- Aldohbeyb, A. A., Vigh, J., & Lear, K. L. (2021). New methods for quantifying rapidity of action potential onset differentiate neuron types. *PLOS ONE*, 16(4), e0247242. <https://doi.org/10.1371/journal.pone.0247242>
- Amaral, D. G., Scharfman, H. E., & Lavenex, P. (2007). The dentate gyrus: Fundamental neuroanatomical organization (dentate gyrus for dummies). *Progress in Brain Research*, 163, 3–790. [https://doi.org/10.1016/S0079-6123\(07\)63001-5](https://doi.org/10.1016/S0079-6123(07)63001-5)
- Aradi, I., & Holmes, W. R. (1999). Role of multiple calcium and calcium-dependent conductances in regulation of hippocampal dentate granule cell excitability. *Journal of Computational Neuroscience*, 6(3), 215–235. <https://doi.org/10.1023/A:1008801821784>
- Beining, M., Jungenitz, T., Radic, T., Deller, T., Cuntz, H., Jedlicka, P., & Schwarzacher, S. W. (2017). Adult-born dentate granule cells show a critical period of dendritic reorganization and are distinct from developmentally born cells. *Brain Structure and Function*, 222(3), 1427–1446. <https://doi.org/10.1007/s00429-016-1285-y>
- Brunner, J., Neubrandt, M., Van-Weert, S., Andrási, T., Kleine Borgmann, F. B., Jessberger, S., & Szabadics, J. (2014). Adult-born granule cells mature through two functionally distinct states. *eLife*, 3, e03104. <https://doi.org/10.7554/eLife.03104>
- Chavlis, S., Petrantonakis, P. C., & Poirazi, P. (2017). Dendrites of dentate gyrus granule cells

- contribute to pattern separation by controlling sparsity. *Hippocampus*, 27(1), 89–110. <https://doi.org/10.1002/hipo.22675>
- Coulter, D. A., & Carlson, G. C. (2007). Functional regulation of the dentate gyrus by GABA-mediated inhibition. *Progress in Brain Research*, 163, 235–812. [https://doi.org/10.1016/S0079-6123\(07\)63014-3](https://doi.org/10.1016/S0079-6123(07)63014-3)
- Espósito, M. S., Piatti, V. C., Laplagne, D. A., Morgenstern, N. A., Ferrari, C. C., Pitossi, F. J., & Schinder, A. F. (2005). Neuronal differentiation in the adult hippocampus recapitulates embryonic development. *The Journal of Neuroscience*, 25(44), 10074–10086. <https://doi.org/10.1523/JNEUROSCI.3114-05.2005>
- Gonçalves, J. T., Schafer, S. T., & Gage, F. H. (2016). Adult neurogenesis in the hippocampus: From stem cells to behavior. *Cell*, 167(4), 897–914. <https://doi.org/10.1016/j.cell.2016.10.021>
- Krueppel, R., Remy, S., & Beck, H. (2011). Dendritic integration in hippocampal dentate granule cells. *Neuron*, 71(3), 512–528. <https://doi.org/10.1016/j.neuron.2011.05.043>
- Laplagne, D. A., Espósito, M. S., Piatti, V. C., Morgenstern, N. A., Zhao, C., Van Praag, H., Gage, F. H., & Schinder, A. F. (2006). Functional convergence of neurons generated in the developing and adult hippocampus. *PLoS Biology*, 4(12), e409. <https://doi.org/10.1371/journal.pbio.0040409>
- Lee, S. H., Marchionni, I., Bezaire, M., Varga, C., Danielson, N., Lovett-Barron, M., Losonczy, A., & Soltesz, I. (2014). Parvalbumin-positive basket cells differentiate among hippocampal pyramidal cells. *Neuron*, 82(5), 1129–1144. <https://doi.org/10.1016/j.neuron.2014.03.034>
- Liu, Y. B., Lio, P. A., Pasternak, J. F., & Trommer, B. L. (1996). Developmental changes in membrane properties and postsynaptic currents of granule cells in rat dentate gyrus. *Journal of Neurophysiology*, 76(2), 1074–1088. <https://doi.org/10.1152/jn.1996.76.2.1074>
- Llorens-Martín, M., Jurado-Arjona, J., Avila, J., & Hernandez, F. (2015). Novel connection between newborn granule neurons and the hippocampal CA2 field. *Experimental Neurology*, 263, 285–292. <https://doi.org/10.1016/j.expneurol.2014.10.021>
- Llorens-Martín, M., Rábano, A., & Ávila, J. (2016). The ever-changing morphology of hippocampal granule neurons in physiology and pathology. *Frontiers in Neuroscience*, 9, 526. <https://doi.org/10.3389/fnins.2015.00526>
- Marr, D. (1971). Simple memory: A theory for archicortex. *Philosophical Transactions of the Royal Society of London. Series B, Biological Sciences*, 262(841), 23–81. <https://doi.org/10.1098/rstb.1971.0078>
- Naundorf, B., Wolf, F., & Volgushev, M. (2006). Unique features of action potential initiation in cortical neurons. *Nature*, 440(7087), 1060–1063. <https://doi.org/10.1038/nature04610>
- Oz, P., Huang, M., & Wolf, F. (2015). Action potential initiation in a multi-compartmental model with cooperatively gating Na channels in the axon initial segment. *Journal of Computational Neuroscience*, 39, 63–75. <https://doi.org/10.1007/s10827-015-0561-9>
- Remondes, M., & Schuman, E. M. (2003). Molecular mechanisms contributing to long-lasting synaptic plasticity at the temporoammonic-CA1 synapse. *Learning & Memory*, 10(4), 247–252. <https://doi.org/10.1101/lm.59103>
- Rolls, E. T. (2010). A computational theory of episodic memory formation in the hippocampus.

- Behavioural Brain Research*, 215(2), 180–196. <https://doi.org/10.1016/j.bbr.2010.03.027>
- Santhakumar, V., Aradi, I., & Soltesz, I. (2005). Role of mossy fiber sprouting and mossy cell loss in hyperexcitability: A network model of the dentate gyrus incorporating cell types and axonal topography. *Journal of Neurophysiology*, 93(1), 437–453. <https://doi.org/10.1152/jn.00777.2004>
- Santoro, A. (2013). Reassessing pattern separation in the dentate gyrus. *Frontiers in Behavioral Neuroscience*, 7, 96. <https://doi.org/10.3389/fnbeh.2013.00096>
- Schmidt, B., Marrone, D. F., & Markus, E. J. (2012). Disambiguating the similar: The dentate gyrus and pattern separation. *Behavioural Brain Research*, 226(1), 56–65. <https://doi.org/10.1016/j.bbr.2011.08.039>
- Schmidt-Hieber, C., Jonas, P., & Bischofberger, J. (2004). Enhanced synaptic plasticity in newly generated granule cells of the adult hippocampus. *Nature*, 429(6988), 184–187. <https://doi.org/10.1038/nature02553>
- Stimberg, M., Brette, R., & Goodman, D. F. (2019). Brian 2, an intuitive and efficient neural simulator. *eLife*, 8, e47314. <https://doi.org/10.7554/eLife.47314>
- Stocca, G., Schmidt-Hieber, C., & Bischofberger, J. (2008). Differential dendritic Ca²⁺ signalling in young and mature hippocampal granule cells. *The Journal of Physiology*, 586(16), 3795–3811. <https://doi.org/10.1113/jphysiol.2008.155739>
- Tejada, J., & Roque, A. C. (2014). Computational models of dentate gyrus with epilepsy-induced morphological alterations in granule cells. *Epilepsy & Behavior*, 38, 63–70. <https://doi.org/10.1016/j.yebeh.2014.02.007>
- Thomas, E. A., Reid, C. A., Berkovic, S. F., & Petrou, S. (2009). Prediction by modeling that epilepsy may be caused by very small functional changes in ion channels. *Archives of Neurology*, 66(10), 1225–1232. <https://doi.org/10.1001/archneurol.2009.219>
- Treves, A., & Rolls, E. T. (1994). Computational analysis of the role of the hippocampus in memory. *Hippocampus*, 4(3), 374–391. <https://doi.org/10.1002/hipo.450040319>
- Vyleta, N. P., & Snyder, J. S. (2023). Enhanced excitability but mature action potential waveforms at mossy fiber terminals of young, adult-born hippocampal neurons in mice. *Communications Biology*, 6(1), 290. <https://doi.org/10.1038/s42003-023-04678-5>
- Heigele, S., Sultan, S., Toni, N., & Bischofberger, J. (2016). Bidirectional GABAergic control of action potential firing in newborn hippocampal granule cells. *Nature Neuroscience*, 19(2), 263–270. <https://doi.org/10.1038/nn.4218>
- Yassa, M. A., & Stark, C. E. L. (2011). Pattern separation in the hippocampus. *Trends in Neurosciences*, 34(10), 515–525. <https://doi.org/10.1016/j.tins.2011.06.006>
- Zhao, C., Teng, E. M., Summers, R. G., Jr., Ming, G. L., & Gage, F. H. (2006). Distinct morphological stages of dentate granule neuron maturation in the adult mouse hippocampus. *The Journal of Neuroscience*, 26(1), 3–11. <https://doi.org/10.1523/JNEUROSCI.3648-05.2006>
- Zhou, Q., Homma, K. J., & Poo, M. M. (2004). Shrinkage of dendritic spines associated with long-term depression of hippocampal synapses. *Neuron*, 44(5), 749–757. <https://doi.org/10.1016/j.neuron.2004.11.011>

RESEARCH ARTICLE

Gango + BioFunctional: A Computational tool for efficient functional gene analysis

Alejandro Rodriguez-Mena^{1,2}  | Xavier Tarragó-Claramunt^{1,2}  | Giulia Castellani^{1,3} 
Javier Méndez-Viera^{1,2}  | Antonio Monleón-Getino^{1,2,*} 

¹ BIOST3, Research Group in Biostatistics, Data Science and Bioinformatics, **Barcelona, Spain**
ROR ID: [021018s57](https://orcid.org/021018s57)

² Department of Genetics, Microbiology and Statistics, Universitat de Barcelona, **Barcelona, Spain**
ROR ID: [021018s57](https://orcid.org/021018s57)

³ School of Biosciences and Veterinary Medicine, University of Camerino, **Camerino (MC), Italy**
ROR ID: [0005w8d69](https://orcid.org/0005w8d69)

* **Corresponding author:** E-mail: amonleong@ub.edu (A.M.G.) ; Ph.: ++34-678329864.

Citation: Rodriguez-Mena, A., Tarragó-Claramunt, X., Castellani, G., Méndez-Viera, J., & Monleón-Getino, A. (2025). Gango + BioFunctional: A Computational tool for efficient functional gene analysis. *The European chemistry and biotechnology journal*, 4, 69–80.
<https://doi.org/10.62063/ecb-63>

License: This article is licensed under a Creative Commons Attribution-NonCommercial 4.0 International License (CC BY-NC 4.0).

Peer review: Double Blind Refereeing.

Ethics statement: It is declared that scientific and ethical principles were followed during the preparation of this study and all studies utilized were indicated in the bibliography (Ethical reporting: editor@euchembioj.com).

Plagiarism Check: Done (iThenticate).
Article has been screened for originality.

Received: 03.06.2025
Accepted: 03.07.2025
Online first: 06.07.2025
Published: 11.07.2025

Abstract

Functional gene analysis is crucial for understanding gene roles in biological processes. However, analyzing data with multiple experimental groups presents significant challenges due to the complexity of data processing and the limitations of existing tools. GANGO + BioFunctional, an R-based Shiny application designed for end-users, addresses these challenges by providing a streamlined and comprehensive workflow for functional gene analysis. This interactive and freely available tool requires no installation, thus significantly enhancing its accessibility. The application is composed of two primary modules: GANGO, which efficiently processes input data and performs functional annotation to Gene Ontology (GO) terms and KEGG pathways; and BioFunctional, dedicated to in-depth analysis and interpretation. Key advantages include a highly user-friendly interface that eliminates the need for programming expertise, robust multi-group analytical capabilities, comprehensive visualization tools (interactive networks and significance-driven bar plots), and seamless compatibility with AI-driven interpretation tools like CURIE. Hosted on a server, GANGO + BioFunctional enhances the efficiency and accessibility of functional gene analysis, making it a valuable asset for both specialists and AI applications, ultimately facilitating deeper biological insights.

Keywords: AI Integration, Computational Tool, Functional Gene Analysis, Gene Ontology, KEGG Pathways, Shiny Application.



Introduction

Functional gene analysis (Figure 1, workflow) is a vital process in biology, enabling researchers to elucidate the roles of genes in various biological processes. The typical workflow involves several key steps:

List of Genes of Interest: The analysis begins with a set of genes relevant to a particular study, such as differentially expressed genes, mutated genes associated with a disease, or genes in a specific biological pathway.

- **Gene Annotation:** Genes are annotated with functional information from databases like Gene Ontology (GO) and KEGG. These databases provide details on molecular functions, biological processes, and cellular localization.
- **Enrichment Analysis:** Statistical enrichment analysis identifies over-represented biological functions or pathways within the gene list, highlighting the most relevant biological functions.
- **Visualization and Interpretation:** Results are visualized using tools like bar graphs and network diagrams, aiding in the interpretation of key biological themes within the research question, often with reference to existing literature.

Functional gene analysis yields insights into biological mechanisms and aids in generating hypotheses for further research (Thomas, 2000).

From data to understanding: Addressing the challenges of functional gene analysis

While functional gene analysis provides critical insights, analyzing studies with more than two experimental groups significantly increases complexity. Consider a study on a disease and its progression, with the following groups:

Group 1: Healthy individual

Group 2: Patients with early-stage disease Group 4: Patients with late-stage disease

Identifying genes consistently dysregulated across all stages or specific to a particular stage requires advanced statistical methods. Researchers often rely on multiple software tools and custom scripts (e.g., in R) to manage gene lists, organize data, perform functional analysis, and interpret results. This process is time-consuming, requires programming expertise, and can hinder reproducibility. The lack of user-friendly tools to handle and visualize the complexity of multi-group results therefore necessitates more sophisticated approaches (Gene Ontology Consortium, 2015).

To address these challenges, a specialized computational tool is needed to:

- Enable easy processing of data from multiple experimental groups without requiring programming expertise.
- Provide a user-friendly interface.
- Efficiently handle multiple groups.
- Identify relevant ontologies or KEGG pathways.
- Prepare results for interpretation by specialists and artificial intelligence.

Such a tool would reduce analysis time and effort, improve result accuracy and reliability, and broaden the accessibility of functional gene analysis. GANGO + BioFuncional was developed to provide such a solution.

Benchmarking with existing tools

In response to the need to contextualize the utility of GANGO + BioFuncional, a comparison was conducted with widely used functional enrichment analysis tools such as DAVID, GSEA, and Enrichr. Table 1 provides a benchmark of the main features of these tools compared to GANGO + BioFuncional. Unlike DAVID (Huang et al., 2009) and Enrichr (Chen et al., 2013), GANGO + BioFuncional is specifically designed to simplify the analysis of data with multiple experimental groups, offering an intuitive user interface that minimizes the need for programming knowledge.

Table 1. Benchmark comparison of GANGO + BioFuncional with other widely used functional enrichment analysis tools: DAVID, GSEA, and Enrichr.

Feature / Tool	GANGO + BioFuncional	DAVID	GSEA	Enrichr
Multi-group Analysis	Yes (Simplified)	Limited	Yes (Specific)	Limited
User-Friendly Interface	Yes (Shiny, no code)	Moderate (Web)	Moderate (Software)	High (Web)
AI Integration	Yes (CURIE)	No	No	No
Advanced Visualization	Interactive Networks, Z-score Bar Plots	Basic (Graphs)	Advanced (Plots)	Basic (Bar charts)
Installation Required	No (Server)	No (Web)	Yes	No

It highlights GANGO + BioFuncional's unique features, particularly its simplified multi-group analysis capabilities and an intuitive user interface designed to minimize the need for programming knowledge. Unlike DAVID (Huang et al., 2009) and Enrichr (Chen et al., 2013), GANGO + BioFuncional streamlines the analysis of data from multiple experimental groups. Furthermore, it stands out with its integration of AI through CURIE and offers advanced visualization options such as interactive networks and Z-score bar plots, surpassing the basic visualization features of some other tools. The table also indicates whether each tool requires local installation or is accessible via a server or web interface, with GANGO + BioFuncional, DAVID, and Enrichr being server/web-based, while GSEA requires installation.

While GSEA (Subramanian et al., 2005) also addresses gene set analysis, GANGO + BioFuncional distinguishes itself by its ability to integrate hierarchical ontology information and generate advanced visualizations such as interactive networks and Z-score bar plots, which enhance the interpretability of results. Furthermore, a notable feature of GANGO + BioFuncional is its integration with artificial intelligence technologies (such as CURIE), facilitating a deeper interpretation of GO terms, an aspect that existing tools do not typically offer. This comparison underscores the unique contributions of GANGO + BioFuncional for functional gene analysis in highly complex scenarios.

Materials and methods

GANGO + BioFuncional is a comprehensive R application, built using the Shiny framework (Chang et al., 2025) (DOWNLOAD AND INSTALL IN <https://alexub.shinyapps.io/BioFuncional/>). It facilitates the

interpretation and visualization of functional analysis related to KEGG pathways and gene ontologies (GO) (Alterovitz et al., 2007; Ashburner et al., 2000; Gene Ontology Consortium, 2015; Kanehisa & Goto, 2000). The application provides researchers with detailed functional information, specifically about biological pathways and gene functions. Utilizing libraries such as Shiny, httr, dplyr, tibble, and rvest in R. GANGO + BioFuncional offers a user-friendly interface for data assessment and analysis. The GANGO + BioFuncional tools have been integrated into this Shiny-based R application.

The development of GANGO stems from prior research detailed in article Monleon-Getino et al. (2020), establishing its foundational components. BioFuncional, on the other hand, represents the significant improvements and enhancements that emerged from subsequent work, specifically those described in article Rodriguez and Monleon-Getino (2024).

The application enables the exploration of KEGG pathways and Gene Ontologies (Gene Ontology Consortium, 2015; Kanehisa & Goto, 2000), facilitating the analysis of complex biological processes. Functions within the application integrate data manipulation and web scraping to extract information from the Kyoto Encyclopedia of Genes and Genomes (KEGG) and QuickGo databases. Parallel processing enhances the efficiency of database queries, enabling rapid results from large datasets.

A key feature is the ability to obtain ancestral information for KEGG pathways and gene ontologies, which simplifies the understanding of their hierarchy and the classification of samples within a dataset. Users can study datasets at different levels of taxonomy directly from raw data. The application also generates interactive networks to visualize relationships between experimental groups and ontologies, preserving classification information. These networks are crucial for understanding the relationships within the displayed system.

These features make the software a valuable tool for analysts studying biological pathways, providing an intuitive interface with advanced data processing techniques. It allows researchers to elucidate the complexity of biological functions and gain insights into gene and molecular component relationships.

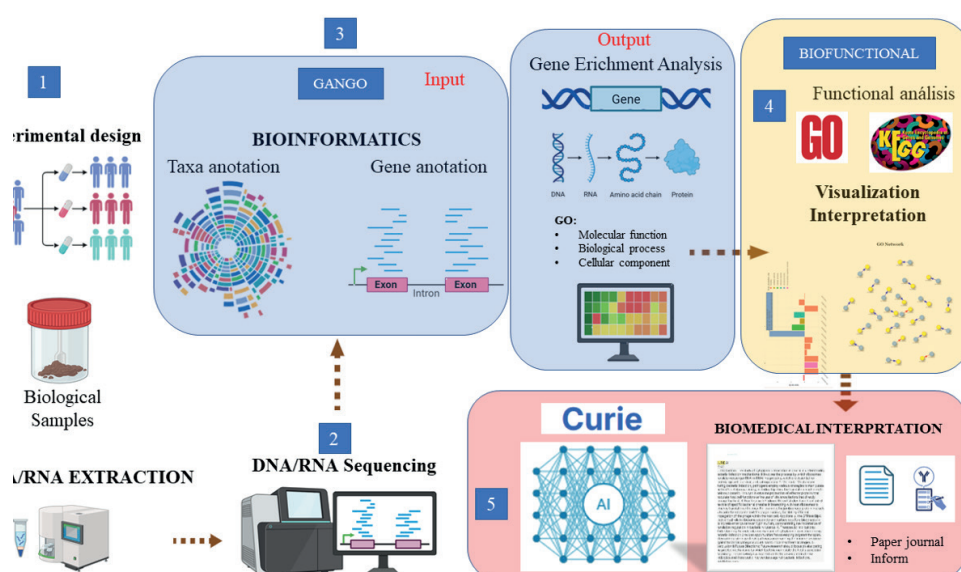


Figure 1. GANGO + BioFuncional Workflow. This diagram illustrates the complete process from biological sample collection to the functional interpretation of genetic results obtained using the GANGO+ BioFuncional ap-

plication. The workflow comprises the following key stages: 1) Experimental design and biological sample collection, followed by DNA/RNA extraction. 2) DNA/RNA sequencing. 3) GANGO: Bioinformatics procedures, outputting gene enrichment analysis. 4) BioFunctional: Visualization and quantification of the functional analysis (Gene Ontologies and KEGG). 5) Biomedical interpretation: Facilitating biomedical interpretation of the functional analysis through Artificial Intelligence. (Biomedical icons in this diagram were extracted using <https://www.biorender.com/>).

What is GANGO?

GANGO is an algorithm (Figure 1,3) that performs enrichment analysis to map genes, taxa, and groups to ontologies. It processes data from text files and generates an information-rich file for the BioFunctional algorithm. This algorithm represents KEGG pathways and ontologies, facilitating functional analysis and interpretation.

What are ontologies?

In bioinformatics, ontologies are structured vocabularies that standardize the description and classification of biological entities (e.g., genes) and their relationships. They aid in organizing and interpreting complex biological data (Gene Ontology Consortium, 2015).

What is KEGG?

KEGG (Kyoto Encyclopedia of Genes and Genomes) is a database of biological pathways, which are a series of molecular actions within a cell that lead to a specific product or change (Kanehisa & Goto, 2000).

What is enrichment analysis?

Enrichment analysis is a statistical method used to determine if a set of genes is over-represented in a particular category (e.g., a biological pathway or gene ontology term) compared to what would be expected by chance (Subramanian et al., 2005)

What is gene functional analysis?

Gene functional analysis is the process of determining the biological roles of genes, including the study of gene expression, protein interactions, and the effects of gene mutations (Reinitz & Hammer, 2004).

What is BioFunctional?

BioFunctional (Figure 1,4) is a software that extends Gene Ontology (GO) and KEGG pathway (metabolism) enrichment analysis. It generates network and bar plot visualizations and enhances previous gene ontology analysis by incorporating hierarchical information. This enables users to filter relevant GO ontologies or KEGG pathways through statistical analysis and facilitates functional interpretation using curated literature or the Biost3 research group's artificial intelligence tool, CURIE. CURIE¹ is currently under development by our research group and is pending publication (Figure 1,

1 CURIE is not directly integrated with GANGO + BioFunctional. Instead, it is an independent computational application currently undergoing testing on the research group's computational server. While GANGO + BioFunctional results are formatted to be readily interpretable by AI tools like CURIE, CURIE itself is presently only available within the University of Barcelona's facilities.

5). The appendix describes its functionality.

For a detailed understanding of BioFuncional, please refer to “BioFuncional: A Comprehensive App for Interpreting and Visualizing Functional Analysis of KEGG Pathways and Gene Ontologies” (Rodriguez & Monleon-Getino, 2024).

Description of the BioFuncional + GANGO application

The BioFuncional + GANGO application provides a workflow for functional analysis, specifically for elucidating Gene Ontology (GO) terms and KEGG pathway enrichment. This methodology allows researchers to derive biological meaning from gene lists or taxonomic classifications from experiments like transcriptomics or metagenomics. The application comprises two primary modules: GANGO and BioFuncional.

GANGO: Gene ontology and KEGG assignment

The GANGO module processes input data. It accepts a list of genes or taxa, is organized into user-defined groups, and performs the following operations:

- Data Input: Accepts a list of genes by taxa and their grouping.
- Functional Annotation: Maps input identifiers to Gene Ontology (GO) terms and KEGG pathways, associating each gene by taxon with its known biological functions, molecular activities, and involvement in specific biological pathways.
- Output Generation: Produces a dataset linking genes/taxa to GO terms and KEGG pathways, serving as input for subsequent analysis.

BioFuncional: Functional analysis and interpretation

The BioFuncional module processes the output from GANGO to interpret functional enrichment. It performs the following steps:

- Data Preprocessing:
- Column Selection: Pre-selects essential data columns. Users can also designate additional columns for filtering in later steps.
- File Export: Allows users to download preprocessed data files.
- Hierarchical Analysis:
- GO Hierarchy Integration: Incorporates GO hierarchical structure, retrieving ancestral relationships between GO terms to provide a framework for understanding the specificity and relationships among enriched functions.
- Hierarchical Data Augmentation: Integrates hierarchical information into the dataset, enabling analysis of functional enrichment at different levels of biological specificity.
- Network Analysis:
- Interactive Network Generation: Constructs interactive networks representing relationships between experimental groups and enriched GO terms.
- Customization: Allows users to customize network visualization by selecting GO categories and applying filters based on GO term hierarchy.

- Bar Plot Visualization (See Figure 2):
- Ontology Ranking: Generates bar plots that rank GO terms based on their enrichment within specified experimental groups.
- Significance Determination: Bar plots help identify pertinent GO terms for further investigation using a Z-score transformation, allowing users to visually assess the significance of functional enrichment.
- The bar plot then visualizes these Z-scores, making it easy to identify the most over-represented (or under-represented) GO terms in the comparison between the healthy and bacterial infection groups.
- Interpretation Guidance:
- Selection of Relevant Terms: Bar plots facilitate the selection of relevant GO terms for further interpretation, potentially involving tools or literature review.
- Emphasis on Group-Specific Terms: The application emphasizes focusing on GO terms most pertinent to the experimental groups of interest (e.g., treatment groups).

Results and discussion

In Appendix 1 of the article's supplementary materials, a detailed, step-by-step graphical tutorial of the GANGO + BioFunctional application's workflow can be found. This tutorial presents a real-world case study to demonstrate the tool's comprehensive functionality, specifically focusing on the functional analysis between a group of healthy individuals and a group with bacterial infection. RNA-Seq data from the study "Dysregulated transcriptional responses to SARS-CoV-2 in the periphery" (McClain et al., 2021) were utilized for this purpose, encompassing samples from subjects affected by bacterial infection versus healthy controls.

The overall workflow detailed in Appendix 1 for the GANGO + BioFunctional + CURIE application involves several key stages: it begins with experimental design and biological sample collection, followed by DNA/RNA extraction and subsequent sequencing. Next, the GANGO module performs bioinformatics procedures to output gene enrichment analysis. This is followed by the BioFunctional module, which handles the visualization and quantification of functional analysis (Gene Ontologies (GO)). Finally, the workflow culminates in biomedical interpretation, which is facilitated through Artificial Intelligence, such as the CURIE.

Implications and novelties

GANGO + BioFuncional offers several key advantages:

- **Streamlined Workflow:** It integrates GANGO and BioFuncional into a single application, simplifying the functional gene analysis process.
- **User-Friendly Interface:** The Shiny-based R application provides an intuitive interface, reducing the need for programming expertise.
- **Multi-Group Analysis:** The tool is designed to handle complex datasets with multiple experimental groups.

- **Comprehensive Analysis:** It combines enrichment analysis, hierarchical analysis, network visualization, and bar plot visualization.
- **Enhanced Interpretation:** It facilitates the selection of relevant GO terms and emphasizes group-specific results.
- **AI Integration:** Results are formatted to be readily interpretable by Artificial Intelligence tools like CURIE, developed by the Biost3 research group.

Specifically, to highlight the most relevant GO terms, the Enrichment Analysis (EA) values for each GO term are used. These EA values are then transformed into Z-scores.

Z-score transformation

Essentially, BioFuncional's bar plots (Figure 2) concisely represent the most relevant GO terms, categorized by GO type. Specifically, the Enrichment Analysis (EA) values for each GO term are transformed into Z-scores to highlight significance. This standardization allows for easy comparison of the relative importance of different GO terms.

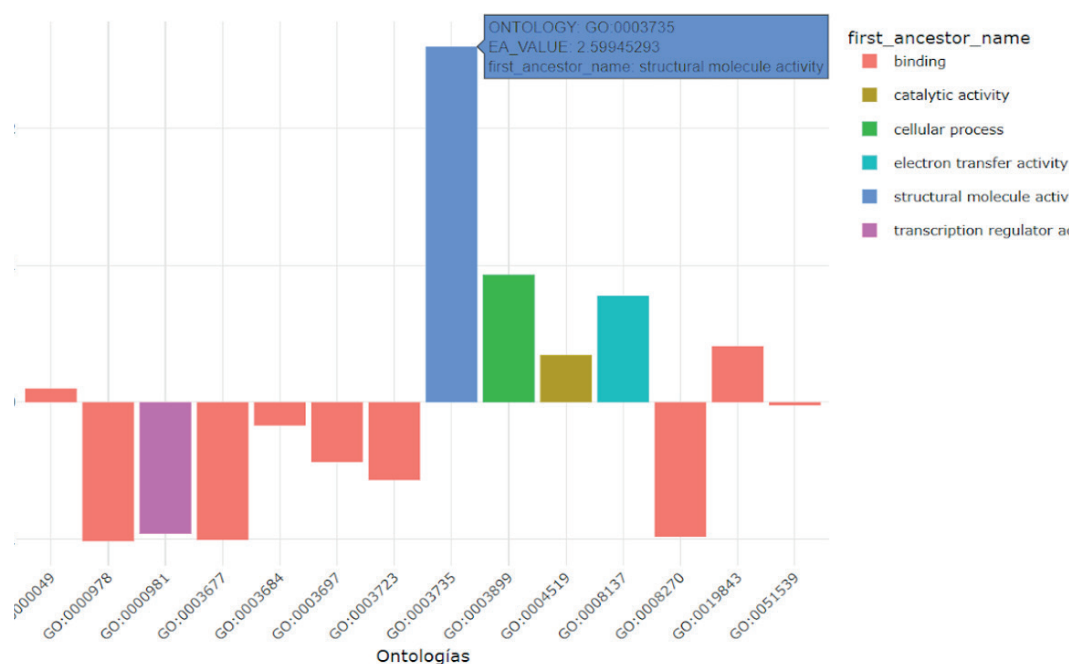


Figure 2. Bar Plot of Enriched Gene Ontologies from BioFuncional Analysis. This bar plot visualizes the Gene Ontology (GO) terms, ranked based on their enrichment within specified experimental groups, as determined by the BioFuncional application. The X-axis displays the enriched Gene Ontologies, representing specific biological functions or processes. The Y-axis represents the Z-score transformation, which allows users to visually assess the significance of functional enrichment. Z-scores make it easy to identify the most over-represented (positive Z-scores) or under-represented (negative Z-scores) GO terms in the comparison, specifically between the healthy and bacterial infection groups in this example.

A Z-score measures how far a data point is from the mean (average) of the dataset. It's calculated in units of standard deviations.

- A Z-score of 0 means the data point is exactly at the mean.
- A positive Z-score means the data point is above the mean.
- A negative Z-score means the data point is below the mean.

In this context, transforming the EA values to Z-scores allows us to:

- **Standardize:** Put all the EA values on a common scale, making it easier to compare the relative importance of different GO terms, even if their original EA values had very different ranges.
- **Highlight Significance:** GO terms with higher absolute Z-scores (farther from zero) are considered significantly more enriched. A large positive Z-score indicates a GO term is more enriched than average, while a large negative Z-score indicates it is less enriched.

These features make GANGO + BioFuncional a valuable tool for researchers in biology, genetics, and related fields.

Beyond transcriptomics: Expanding applicability to other omics data

GANGO + BioFuncional has been developed with a primary focus on functional gene analysis, particularly for data derived from transcriptomics. While GANGO is not directly designed to process raw data from other omics types such as proteomics or metabolomics, its modular architecture allows for broader applicability.

Users working with proteomics or metabolomics data would first need to translate their findings into relevant Gene Ontologies (GO) or KEGG pathways and then use BioFuncional to present ontologies, conveniently select them, and interpret them using CURIE. This can be achieved through established bioinformatics workflows in R, for instance, by using database searches (e.g., with Bioconductor packages like org.Hs.eg.db for gene IDs or clusterProfiler for enrichment analysis) to map protein identifiers or metabolites to their corresponding genes, and then performing enrichment analysis to obtain GO terms or KEGG pathways. Subsequently, these pre-processed GO or KEGG terms, when formatted appropriately, can be seamlessly integrated into BioFuncional for advanced visualization, hierarchical analysis, and AI-driven interpretation, thereby leveraging the full capabilities of our tool for a wider range of biological insights.

Accuracy and reliability

The accuracy and reliability of GANGO + BioFuncional's results are ensured through several key design principles and integrated features, including its robust statistical foundation (with Z-score transformation), its ability to integrate complex hierarchical and multi-group data, and a user-friendly design that minimizes errors and facilitates comprehensive data visualization and expert validation:

- **Statistical Foundation:** The tool's core relies on statistical enrichment analysis, a method used to identify biological functions or pathways that are significantly over-represented in a given gene list compared to what would be expected by chance. This statistical rigor forms the basis of the reliability of the identified enrichments.
- **Z-score Transformation for Significance:** To enhance the assessment of significance and enable robust comparisons, GANGO + BioFuncional transforms Enrichment Analysis (EA) values into

Z-scores. This standardization places all values on a common scale, making it easier to compare the relative importance of different Gene Ontology (GO) terms and highlight those that are most significantly enriched (further from zero).

- **Hierarchical Information Integration:** The tool incorporates the hierarchical structure of GO terms and KEGG pathways, providing a framework to understand the specificity and relationships among enriched functions. This integration of hierarchical data allows for analysis at different levels of biological specificity, contributing to more precise and reliable interpretations.
- **Robust Multi-Group Analytical Capabilities:** GANGO + BioFuncional is specifically designed to handle complex datasets involving multiple experimental groups. This capability ensures that the tool can robustly process and analyze diverse and complex biological scenarios, which is crucial for the reliability of comparative studies.
- **Comprehensive Visualization Tools:** The application provides comprehensive visualization tools, including interactive networks and significance-driven bar plots. These visualizations aid in the interpretation of key biological themes, making complex data more digestible and allowing users to visually assess the significance of functional enrichment, thereby increasing confidence in the results.
- **User-Friendly and Streamlined Workflow:** By integrating various analysis steps into a single, intuitive R-based Shiny application, GANGO + BioFuncional reduces the need for programming expertise and streamlines the analysis process. A simplified workflow can minimize user errors, indirectly contributing to the reliability of the outputs. The explicit goal of the tool's development was to "improve result accuracy and reliability".
- **Facilitating Cross-Referencing and Validation:** While the tool provides robust analytical outputs, the manuscript also emphasizes the importance of manual interpretation by experts. It suggests cross-referencing GO analysis results with other relevant data (e.g., other enrichment analyses, gene expression data, protein-protein interaction networks, phenotype data) to validate findings and look for consistency and convergence of evidence from multiple sources. This highlights that the tool provides the necessary data for users to perform their own validation steps.
- **AI Integration (with transparency):** GANGO + BioFuncional is compatible with AI-driven interpretation tools like CURIE. While CURIE is noted to be in an experimental phase and potentially subject to inconsistencies, this integration points towards future enhancements in interpretation and the potential for increased reliability as the AI technology matures.

Conclusions

In summary, GANGO + BioFuncional provides a significant advancement in functional analysis for high-throughput biological data. By integrating efficient data processing with robust analytical and visualization capabilities, this application empowers researchers to streamline complex analyses, enhance the interpretability of their findings, and ultimately derive more meaningful biological insights. Its user-friendly design, capacity to handle multi-group studies, and compatibility with AI-driven interpretation tools make it a valuable asset for a wide range of biological research, facilitating a deeper understanding of gene function and its implications.

Appendix A. Supplementary material

Supplementary material associated with this article can be found on <https://doi.org/10.62063/ecb-63>. To access the supplementary material, please visit the article landing page.

Funding

There is no funding to declare.

Conflict of interest

The authors declare no conflict of interest.

Data availability statement

All necessary files for the analysis are provided in the correct format and can be download in <https://github.com/amonleong/Biofunctional>

Ethics committee approval

Ethics committee approval is not required for this study.

Authors' contribution statement

The authors acknowledge their contributions to this paper as follows: **Study conception and design:** AR, TM; **Data collection:** AR, XT; **Analysis and interpretation of results:** XT, GC, JM; **Manuscript draft preparation:** TM, AR, GC. All authors reviewed the results and approved the final version of the manuscript.

Use of Artificial Intelligence: No artificial intelligence-based tools or applications were used in the preparation of this study. The entire content of the study was produced by the author(s) in accordance with scientific research methods and academic ethical principles.

ORCIDs and emails of the authors

Alejandro Rodriguez-Mena | ORCID 0009-0008-5839-0511 | alejandrorodriguez@ub.edu

Xavier Tarragó-Claramunt | ORCID 0009-0007-8364-3632 | xavitarragoc@gmail.com

Giulia Castellani | ORCID 0009-0005-5022-6918 | giuli.castellani@studenti.unicam.it

Javier Méndez-Viera | ORCID 0000-0003-3723-8787 | jmendez@ub.edu

Antonio Monleón-Getino | ORCID 0000-0001-8214-3205 | amonleong@ub.edu

References

- Alterovitz, G., Xiang, M., Mohan, M., & Ramoni, M. F. (2007). GO PaD: the Gene Ontology Partition Database. *Nucleic acids research*, 35(Database issue), D322–D327. <https://doi.org/10.1093/nar/gkl799>
- Ashburner, M., Ball, C. A., Blake, J. A., Botstein, D., Butler, H., Cherry, J. M., Davis, A. P., Dolinski, K., Dwight, S. S., Eppig, J. T., Harris, M. A., Hill, D. P., Issel-Tarver, L., Kasarskis, A., Lewis, S., Matese, J. C., Richardson, J. E., Ringwald, M., Rubin, G. M., & Sherlock, G. (2000). Gene ontology: Tool for the unification of biology. *Nature Genetics*, 25(1), 25–29. <https://doi.org/10.1038/75556>
- Chang, W., Cheng, J., Allaire, J., Sievert, C., Schloerke, B., Xie, Y., Allen, J., McPherson, J., Dipert, A., & Borges, B. (2025). *shiny: Web Application Framework for R* (R package version 1.10.0.9001). <https://github.com/rstudio/shiny>

- Chen, E. Y., Tan, C. M., Kou, Y., Duan, Q., Wang, Z., & Ma'ayan, A. (2013). Enrichr: Interactive and collaborative HTML5 gene list enrichment analysis tool. *BMC Bioinformatics*, 14(1), 128. <https://doi.org/10.1186/1471-2105-14-128>
- Gene Ontology Consortium (2015). Gene Ontology Consortium: going forward. *Nucleic acids research*, 43(Database issue), D1049–D1056. <https://doi.org/10.1093/nar/gku1179>
- Huang, D. W., Sherman, B. T., & Lempicki, R. A. (2009). Systematic and integrative analysis of large gene lists using DAVID bioinformatics resources. *Nature Protocols*, 4(1), 44–57. <https://doi.org/10.1038/nprot.2008.211>
- Kanehisa, M., & Goto, S. (2000). KEGG: Kyoto Encyclopedia of Genes and Genomes. *Nucleic Acids Research*, 28(1), 27–30. <https://doi.org/10.1093/nar/28.1.27>
- McClain, M. T., Constantine, F. J., Henao, R., Liu, Y., Tsalik, E. L., Burke, T. W., Steinbrink, J. M., Petzold, E., Nicholson, B. P., Rolfe, R., Kraft, B. D., Kelly, M. S., Saban, D. R., Yu, C., Shen, X., Ko, E. M., Sempowski, G. D., Denny, T. N., Ginsburg, G. S., & Woods, C. W. (2021). Dysregulated transcriptional responses to SARS-CoV-2 in the periphery. *Nat Commun* 12, 1079. <https://doi.org/10.1038/s41467-021-21289-y>
- Monleon-Getino, A., Paytuví-Gallart, A., Sanseverino, W., & Méndez, J. A. (2020). A new bioinformatic tool to interpret metagenomics/metatranscriptomics results based on the geometry of the clustering network and its differentially gene ontologies (GANGO) [Preprint]. *bioRxiv*. <https://doi.org/10.1101/2020.06.10.140103>
- Reinitz, J., & Hammer, M. (2004). A computational approach to gene functional analysis: Gene ontology, sequence motifs, and expression data. *Methods in Cell Biology*, 77, 1–23.
- Rodriguez, A., & Monleon-Getino, A. (2024). BioFunctional: A comprehensive app for interpreting and visualizing functional analysis of KEGG pathways and gene ontologies [Preprint]. *bioRxiv*. <https://doi.org/10.1101/2024.10.08.616405>
- Subramanian, A., Tamayo, P., Mootha, V. K., Mukherjee, S., Ebert, M. A., Gillette, M. A., Paulovich, A., Pomeroy, S. L., Golub, T. R., Lander, E. S., & Mesirov, J. P. (2005). Gene set enrichment analysis: A knowledge-based approach for interpreting genome-wide expression profiles. *Proceedings of the National Academy of Sciences*, 102(43), 15545–15550. <https://doi.org/10.1073/pnas.0506580102>
- Thomas, D. A. (2000). Functional genomics: A user's guide to the Rosetta Stone of gene function. *Genome Biology*, 1(3), reviews1003.1–reviews1003.7. <https://doi.org/10.1186/gb-2000-1-3-reviews1003>